



Universiteit Gent
Faculteit Wetenschappen
Vakgroep Fysica en Sterrenkunde

² No title yet

³ No sub-title neither, obviously...

⁴ Alexis Fagot

5



Thesis to obtain the degree of
Doctor of Philosophy in Physics
Academic years 2012-2017





Universiteit Gent
Faculteit Wetenschappen
Vakgroep Fysica en Sterrenkunde

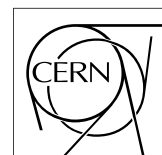
Promotoren: Dr. Michael Tytgat
Prof. Dr. Dirk Ryckbosch

Universiteit Gent
Faculteit Wetenschappen
Vakgroep Fysica en Sterrenkunde
Proeftuinstraat 86, B-9000 Gent, België
Tel.: +32 9 264.65.28
Fax.: +32 9 264.66.97

17



Thesis to obtain the degree of
Doctor of Philosophy in Physics
Academic years 2012-2017



Acknowledgements

¹⁹ Ici on remerciera tous les gens que j'ai pu croiser durant cette aventure et qui m'ont permis de passer
²⁰ un bon moment

²¹ *Gent, ici la super date de la mort qui tue de la fin d'écriture*
²² *Alexis Fagot*

Table of Contents

23

24	Acknowledgements	i
25	Nederlandse samenvatting	vii
26	English summary	ix
27	1 Introduction	1-1
28	1.1 A story of High Energy Physics	1-1
29	1.2 Organisation of this study	1-1
30	2 Investigating the TeV scale	2-1
31	2.1 The Standard Model of Particle Physics	2-2
32	2.1.1 A history of particle physics	2-2
33	2.1.2 Construction and test of the model	2-11
34	2.1.3 Investigating the TeV scale	2-12
35	2.2 The Large Hadron Collider & the Compact Muon Solenoid	2-14
36	2.2.1 LHC, the most powerful particle accelerator	2-14
37	2.2.1.1 Particle acceleration	2-15
38	2.2.1.2 High Luminosity LHC	2-18
39	2.2.2 CMS, a multipurpose experiment	2-20
40	2.3 Muon Phase-II Upgrade	2-20
41	3 Physics of Resistive plate chambers	3-1
42	3.1 Principle	3-1
43	3.1.1 Electron drift velocity	3-4
44	3.2 Rate capability and time resolution of Resistive Plate Chambers	3-4
45	3.2.1 Operation modes	3-4
46	3.2.2 Detector designs and performance	3-6
47	3.2.2.1 Double-gap RPC	3-7
48	3.2.2.2 Multigap RPC (MRPC)	3-8
49	3.2.2.3 Charge distribution and performance limitations	3-9
50	3.3 Signal formation	3-12
51	3.4 Gas transport parameters	3-12
52	4 Longevity studies and Consolidation of the present CMS RPC subsystem	4-1
53	4.1 Resistive Plate Chambers at CMS	4-1
54	4.1.1 Overview	4-1
55	4.1.2 The present RPC system	4-2
56	4.1.3 Pulse processing of CMS RPCs	4-3
57	4.2 Testing detectors under extreme conditions	4-4
58	4.2.1 The Gamma Irradiation Facilities	4-7

59	4.2.1.1	GIF	4-7
60	4.2.1.2	GIF++	4-9
61	4.3	Preliminary tests at GIF	4-11
62	4.3.1	Resistive Plate Chamber test setup	4-11
63	4.3.2	Data Acquisition	4-13
64	4.3.3	Geometrical acceptance of the setup layout to cosmic muons	4-13
65	4.3.3.1	Description of the simulation layout	4-14
66	4.3.3.2	Simulation procedure	4-16
67	4.3.3.3	Results	4-17
68	4.3.4	Photon flux at GIF	4-17
69	4.3.4.1	Expectations from simulations	4-17
70	4.3.4.2	Dose measurements	4-22
71	4.3.5	Results and discussions	4-23
72	4.4	Longevity tests at GIF++	4-24
73	4.4.1	Description of the Data Acquisition	4-27
74	4.4.2	RPC current, environmental and operation parameter monitoring	4-28
75	4.4.3	Measurement procedure	4-29
76	4.4.4	Longevity studies results	4-29
77	5	Investigation on high rate RPCs	5-1
78	5.1	Rate limitations and ageing of RPCs	5-1
79	5.1.1	Low resistivity electrodes	5-1
80	5.1.2	Low noise front-end electronics	5-1
81	5.2	Construction of prototypes	5-1
82	5.3	Results and discussions	5-1
83	6	Conclusions and outlooks	6-1
84	6.1	Conclusions	6-1
85	6.2	Outlooks	6-1
86	A	A data acquisition software for CAEN VME TDCs	A-1
87	A.1	GIF++ DAQ file tree	A-1
88	A.2	Usage of the DAQ	A-2
89	A.3	Description of the readout setup	A-3
90	A.4	Data read-out	A-3
91	A.4.1	V1190A TDCs	A-4
92	A.4.2	DataReader	A-6
93	A.4.3	Data quality flag	A-10
94	A.5	Communications	A-12
95	A.5.1	V1718 USB Bridge	A-13
96	A.5.2	Configuration file	A-13
97	A.5.3	WebDCS/DAQ intercommunication	A-17
98	A.5.4	Example of inter-process communication cycle	A-18
99	A.6	Software export	A-18
100	B	Details on the offline analysis package	B-1
101	B.1	GIF++ Offline Analysis file tree	B-1
102	B.2	Usage of the Offline Analysis	B-2
103	B.2.1	Output of the offline tool	B-3
104	B.2.1.1	ROOT file	B-3

105	B.2.1.2	CSV files	B-5
106	B.3	Analysis inputs and information handling	B-6
107	B.3.1	Dimensions file and IniFile parser	B-6
108	B.3.2	TDC to RPC link file and Mapping	B-7
109	B.4	Description of GIFT++ setup within the Offline Analysis tool	B-9
110	B.4.1	RPC objects	B-9
111	B.4.2	Trolley objects	B-10
112	B.4.3	Infrastructure object	B-11
113	B.5	Handling of data	B-12
114	B.5.1	RPC hits	B-13
115	B.5.2	Clusters of hits	B-14
116	B.6	DAQ data Analysis	B-15
117	B.6.1	Determination of the run type	B-16
118	B.6.2	Beam time window calculation for efficiency runs	B-17
119	B.6.3	Data loop and histogram filling	B-18
120	B.6.4	Results calculation	B-19
121	B.6.4.1	Rate normalisation	B-19
122	B.6.4.2	Rate and activity	B-21
123	B.6.4.3	Strip masking tool	B-23
124	B.6.4.4	Output CSV files filling	B-25
125	B.7	Current data Analysis	B-29

¹²⁶

Nederlandse samenvatting –Summary in Dutch–

¹²⁸ Le resume en Neerlandais (j'aurais peut-être pu apprendre la langue juste pour ça...).

¹²⁷

English summary

¹³⁰ Le meme résume mais en Anglais (on commencera par la hein!).

List of Figures

131

132 2.1	Through the gold foil experiment Rutherford could show that most of the mass of atoms was contained in a positively charged nucleus and could then propose a more accurate atomic model than that of Thomson.	2-3
133		
134		
135 2.2	Figure 2.2a: Meson octet. Figure 2.2b: Baryon octet. Figure 2.2c: Baryon decuplet. .	2-8
136		
137		
138 2.3	The elementary particles of the Standard Model are showed along with their names and properties. Their interactions with the strong, weak and electromagnetic forces have been explicated using color squares. In the left column, the scalar higgs boson is depicted, while the central is focused on the matter particles, the fermions, and the right on the force carriers, the gauge bosons. The role of the Higgs boson in electroweak symmetry breaking is highlighted, and the corresponding way properties of the various particles differ in the (high-energy) symmetric phase (top) and the (low-energy) broken-symmetry phase (bottom) are showed.	2-11
139		
140		
141		
142		
143		
144 2.4	CERN accelerator complex.	2-15
145		
146 2.5	Pictures of the different accelerators. From top to bottom: first the LINAC 2 and the <i>Pb</i> source of LINAC 3. Then the Booster and the LEIR. Finally, the PS, the SPS and the LHC.	2-16
147		
148 2.6	Figure 2.6a: schematics of the LHC cryodipoles. 1: Superconducting Coils, 2: Beam pipe, 3: Heat exchanger Pipe, 4: Helium-II Vessel, 5: Superconducting Bus-bar, 6: Iron Yoke, 7: Non-Magnetic Collars, 8: Vacuum Vessel, 9: Radiation Screen, 10: Thermal Shield, 11: Auxiliary Bus-bar Tube, 12: Instrumentation Feed Throughs, 13: Protection Diode, 14: Quadrupole Bus-bars, 15: Spool Piece Bus-bars. Figure 2.6b: magnetic field and resulting motion force applied on the beam particles. .	2-17
149		
150		
151		
152		
153		
154 2.7	Figure 2.7a: picture of the LHC quadrupoles. Figure 2.7b: magnetic fields and resulting focussing force applied on the beam by 2 consecutive quadrupoles.	2-18
155		
156 2.8	Detailed timeline of for LHC and HL-LHC operation until 2028 and operation projection until 2038. This timeline only describes the operation plans after LS1.	2-20
157		
158 2.9	Absorbed dose in the CMS cavern after an integrated luminosity of 3000 fb. R is the transverse distance from the beamline and Z is the distance along the beamline from the Interaction Point at Z=0.	2-21
159		
160		
161 2.10	A quadrant of the muon system, showing DTs (yellow), RPCs (light blue), and CSCs (green). The locations of new forward muon detectors for Phase-II are contained within the dashed box and indicated in red for GEM stations (ME0, GE1/1, and GE2/1) and dark blue for improved RPC (iRPC) stations (RE3/1 and RE4/1).	2-21
162		
163		
164		
165 2.11	RMS of the multiple scattering displacement as a function of muon p_T for the proposed forward muon stations. All of the electromagnetic processes such as bremsstrahlung and magnetic field effect are included in the simulation.	2-22
166		
167		

168	3.1	Different phases of the avalanche development in the RPC gas volume subjected to a constant electric field E_0 . a) An avalanche is initiated by the primary ionisation caused by the passage of a charged particle through the gas volume. b) Due to its growing size, the avalanche starts to locally influence the electric field. c) The electrons, lighter than the cations reach the anode first. d) The ions reach the cathode. While the charges have not recombined, the electric field in the small region around the avalanche stays affected and locally blind the detector.	3-2
175	3.2	Effeciency (circles and stars with 30 mV and 100 mV thresholds respectively) and streamer probability (opened circles) as function of the operating voltatge of a 2 mm single gap HPL RPC flushed with a gas mixture containing (a) 5%, (b) 2%, (c) 1% and (d) no SF_6 [33].	3-3
179	3.3	Movement of the charge carriers in an RPC. Figure 3.3a: Voltage across an RPC whose electrode have a relative permittivity of 5 at the moment the tension s applied. Figure 3.3b: After the charge carriers moved, the electrodes are charged and there is no voltage drop over the electrodes anymore. The full potential is applied on the gas gap only. Figure 3.3c: The streamer discharge initiated by a charged particle transports electrons and cations towards the anode and cathode respectively.	3-5
185	3.4	Typical oscilloscope pulses in streamer mode (Figure 3.4a) and avalanche mode(Figure 3.4b). In the case of streamer mode, the very small avalanche signal is visible.	3-5
187	3.5	Rate capability comparison for the streamer and avalanche mode of operation. An order of magnitude in rate capability for a maximal efficiency drop of 10% is gained by using the avalanche mode over the streamer mode.	3-6
190	3.6	Possible double-gap RPC layouts: a) "standard" 1D double-gap RPC, as used in CMS experiment, where the anodes are facing each other and a 1D read-out plane is sandwiched in between them, b) double read-out double-gap RPC as used in AT-LAS experiment, where the cathodes are facing each other and 2 read-out planes are used on the outer surfaces. This last layout can offer the possibility to use a 2D reconstruction by using orthogonal read-out planes.	3-7
196	3.7	Comparison of performance of CMS double and single gap RPCs using cosmic muons [44]. Figure 3.7a: Comparison of efficiency sigmoids. Figure 3.7b: Voltage distribution at 95% of maximum efficiency. Figure 3.7c: $\Delta_{10\%}^{90\%}$ distribution.	3-7
199	3.8	Presentation of ALICE MRPC using 250 μm gas gaps, 620 μm outer glass electrodes and 550 μm inner floating electrodes. More details on the labels are given in [45].	3-8
201	3.9	Particle identification applied to electrons in the STAR experiment. The identifica- tion is performed combining ToF and dE/dx measurements [50].	3-9
203	3.10	Comparison of the detector performance of ALICE ToF MRPC [51] at fixed applied voltage (in blue) and at fixed effective voltage (in red). The effective voltage is kept fixed by increasing the applied voltage accordingly to the current drawn by the detector.	3-9
206	3.11	Ratio between total induced and drifting charge have been simulated for single gap, double-gap and multigap layouts [52]. The total induced charge for a double-gap RPC is a factor 2 higher than for a multigap.	3-10
209	3.12	Charge spectra have been simulated for single gap, double-gap and multigap lay- outs [52]. It appears that when single gap shows a decreasing spectrum, double and multigap layouts exhibit a spectrum whose peak is detached from the origin. The detachment gets stronger as the number of gaps increases.	3-11
213	3.13	The maximal theoretical efficiency is simulated for single gap, double-gap and multi- gap layouts [52] at a constant gap thickness of 2 mm and using an effective Townsend coefficient of 9 mm^{-1}	3-11

216	4.1	Signals from the RPC strips are shaped by the FEE described on Figure 4.1a. Out- put LVDS signals are then read-out by a TDC module connected to a computer or converted into NIM and sent to scalers. Figure 4.1b describes how these converted signals are put in coincidence with the trigger.	4-3
220	4.2	Description of the principle of a CFD. A comparison of threshold triggering (left) and constant fraction triggering (right) is shown in Figure 4.2a. Constant fraction triggering is obtained thanks to zero-crossing technique as explained in Figure 4.2b. The signal arriving at the input of the CFD is split into three components. A first one is delayed and connected to the inverting input of a first comparator. A sec- ond component is connected to the noninverting input of this first comparator. A third component is connected to the noninverting input of another comparator along with a threshold value connected to the inverting input. Finally, the output of both comparators is fed through an AND gate.	4-4
229	4.3	(4.3a) Extrapolation from 2016 data of single hit rate per unit area in the barrel region. (4.3b) Extrapolation from 2016 data of single hit rate per unit area in the endcap region.	4-6
232	4.4	Background Fluka simulation compared to 2016 Data at $L = 10^{34} \text{ cm}^{-2} \cdot \text{s}^{-1}$ in the fourth endcap disk region. A mismatch in between simulation and data can be observed. [To be understood.]	4-7
235	4.5	Layout of the test beam zone called X5c GIF at CERN. Photons from the radioactive source produce a sustained high rate of random hits over the whole area. The zone is surrounded by 8 m high and 80 cm thick concrete walls. Access is possible through three entry points. Two access doors for personnel and one large gate for material. A crane allows installation of heavy equipment in the area.	4-8
240	4.6	^{137}Cs decays by β^- emission to the ground state of ^{137}Ba (BR = 5.64%) and via the 662 keV isomeric level of ^{137}Ba (BR = 94.36%) whose half-life is 2.55 min.	4-9
242	4.7	Floor plan of the GIF++ facility. When the facility downstream of the GIF++ takes electron beam, a beam pipe is installed along the beam line (z-axis). The irradiator can be displaced laterally (its center moves from $x = 0.65$ m to 2.15 m), to increase the distance to the beam pipe.	4-9
246	4.8	Simulated unattenuated current of photons in the xz plane (Figure 4.8a) and yz plane (Figure 4.8b) through the source at $x = 0.65$ m and $y = 0$ m. With angular correction filters, the current of 662 keV photons is made uniform in xy planes.	4-10
249	4.9	Description of the RPC setup. Dimensions are given in mm. A tent containing RPCs is placed at 1720 mm from the source container. The source is situated in the center of the container. RE-4-2-BARC-161 chamber is 160 mm inside the tent. This way, the distance between the source and the chambers plan is 2060 mm. Figure 4.9a provides a side view of the setup in the xz plane while Figure 4.9b shows a top view in the yz plane.	4-11
255	4.10	RE-4-2-BARC-161 chamber is inside the tent as described in Figure 4.9. In the top right, the two scintillators used as trigger can be seen. This trigger system has an inclination of 10° relative to horizontal and is placed above half-partition B2 of the RPCs. PMT electronics are shielded thanks to lead blocks placed in order to protect them without stopping photons from going through the scintillators and the chamber. 4-12	4-12

260	4.11 Hit distributions over all 3 partitions of RE-4-2-BARC-161 chamber is showed on 261 these plots. Top, middle and bottom figures respectively correspond to partitions A, 262 B, and C. These plots show that some events still occur in other half-partitions than 263 B2, which corresponds to strips 49 to 64, in front of which the trigger is placed, con- 264 tributing to the inefficiency of detection of cosmic muons. In the case of partitions 265 A and C, the very low amount of data can be interpreted as noise. On the other hand, 266 it is clear that a little portion of muons reach the half-partition B1, corresponding to 267 strips 33 to 48.	4-13
268	4.12 Results are derived from data taken on half-partition B2 only. On the 18 th of June 269 2014, data has been taken on chamber RE-2-BARC-161 at building 904 (Prevessin 270 Site) with cosmic muons providing us a reference efficiency plateau of $(97.54 \pm$ 271 $0.15)\%$ represented by a black curve. A similar measurement has been done at GIF 272 on the 21 st of July with the same chamber giving a plateau of $(78.52 \pm 0.94)\%$ 273 represented by a red curve.	4-14
274	4.13 Representation of the layout used for the simulations of the test setup. The RPC is 275 represented as a yellow trapezoid while the two scintillators as blue cuboids looking 276 at the sky. A green plane corresponds to the muon generation plane within the sim- 277 ulation. Figure 4.9a shows a global view of the simulated setup. Figure 4.9b shows 278 a zommed view that allows to see the 2 scintillators as well as the full RPC plane.	4-15
279	4.14 γ flux $F(D)$ is plot using values from table 4.1. As expected, the plot shows similar 280 attenuation behaviours with increasing distance for each absorption factors.	4-18
281	4.15 Figure 4.15a shows the linear approximation fit done via formulae 4.7 on data from 282 table 4.2. Figure 4.15b shows a comparison of this model with the simulated flux 283 using a and b given in figure 4.15a in formulae 4.4 and the reference value $D_0 =$ 284 50cm and the associated flux for each absorption factor F_0^{ABS} from table 4.1	4-20
285	4.16 Dose measurements has been done in a plane corresponding to the tents front side. 286 This plan is 1900 mm away from the source. As explained in the first chapter, a 287 lens-shaped lead filter provides a uniform photon flux in the vertical plan orthogonal 288 to the beam direction. If the second line of measured fluxes is not taken into account 289 because of lower values due to experimental equipments in the way between the 290 source and the tent, the uniformity of the flux is well showed by the results.	4-22
291	4.17	4-23
292	4.18 Evolution of the maximum efficiency for RE2 (4.18a) and RE4 (4.18b) chambers 293 with increasing extrapolated γ rate per unit area at working point. Both irradiated 294 (blue) and non irradiated (red) chambers are shown.	4-25
295	4.19 Evolution of the working point for RE2 (4.19a) and RE4 (4.19b) with increasing 296 extrapolated γ rate per unit area at working point. Both irradiated (blue) and non 297 irradiated (red) chambers are shown.	4-25
298	4.20 Evolution of the maximum efficiency at HL-LHC conditions, i.e. a background hit 299 rate per unit area of 300Hz/cm^2 , with increasing integrated charge for RE2 (4.20a) 300 and RE4 (4.20b) detectors. Both irradiated (blue) and non irradiated (red) chambers 301 are shown. The integrated charge for non irradiated detectors is recorded during test 302 beam periods and stays small with respect to the charge accumulated in irradiated 303 chambers.	4-26
304	4.21 Comparison of the efficiency sigmoid before (triangles) and after (circles) irradiation 305 for RE2 (4.21a) and RE4 (4.21b) detectors. Both irradiated (blue) and non irradiated 306 (red) chambers are shown.	4-26
307	4.22 Evolution of the Bakelite resistivity for RE2 (4.22a) and RE4 (4.22b) detectors. Both 308 irradiated (blue) and non irradiated (red) chambers are shown.	4-27

309	4.23 Evolution of the noise rate per unit area for the irradiated chamber RE2-2-BARC-9 only.	4-27
310		
311	A.1 (A.1a) View of the front panel of a V1190A TDC module [58]. (A.1b) View of the front panel of a V1718 Bridge module [59]. (A.1c) View of the front panel of a 6U 6021 VME crate [60].	A-3
312		
313		
314	A.2 Module V1190A <i>Trigger Matching Mode</i> timing diagram [58].	A-4
315		
316	A.3 Structure of the ROOT output file generated by the DAQ. The 5 branches (<code>EventNumber</code> , <code>number_of_hits</code> , <code>Quality_flag</code> , <code>TDC_channel</code> and <code>TDC_TimeStamp</code>) are visible on the left panel of the ROOT browser. On the right panel is visible the histogram cor- responding to the variable <code>nHits</code> . In this specific example, there were approximately 50k events recorded to measure the gamma irradiation rate on the detectors. Each event is stored as a single entry in the <code>TTree</code>	A-10
317		
318		
319		
320		
321	A.4 The effect of the quality flag is explained by presenting the content of <code>TBranch</code> <code>number_of_hits</code> of a data file without <code>Quality_flag</code> in Figure A.4a and the con- tent of the same <code>TBranch</code> for data corresponding to a <code>Quality_flag</code> where all TDCs were labelled as <code>GOOD</code> in Figure A.4b taken with similar conditions. It can be noted that the number of entries in Figure A.4b is slightly lower then in Figure A.4a due to the excluded events.	A-12
322		
323		
324		
325		
326		
327	A.5 Using the same data as previously showed in Figure A.4, the effect of the quality flag is explained by presenting the reconstructed hit multiplicity of a data file with- out <code>Quality_flag</code> in Figure A.5a and the reconstructed content of the same RPC partition for data corresponding to a <code>Quality_flag</code> where all TDCs were labelled as <code>GOOD</code> in Figure A.5b taken with similar conditions. The artificial high content of bin 0 is completely suppressed.	A-12
328		
329		
330		
331		
332		
333	A.6 WebDCS DAQ scan page. On this page, shifters need to choose the type of scan (Rate, Efficiency or Noise Reference scan), the gamma source configuration at the moment of data taking, the beam configuration, and the trigger mode. These in- formation will be stored in the DAQ ROOT output. Are also given the minimal measurement time and waiting time after ramping up of the detectors is over before starting the data acquisition. Then, the list of HV points to scan and the number of triggers for each run of the scan are given in the table underneath.	A-14
334		
335		
336		
337		
338		
339		
340	B.1 Example of expected hit time distributions in the cases of efficiency (Figure B.1a) and noise/gamma rate per unit area (Figure B.1b) measurements as extracted from the raw ROOT files. The unit along the x-axis corresponds to ns. The fact that "the" muon peak is not well defined in Figure B.1a is due to the contribution of all the RPCs being tested at the same time that don't necessarily have the same signal arrival time. Each individual peak can have an offset with the ones of other detectors. The inconsistancy in the first 100 ns of both time distributions is an artefact of the TDCs and are systematically rejected during the analysis.	B-16
341		
342		
343		
344		
345		
346		
347		
348	B.2 The effect of the quality flag is explained by presenting the reconstructed hit multi- plicity of a data file without <code>Quality_flag</code> . The artificial high content of bin 0 is the effect of corrupted data.	B-19
349		
350		

- 351 B.3 Display of the masking tool page on the webDCS. The window on the left allows the
352 shifter to edit `ChannelsMapping.csv`. To mask a channel, it only is needed to set the
353 3rd field corresponding to the strip to mask to 0. It is not necessary for older mapping
354 file formats to add a 1 for each strip that is not masked as the code is versatile and
355 the default behaviour is to consider missing mask fields as active strips. The effect
356 of the mask is directly visible for noisy channels as the corresponding bin turns red.
357 The global effect of masking strips will be an update of the rate value showed on the
358 histogram that will take into consideration the rejected channels. B-24

List of Tables

359

360	3.1 Properties of the most used electrode materials for RPCs.	3-4
361	4.1 Total photon flux ($E\gamma \leq 662$ keV) with statistical error predicted considering a	
362	^{137}Cs activity of 740 GBq at different values of the distance D to the source along	
363	the x-axis of irradiation field [55].	4-17
364	4.2 Correction factor c is computed thanks to formulae 4.5 taking as reference $D_0 =$	
365	50 cm and the associated flux F_0^{ABS} for each absorption factor available in table 4.1. .	4-19
366	4.3 The data at D_0 in 1997 is taken from [55]. In a second step, using Equations 4.8	
367	and 4.9, the flux at D can be estimated in 1997. Then, taking into account the	
368	attenuation of the source activity, the flux at D can be estimated at the time of the	
369	tests in GIF in 2014. Finally, assuming a sensitivity of the RPC to γ $s = 2 \cdot 10^{-3}$,	
370	an estimation of the hit rate per unit area is obtained.	4-21
371	A.1 Inter-process communication cycles in between the webDCS and the DAQ through	
372	file string signals.	A-19

373

List of Acronyms

374

List of Acronyms

375

376

A

377

378

379

AFL

Almost Full Level

380

381

B

382

383

384

BARC

Bhabha Atomic Research Centre

385

BLT

Block Transfer

386

BNL

Brookhaven National Laboratory

387

BR

Branching Ratio

388

389

C

390

391

392

CAEN

Costruzioni Apparecchiature Elettroniche Nucleari S.p.A.

393

CERN

European Organization for Nuclear Research

394

CFD

Constant Fraction Discriminator

395

CMB

Cosmic Microwave Background

396

CMS

Compact Muon Solenoid

397

CSC

Cathode Strip Chamber

398

399

D

400

401

402

DAQ

Data Acquisition

403

DCS

Detector Control Software

404

DQM

Data Quality Monitoring

405

DT

Drift Tube

406

407

F

408

409

410	FCC	Future Circular Collider
411	FEE	Front-End Electronics
412	FEB	Front-End Board
413		
414		
415	G	
416		
417	GE-/-	Find a good description
418	GE1/1	Find a good description
419	GE2/1	Find a good description
420	GEANT	GEometry ANd Tracking - a series of software toolkit platforms developed by CERN
421		
422	GEM	Gas Electron Multiplier
423	GIF	Gamma Irradiation Facility
424	GIF++	new Gamma Irradiation Facility
425		
426		
427	H	
428		
429	HL-LHC	High Luminosity LHC
430	HPL	High-pressure laminate
431	HV	High Voltage
432		
433		
434	I	
435		
436	iRPC	improved RPC
437	IRQ	Interrupt Request
438	ISR	Intersecting Storage Rings
439		
440		
441	L	
442		
443	LEIR	Low Energy Ion Ring
444	LEP	Large Electron-Positron
445	LHC	Large Hadron Collider
446	LS1	First Long Shutdown
447	LS2	Second Long Shutdown
448	LS3	Third Long Shutdown
449	LV	Low Voltage
450	LVDS	Low-Voltage Differential Signaling
451		
452		
453	M	
454		

455	MC	Monte Carlo
456	MCNP	Monte Carlo N-Particle
457	ME/-	Find good description
458	ME0	Find good description
459	MRPC	Multigap RPC
460		
461	N	
462		
463		
464	NIM	Nuclear Instrumentation Module logic signals
465		
466	P	
467		
468		
469	PMT	PhotoMultiplier Tube
470	PS	Proton Synchrotron
471	PU	pile-up
472		
473	Q	
474		
475		
476	QCD	Quantum Chromodynamics
477	QED	Quantum Electrodynamics
478		
479	R	
480		
481		
482	RE/-	Find a good description
483	RE2/2	Find a good description
484	RE3/1	Find a good description
485	RE3/2	Find a good description
486	RE4/1	Find a good description
487	RE4/2	Find a good description
488	RE4/3	Find a good description
489	RMS	Root Mean Square
490	ROOT	a framework for data processing born at CERN
491	RPC	Resistive Plate Chamber
492		
493	S	
494		
495		
496	SC	Synchrocyclotron
497	SLAC	Stanford Linear Accelerator Center

498	SM	Standard Model
499	SPS	Super Proton Synchrotron
500	SUSY	supersymmetry
501		
502	T	
503		
504		
505	TDC	Time-to-Digital Converter
506	ToF	Time-of-flight
507		
508		
509	W	
510		
511	webDCS	Web Detector Control System

1

Introduction

512

513

⁵¹⁴ **1.1 A story of High Energy Physics**

⁵¹⁵ **1.2 Organisation of this study**

2

516

517

Investigating the TeV scale

518 „We may regard the present state of the universe as the effect of the
519 past and the cause of the future. An intellect which at any given mo-
520 ment knew all of the forces that animate nature and the mutual posi-
521 tions of the beings that compose it, if this intellect were vast enough
522 to submit the data to analysis, could condense into a single formula
523 the movement of the greatest bodies of the universe and that of the
524 lightest atom; for such an intellect nothing could be uncertain and
525 the future just like the past would be present before its eyes.”

526

527 - Pierre Simon de Laplace, *A Philosophical Essay on Probabilities*, 1814

528 Throughout history, physics experiment became more and more powerful in order to investigate
529 finer details of nature and helped understanding the elementary blocks of matter and the fundamental
530 interactions that bond them in the microscopic world. Nowadays, the Standard Model (SM) of
531 particle physics is the most accurate theory designed to explain the behaviour of particles and was
532 able to make very precise predictions that are constantly verified, although some hints of new physics
533 are visible as bricks are still missing to have a global comprehension of the Universe.

534 To highlight the limits of the SM and test the different alternative theories, ever more powerful
535 machines are needed. This is in this context that the Large Hadron Collider (LHC) has been thought
536 and built to accelerate and collide particles at energies exceeding anything that had been done be-
537 fore. Higher collision energies and high pile-up imply the use of enormous detectors to measure the
538 properties of the interaction products. The Compact Muon Solenoid (CMS) is a multipurpose ex-
539 periment that have been designed to study the proton-proton collisions of the LHC and give answers
540 on various high energy physics scenari. Nevertheless, the luminosity delivered by the collider will
541 in the future be increased to levels beyond the original plans to improve its discovery potential giv-
542 ing no choice to experiments such as CMS to upgrade their technologies to cope with the increased
543 radiation levels and detection rates.

544 **2.1 The Standard Model of Particle Physics**

545 In this early 21st century it is now widely accepted that matter is made of elementary blocks referred
546 to as *elementary particles*. The physics theory that classifies and describes the best the behaviour
547 and interaction of such elementary particles is the so called Standard Model that formalizes 3 of
548 the 4 fundamental interactions (electromagnetic, weak and strong interactions). It's development
549 took place during the 20th century thanks to a strong collaboration in between the theoretical and
550 experimental physicists.

551 **2.1.1 A history of particle physics**

552 The idea that nature is composed of elementary bricks, called *atomism*, is not contemporary as it
553 was already discussed by Indian or Greek philosophers during antiquity. In Greece, atomism has
554 been rejected by Aristotelianism as the existance of *atoms* would imply the existance of a void that
555 would violate the physical principles of Aristotle philosophy. Aristotelianism has been considered
556 as a reference in the european area until the 15th century and the italian *Rinascimento* where antic
557 text and history started to be more deeply studied. The re-discovery of Platon's philosophy would
558 allow to open the door to alternative theories and give a new approach to natural sciences where
559 experimentation would become central. A new era of knowledge was starting. By the begining of
560 the 17th century, atomism was re-discovered by philosophers and the very first attempt to estimate
561 an *atom* size would be provided by Magnetus in 1646. Although his *atoms* correspond to what would
562 nowadays be called *molecules*, Magnetus achieved feats by calculating that the number of molecules
563 in a grain of incense would be of the order of 10^{18} simply by considering the time necessary to smell
564 it everywhere in a large church after the stick was lit on. It is now known that this number only falls
565 short by 1 order of magnitude.

566 An alternative philosophy to atomism popularized by Descartes was corpuscularianism. Built on
567 ever divisible corpuscles, contrary to atoms, it's principles would be mainly used by alchemists like
568 Newton who would later develop a corpuscular theory of light. Boyle would combine together ideas
569 of both atomism or corpuscularianism leading to mechanical philosophy. The 18th century have

seen the development of engineering providing philosophical thought experiments with repeatable demonstration and a new point of view to explain the composition of matter and Lavoisier would greatly contribute to chemistry and atomism by publishing in 1789 a list of 33 chemical elements corresponding to what is now called *atoms*. In the early 19th century Dalton would summarize the knowledge on composition of matter and Fraunhofer would invent the spectrometer and discover the spectral lines. The rise of atomic physics, chemistry and mathematical formalism would unravel the different atomic elements and ultimately, the 20th century would see the very first sub-atomic particles.

Discovery of the inner structure of the atom

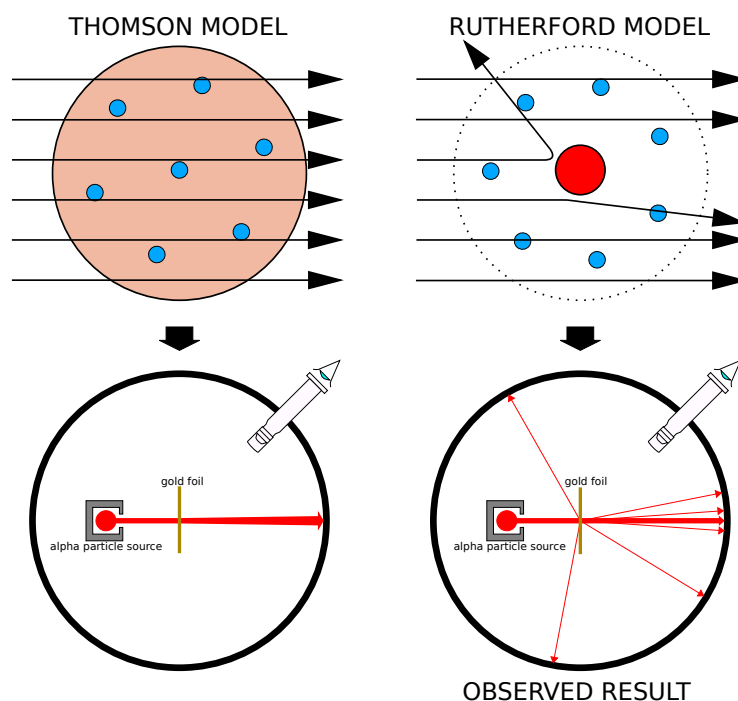


Figure 2.1: Through the gold foil experiment Rutherford could show that most of the mass of atoms was contained in a positively charged nucleus and could then propose a more accurate atomic model than that of Thomson.

The negative *electron* would be the first to be discovered in 1897 by Thomson after 3 decades of research on cathode rays by proving that the electrification observed in an electroscope, as reported by Perrin, was due to the rays themselves and that they had to be composed of electrically charged particles. In 1900, Becquerel would show the *beta rays* emitted by radium had the same charge over mass ratio than what measured by Thomson for cathode rays, pointing to electrons as a constituent of atoms. In 1907, Rutherford and Royds showed that *alpha* particles, once captured in a tube and subjected to an electric spark causing an electron avalanche, where helium ions as they could combine with 2 electrons to form a ${}^4\text{He}$. This discovery was directly followed by the constraint of the atom structure in 1909 through the gold foil experiment in which the deflection angle of alpha particles fired at a very thin gold foil was measured and highlighted atoms where mainly empty with

589 nearly all its mass contained into a tiny positively charged *nucleus*. With these two observations,
 590 he could formulate the Rutherford model of the atom in 1911, shown together with the Thomson
 591 plum pudding model in Figure 2.1. The link in between atomic number and number of positive and
 592 negative charges contained into the atoms would fast be understood and the different kind of element
 593 transmutation appeared to be purely nuclear processes making clear that the electromagnetic nature
 594 of chemical transformation could not possibly change nuclei. Thus a new branch in physics appeared
 595 to study nuclei exclusively: the nuclear physics.

596 Moreover, in 1913 quantum physics would be introduced into the atomic model by Bohr based
 597 on the assumptions of Plank to explain spectral lines, and other observed quantum effects. The same
 598 year, Moseley would confirm Bohr's model and Debye would extend it by introducing elliptical
 599 orbits.

600 By studying alpha emission and the product of their interaction with nitrogen gas, Rutherford
 601 reported in 1919 the very first nuclear reaction leading to the discovery that the hydrogen nucleus was
 602 composed of a single positively charged particle that was later baptised *proton*. This idea came from
 603 1815 Prout's hypothesis proposing that all atoms are composed of "*protyles*" (i.e. hydrogen atoms).
 604 By using scintillation detectors, Rutherford could highlight typical hydrogen nuclei signature and
 605 understand that the impact of alpha particles with nitrogen would knock out an hydrogen nucleus
 606 and produce an oxygen 17, as explicated in Formula 2.1 and would then postulate that protons are
 607 building bricks of all elements.



608 With this assumption and the discovery of isotopes together with Aston, elements with identical
 609 atomic number but different masses, Rutherford would propose that all elements' nuclei but hydrogen's are composed of both charged particles, protons, and of chargeless particles, which he called
 610 *neutrons*, and that these neutral particles would help maintaining nuclei as one, as charged protons
 611 were likely to electrostatically repulse each other, and introduced the idea of a new force, a *nuclear*
 612 force. Though the first idea concerning neutrons was a bond state of protons and electrons as it was
 613 known that the beta decay, emitting electrons, was taking place in the nucleus, it was then showed
 614 that such a model would hardly be possible due to Heisenberg's uncertainty principle and by the
 615 recently measured *spin* of both protons and electrons. The spin, discovered through the study of
 616 the emission spectrum of alkali metals, would be understood as a "two-valued quantum degree of
 617 freedom" and formalized by Pauli and extended by Dirac, to take the relativist case into account.
 618 Measured to be $\frac{1}{2}\hbar$ for both, it was impossible to arrange an odd number of half integer spins and
 619 obtain a global nucleus spin that would be integer. Finally, in 1932, following the discovery of a new
 620 neutral radiation, Chadwick could discover the neutron as an uncharged particle with a mass similar
 621 to that of the proton whose half integer spin would reveal to be the solution to explain the nuclear
 622 spin.

624 Development of the Quantum Electrodynamics

625 Historically, the development of the quantum theory revolved around the question of emission and
 626 absorption of discrete amount of energy through light. Einstein used the initial intuition of Plank
 627 about the black-body radiation to develop in 1905 a model to explain the photoelectric effect in
 628 which light was described by discrete quanta now called *photons*. For this model, Einstein introduced
 629 the concept of wave-particle duality as classical theory was not able to describe the phenomenon.
 630 With the new understanding of atoms and of their structure, classical theories also proved unable

631 to explain atoms stability. Indeed, using classical mechanics, electrons orbiting around a nucleus
 632 should radiate an energy proportional to their angular momentum and thus lose energy through
 633 time and the spectrum of energy emission should then be continuous, but it was known since the
 634 19th century and the discovery of spectral lines that the emission spectrum of material was discrete.

635 This was Bohr who first suggested that a quantum description of the atom was necessary in 1913.
 636 Using the correspondence principle stating that at large enough numbers the quantum calculations
 637 should give the same results than the classical theory, he proposed the very first quantum model
 638 of the hydrogen atom explaining the line spectrum by introducing the principal quantum number
 639 n describing the electron shell. This model would then be improved by Sommerfeld that would
 640 quantize the z-component of the angular momentum, leading to the second and third quantum
 641 numbers, or azimuthal and magnetic quantum number, l and m defining for the second the orbital
 642 angular momentum of the electrons on their shells and thus, the shape of the orbital, and for the third
 643 the available orbital on the subshell for each electron. Nevertheless, although the model was not only
 644 limited to spherical orbitals anymore, making the atom more realistic, the Zeeman effect couldn't be
 645 completely explained by just using n , l and m . A solution would be brought after the discovery of
 646 Pauli in 1924, as Uhlenbeck, Goudsmit, and Kramers proposed in 1925 the idea of intrinsic rotation
 647 of the electron, introducing a new angular momentum vector associated to the particle itself, and
 648 not to the orbital, and associated to a new quantic number s , the *spin* projection quantum number
 649 explaining the lift of degeneracy to an even number of energy levels.

650 The introduction of the *spin* happened 1 year after another attempt of improvement of the theory
 651 was made by De Broglie in his PhD thesis. The original formulation of the quantum theory only
 652 considered photons as energy quanta behaving as both waves and particles. De Broglie proposed
 653 that all matter are described by waves and that their momentum is proportional to the oscillation of
 654 quantized electromagnetic field oscillators. This interpretation was able to reproduce the previous
 655 version of the quantum energy levels by showing that the quantum condition involves an integer
 656 multiple of 2π , as shown by Formula 2.2.

$$p = \hbar k \Leftrightarrow \int pdx = \hbar \int kdx = 2\pi\hbar n \quad (2.2)$$

657 Although the intuition of De Broglie about the wave-particle duality of all matter, his interpretation
 658 was semiclassical and it's in 1926 that the first fully quantum mechanical wave-equation would
 659 be introduced by Schrödinger to describe electron-like particles, reproducing the previous semiclassical
 660 formulation without inconsistencies. This complexe equation describes the evolution of the
 661 wave function Ψ of the quantum system, defined by its position vector \mathbf{r} and time t as an energy
 662 conservation law, in which the hamiltonian of the system \hat{H} is explicit, by solving the Equation 2.3.

$$i\hbar \frac{\partial}{\partial t} |\Psi(\mathbf{r}, t)\rangle = \hat{H} |\Psi(\mathbf{r}, t)\rangle \quad (2.3)$$

663 In 1927, Dirac would go further in his paper about emission and absorption of radiation by
 664 proposing a second quantization not only of the physical process at play but also of the electromagnetic
 665 field, providing the ingredients to the first formulation of *Quantum Electrodynamics (QED)*
 666 and the description of photon emission by electrons dropping into a lower energy state in which the
 667 final number of particles is different than the initial one. To complete this model to the many-body
 668 wave functions of identical particles, Jordan included creation and annihilation operators for fields
 669 obeying Fermi-Dirac statistics leading to a model describing particles that would be referred to as
 670 *fermions*. Nevertheless, in order to properly treat electromagnetism, the incorporation of the relativ-

ity theory developed by Einstein. Including gravity into quantum physics still is a challenge nowadays, but in 1928 Pauli and Jordan would show that special relativity's coordinate transformations could be applied to quantum fields as the field commutators were Lorentz invariant. Finally derived the same year, the Dirac equation, shown as Equation 2.4, similarly to Schrödinger's equation, is a single-particle equation but it incorporates special relativity in addition to quantum mechanics rules. It features the 4×4 gamma matrices γ^μ built using 2×2 Pauli matrices and unitary matrix, the 4-gradient ∂_μ , the rest mass m of any half integer spin massive particle described by the wave function $\psi(x, t)$, also called a Dirac spinor, and the speed of light c . In addition to perfectly reproduce the results obtained with quantum mechanics so far, it also provided with *negative-energy solutions* that would later be interpreted as a new form of matter, *antimatter* and give a theoretical justification to the Pauli equation that was phenomenologically constructed to account for the spin as in the non-relativistic limit, the Dirac equation is similar.

$$i\hbar\gamma^\mu\partial_\mu\psi - mc\psi = 0 \quad (2.4)$$

The successes of the QED was soon followed with theoretical problems as computations of any physical process involving photons and charged particles were showed to be only reliable at the first order of perturbation theory. At higher order of the theory, divergent contributions were appearing giving nonsensical results. Only two effects were contributing to these infinities.

- The self-energy of the electron (or positron), the energy that the particle has due its own interaction with its environment.
- The vacuum polarization, virtual electron–positron pairs produced by a background electromagnetic field in the vacuum which is not an "empty" space. These virtual pairs affect the charge and current distributions generated by the original electromagnetic field.

Solving this apparent problem was done by carefully defining the concepts of each observables, for example mass or charge, as these quantities are understood within the context of a non-interacting field equation, and that from the experiment point of view, they are abstractions as what is measured are "renormalized observables" shifted from there "bare" value by the interaction taking place in the measuring process. The infinities needed to be connected to corrections of mass and charge as those are fixed to finite values by experiment. This was the intuition of Bethe in 1947 who successfully computed the effect of such *renormalization* in the non-relativist case. Fully covariant formulations of QED including renormalization was achieved by 1949 by Tomonaga, Schwinger, Feynman and Dyson and Feynman is now famous for his association of diagrams to the term of the scattering matrix, greatly simplifying the representation and computation of interactions as the diagrams directly corresponded the measurable physical processes and would then be used in every quantum field theories. With the resolution of infinities, QED had mostly reached its final form, being still today the most accurate physical theory and would serve as a model to build all other quantum field theories.

Development of the quark model and Quantum Chromodynamics

To explain the nuclear force that holds *nucleons* (protons and neutrons) together, Yukawa theoretically proposed in 1934 the existence of a force carrier called *meson* due to it's predicted mass in the range in between the electron and nucleon masses. Discovered in 1936 by Anderson and Neddermeyer, and confirmed using bubble chambers in 1937 by Street and Stevenson, a first meson

711 candidate was observed in the decay products of cosmic rays. Assuming it had the same electric
 712 charge than electrons and protons, this particle was observed to have a curvature due to magnetic
 713 field that was sharper than protons but smoother than electrons resulting in a mass in between that
 714 of electrons and protons. But its properties were not compatible with Yukawa's theory, which was
 715 emphasized by the discovery of a new candidate in 1947, again in cosmic ray products using photo-
 716 graphic emulsions.

717 This new candidate, although it had a similar mass than the already believed *meson*, would rather
 718 decay into it. For distinction, the first candidate would then be renamed "*mu meson*" when the second
 719 would be the "*pi meson*". The *mu meson* was behaving like a heavy electron and didn't participate
 720 in the strong interaction whereas the pion was believed to be the carrier of the nuclear interaction.
 721 This lead to classify the *mu* in a new category of particles called *leptons* together with the electron
 722 that shared similar properties and *the neutrino*, and be renamed *muon*. The *pi meson* was finally
 723 found to be a triplet of particles: a positively charged, a negatively charged, and a neutral particle.
 724 The neutral *pi meson* has been more difficult to identify as it wouldn't leave tracks on emulsions nor
 725 on bubble chambers and needed to be studied via it's decay products. It was ultimately identified in
 726 University of California's cyclotron in 1950 through the observation of its decay into 2 photons.

727 Also discovered in 1947 but in cloud chamber photographs, the *K meson* as also been an im-
 728 portant step towards the establishment of the Standard Model. A triplet of particle, 2 charged and a
 729 neutral, with a mass roughly half that of a proton, were reported. These particles were baptised *K*
 730 *meson* in contrast to the "light" *pi* and *mu* "L-mesons". The particularity of the *K* were there very
 731 slow decays with a typical lifetime of the order of 10^{-10} s much greater than the 10^{-23} s of *pi*-proton
 732 reactions. The concept of *strangeness*, a new quantum number was then introduced by Pais as an
 733 attempt to explain this phenomenon as *strange* particles appeared as a pair production of a strange
 734 and anti-strange particle.

735 With the development of synchrotrons, the particle *zoo* would grow to several dozens during the
 736 1950s as higher energies were reachable through acceleration. In 1961, a first classification system,
 737 called Eightfold Way, was proposed by Gell-Mann and finding its roots in the Gell-Mann–Nishijima
 738 formula, which relates the electric charge Q , the third component of the isospin I_3 , the *baryon*
 739 number B and the strangeness S , as explicitated in Formula 2.5. The isospin was a quantum number
 740 introduced in 1932 to explain symmetries of the newly discovered neutron using representation
 741 theory of SU(2). The baryon number, was introduced by Nishijima as a quantum number for baryons,
 742 i.e. particles of the same family as nucleons. The mesons were classified in an octet and baryons of
 743 spin $\pm \frac{1}{2}$ and $\pm \frac{3}{2}$ were respectively classified into an octet and a decuplet, as shown in Figure 2.2. To
 744 complete the baryon decuplet, Gell-Mann predicted the existance of baryon Ω^- which would later
 745 be discovered in 1964.

$$Q = I_3 + \frac{1}{2}(B + S) \quad (2.5)$$

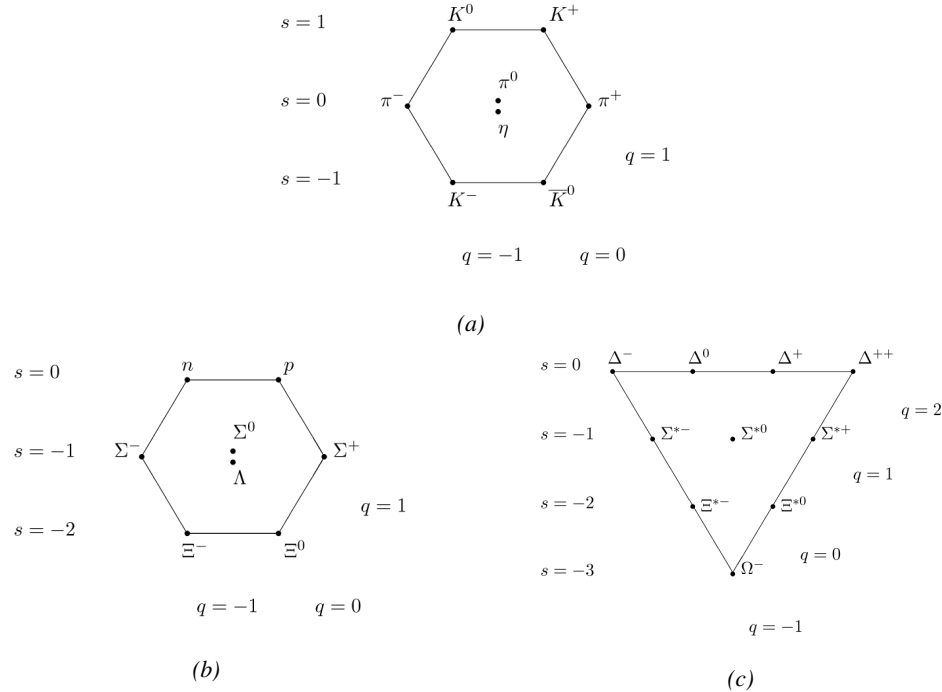


Figure 2.2: Figure 2.2a: Meson octet. Figure 2.2b: Baryon octet. Figure 2.2c: Baryon decuplet.

Strong of this classification using an SU(3) flavor symmetry, Gell-Mann, and independently Zweig, would propose a full theoretical model in which *hadrons* (strongly interacting particles, i.e. mesons and baryons) were not elementary particles anymore. They would rather be composed with 3 flavors of particles called *quarks* and there anti-particles. The 3 flavors were called *up*, *down* and *strange*. *Up* and *down* would be used to explain the nucleons and non-strange mesons, while *strange* would come into the composition of hadrons showing strangeness. *Up* and *down* flavors would be discovered in 1968 thanks to the deep inelastic scattering experiments conducted at the Stanford Linear Accelerator Center (SLAC), and *strange* could only be indirectly validated even though it provided a robust explanation to *kaon* (K) and *pion* (π). However, in the decade following the Gell-Mann-Zweig quark model proposition, several improvement to the model were brought, first by Glashow and Bjorken the same year that predicted the existence of a fourth quark flavor, the *charm*, that would equalize the then known number of quarks and leptons and finally in 1973 by Kobayashi and Maskawa that would increase the number of quarks to 6 to explain the experimental observation of CP violation. These two quarks would be referred to as *top* and *bottom* for the first time in 1975. It's only after these additions to the quark model that finally the *charm* would be discovered in 1974 at both SLAC and Brookhaven National Laboratory (BNL). A meson where the *charm* was bound with an *anti-charm*, called J/ψ , would help convince the physics community of the validity of the model. The *top* would be discovered soon after in 1977 in Fermilab and indicate the existence of the *bottom* that would resist to discovery until Fermilab's experiments CDF and D \emptyset in 1995 due to its very large mass and the energy needed to produce it.

As remarked by Struminsky, the original quark model proposal composed of 3 quarks should possess an additional quantum number due to mesons such as Ω^- or Δ^{++} . Indeed, these mesons are composed of 3 identical quarks, respectively 3 *strange* and *up* quark, with parallel spins, which

should be forbidden by the exclusion principle. Independentle, Greenberg and Han-Nambu proposed an additional SU(3) degree of freedom possessed by the quarks, that would later be refered to as *color charge gauge*, that could interact through *gluons*, the gauge boson octet corresponding to this degree of freedom. Nevertheless, as observing free quarks proved to be impossible, two visions of the quarks were argued mainly due to the failures to observe these particles free to prove their existence. On one side, Gell-Mann proposed to see quarks as mathematical construct instead of real particles, as they are always confined, implying that quantum field theory would not describe entirely the strong interaction. Opposed to this vision, Feynman on the contrary argued that quarks were real particles, that he would call *partons*, that should be described as all other particles by a distribution of position and momentum. The implications of quarks as point-like particles would be verified at SLAC and the concept of *color* would be added to the quark model in 1973 by Fritzsch and Leutwyler together with Gell-Mann to propose a description of the strong interaction through the theory of Quantum Chromodynamics (QCD). The discovery the same year of asymptotic freedom within the QCD by Groos, Politzer and Wilczek, allowed for very precise predictions thanks to the perturbation theory. Nowadays, the confinement of quarks is studied in experiments such as ALICE, through exploration of the quark-gluon plasma.

785 The Weak interaction, spontaneous symmetry breaking, the Higgs mechanism and the Elec- 786 troweak unification

The weak interaction is the process that causes radioactive decays. Thanks to the neutron discovery, Fermi could explain in 1934 the beta radiations through the beta decay process in which the neutron decays into a proton by emitting an electron. Though the missing energy observed during this process triggered a huge debate about the apparent non conservation of energy, momentum and spin of the process, Fermi, as Pauli before him, proposed that the missing energy was due to a neutral not yet discovered particle that would then be baptised *neutrino*. The impossibility to detect such a particle would leave some members of the scientific community sceptical, but hints of energy conservation and of the existence of the neutrino were provided by measuring the energy spectrum of electrons emitted through beta decay, as there was a strict limit on their energy. It's only 30 years later in 1953 that it would be discovered by the team of Cowan and Reines using the principle of inverse beta decay described through Formula 2.6. The experiment consisted in placing water tanks sandwiched in between liquid scintillators near a nuclear reactor with an estimated neutrino flux of $5 \times 10^{13} \text{ s}^{-1} \text{ cm}^{-2}$. However, in order to explain the absence of some reactions in the experiment of Cowan and Reines, and constraint the beta decay theory of Fermi and extend it to the case of the muon, Konopinski and Mahmoud proposed in 1953 that the muon decay would eject a particle similar to the neutrino and thus predicted the existence of a muon neutrino that would be different than the one involved in the beta decay, related to the electron. With this, the idea of lepton number would arise. The muon neutrino would successfully be detected in 1962 by Lederman, Schwartz and Steinberger.

$$\bar{\nu} + p \rightarrow n + e^+ \quad (2.6)$$

The theory could not be valid though as the probability of interaction, called cross-section, would have been increasing without bond with the square of the energy. Fermi assumed in a two vector current coupling but Lee and Yang noted that an axial current could appear and would violate parity. The experiment of Wu in 1956 would confirm the parity violation and Gamow and Teller would try to account for it by describing Fermi's interaction through allowed (parity-violating) and superallowed

811 (parity-conserving) decays. But the success of QED as a quantum field theory would spark the
812 development of such a theory to describe the weak interaction.

813 As previously discussed, the great success of QED was built on an underlying symmetry, inter-
814 preted as a gauge invariance so that the effect of the force is the same in all space-time coordinates,
815 and of the possibility to renormalize it in order to absorb the infinities. Independently in 1958,
816 Glashow, and Salam and Ward used 1957 Schwinger ideas about vector intermediary for the decay
817 processes, could find a way to unite both the electromagnetic and weak interaction into a gauge
818 theory involving 4 gauge bosons, 3 of which were massive and carried out the weak interaction and
819 a massless boson carrying the electromagnetic interaction. Among the 3 massive bosons, 2 were
820 charged and 1 was neutral, similarly to the previously theorized *pi meson* vector of the Yukawa
821 model and all have a mass much greater than nucleons and thus a very short life time implying a
822 finite very short range contrary to the contact interaction originally proposed by Fermi.

823 Breakthrough in other fields of physics contributed in giving theoretical support and interpreta-
824 tion to the unified electroweak theory. The stepping stone would be the use of spontaneous symmetry
825 breaking that was inspired to Nambu at the end of the 1950s following the development of the BCS
826 superconductivity mechanism in 1957. Cooper had shown that BCS pairs, pairs of electrons bound
827 together at low temperature, could have lower energy than the Fermi energy and where responsi-
828 ble for superconductivity. This lead to the discovery of Goldstone-Nambu bosons as a result of the
829 spontaneous breaking of the chiral symmetry in a theory describing nucleons and mesons devel-
830 opped by Nambu and Jona-Lasinio in 1961, and now understood as a low-energy approximation of
831 QCD. Similarly to mechanism of energy gap appearance in superconductivity, the nucleon mass
832 is suggested to the result of a self-energy of a fermion field and is studied through a four-fermion
833 interaction in which, as a consequence of the symmetry, bound states of nucleon-antinucleon pairs
834 appear and can be regarded as virtual pions. Though the symmetry is maintained in the equations,
835 the ground state is not preserved. Goldstone would later the same year show that the bound states
836 corresponds to spinless bosons with zero mass.

837 Although the model in itself didn't revolutionize particle physics, spontaneous symmetry break-
838 ing would be generalized to quantum field theories. As all fundamental interactions are described
839 using gauge theories based on underlying symmetries, processes such as the chiral symmetry break-
840 ing would be introduced soon after the publication of Nambu and Jona-Lasinio. In 1962, Anderson,
841 following an idea of Schwinger who suggested that zero-mass vector bosons were not necessarily
842 required to describe the conservation of baryons contrary to the bosons emerging from chiral sym-
843 metry breaking, discussed the implications of spontaneous symmetry breaking in particles physics.
844 A model was finally independently built in 1964 by Brout and Englert, Higgs, and Guralnik, Hagen,
845 and Kibble, who discovered that combining an additional field into a gauge theory in order to break
846 the symmetry, the resulting gauge bosons acquire a nonzero mass. Moreover, Higgs stated that this
847 implied the existence of at least one new massive, i.e. self-interacting, scalar boson, that are now
848 known as *Higgs bosons* corresponding to this additional field. The Higgs mechanism today specific-
849 ally refers to the process through which the gauge bosons of the weak interaction acquire mass. In
850 1968, Weinberg could point to the Higgs mechanism to integrate a Higgs field into a new version
851 of the electroweak theory in which the spontaneous symmetry breaking mechanism of the Higgs
852 field would explicitly explain the masses of the weak interaction gauge bosons and the zero-mass
853 of photons.

854 2.1.2 Construction and test of the model

855 The Standard Model of particle physics was built in the middle of the 1970s after the experimental
 856 confirmation of the existence of quarks. It is based on the assembly of the models previously introduced
 857 and describing the fundamental interactions, except for gravitation, and their gauge bosons
 858 as well as the way elementary "matter" particles interact with the fields associated with these force
 859 carriers. In this sense, the development of QED and the unification of the electroweak interaction,
 860 of the Yukawa interaction and of QCD, and of the Higgs mechanism made it possible to explain most
 861 of contemporary physics.

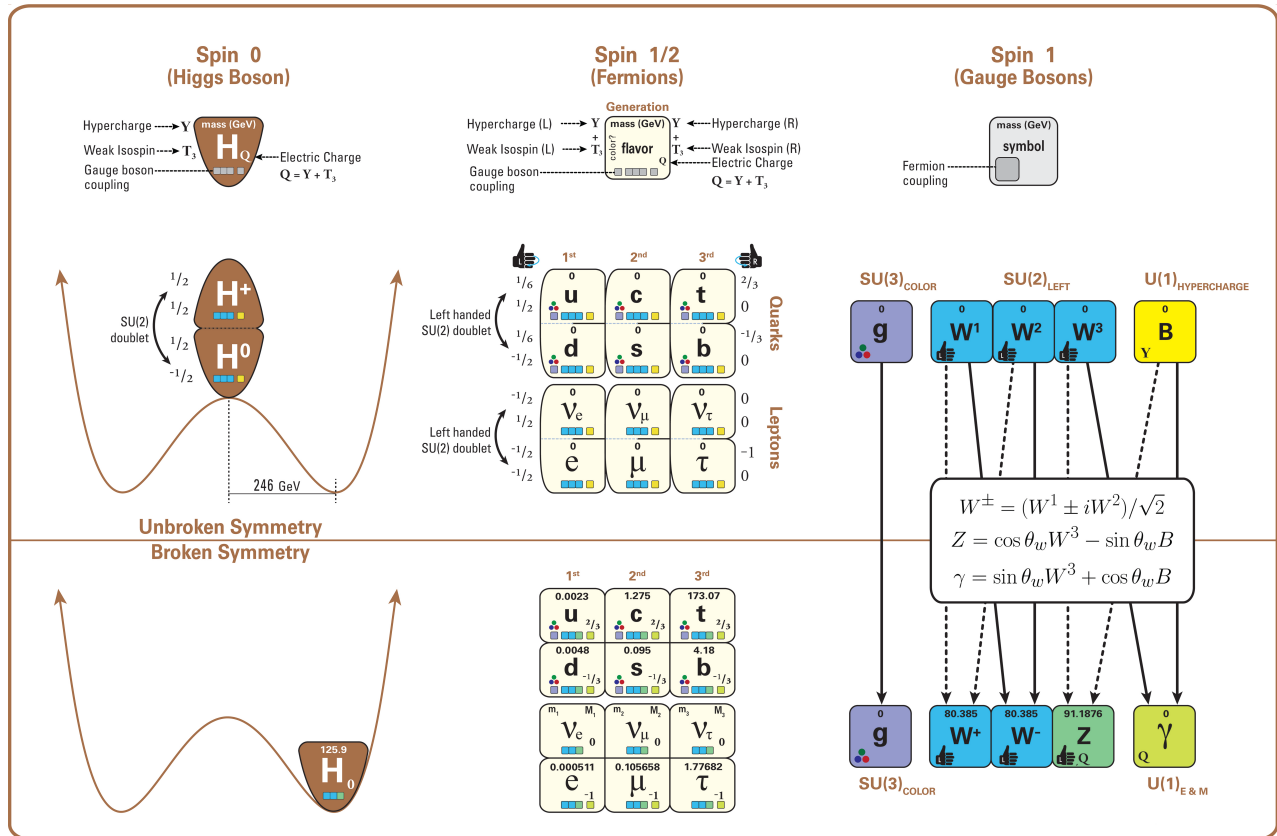


Figure 2.3: The elementary particles of the Standard Model are showed along with their names and properties. Their interactions with the strong, weak and electromagnetic forces have been explicited using color squares. In the left column, the scalar higgs boson is depicted, while the central is focused on the matter particles, the fermions, and the right on the force carriers, the gauge bosons. The role of the Higgs boson in electroweak symmetry breaking is highlighted, and the corresponding way properties of the various particles differ in the (high-energy) symmetric phase (top) and the (low-energy) broken-symmetry phase (bottom) are showed.

862 In the SM, "matter" particles, are described by 12 fermion fields of spin $\frac{1}{2}$ obeying the Fermi-
 863 Dirac statistics, i.e. subjected to the Pauli exclusion principle. To each fermion is associated its
 864 corresponding antiparticle. The fermions are classified according to the way they interact and, thus,
 865 according to the charges they carry. 6 of them are classified as quarks (u, d, c, s, t , and b) and
 866 are subjected to all interactions and the 6 others as leptons ($e^-, \mu^-, \tau^-, \nu_e, \nu_\mu$, and ν_τ). Leptons

867 are not subjected to the strong interaction and among them, the 3 neutrinos only interact weakly as
 868 they are neutral particles, which explains why they are so difficult to detect. The gauge boson fields
 869 are the gluons g for the strong interaction, the photon γ for the electromagnetic interaction and the
 870 weak bosons W^+ , W^- , and Z^0 for the weak interaction. Finally, the Higgs field H^0 is responsible,
 871 through the spontaneous symmetry breaking, of the mixing of the massless electroweak boson fields
 872 W_1 , W_2 , W_3 , and B leading to the observable states γ , W^+ , W^- , and Z^0 that can gain mass while
 873 interacting with the Higgs field. This picture of the SM is summarized through Figure 2.3 where the
 874 antifermions are not showed.

875 When the model was first finalized, the existence of the weak gauge bosons, of the charm, of the
 876 third quark generation composed of top and bottom quarks to explain the observed CP violation was
 877 not proven but the predictions were measured with good precision in the years following. First, the
 878 charm quark would be discovered in 1974, followed by the bottom quark in 1977. The weak bosons
 879 would be discovered during the next decade in 1983. The top quark would resist until 1995 due to
 880 its very large mass but would offer the last piece of the elementary QCD particles. The very last
 881 predicted elementary particle of the model that was not observed yet would prove to be very difficult
 882 to observe. the Higgs boson needed the start of the LHC to finally be observed in 2012. A few years
 883 more of tests were necessary to measure its properties to confirm the observation of a scalar boson
 884 compatible with the predicted Higgs boson H^0 . Even though only quark-antiquark (mesons) and 3
 885 quark states (baryons) were observed, exotic hadrons were not forbidden by QCD and no limit of
 886 quark is imposed by the theory. Moreover, gluons could form bond states by themselves and with
 887 quarks. These two types of states are called *glueballs* and *hybrid hadrons*. For decades, experi-
 888 ments have been conducted without confirmation of such possible states existing. Nevertheless, in
 889 2014, tetraquarks were observed by LHCb, one of LHC's main experiments, and in 2015, the same
 890 experiment reported the discovery of pentaquarks making the SM one of the best tested theories of
 891 physics.

892 2.1.3 Investigating the TeV scale

893 Even though the SM is a well tested theory, several hints of physics going beyond its scope have
 894 been observed. First of all, gravity is not explained through this model and huge difficulties are en-
 895 countered when trying to include gravitation. The strength of gravitational interaction is expected to
 896 be negligible at the scale of elementary particles, nevertheless, adding gravitation in the perspective
 897 of developing a "theory of everything" leads to divergent integrals that could not be fixed through
 898 renormalization.

899 Moreover, the SM considers neutrinos to be massless but it was shown in the late 1960s by the
 900 Homestake experiment that the flux of solar neutrinos (i.e. ν_e) measured didn't match the predicted
 901 values due to neutrino oscillations, confirmed in the early 2000s by the Sudbury Neutrino Obser-
 902 vatory. This oscillation implies that neutrinos that can be observed are a superposition of massive
 903 neutrino states. The research on neutrino oscillation is already quite advanced with experiments
 904 looking at atmospheric, reactor or beam neutrinos in order to determine the elements of the mixing
 905 matrix similar to the CKM matrix describing the mixing of quarks. Nevertheless, no answer to the
 906 origin of neutrino mass is provided.

907 Another intriguing fact is that the universe is dominated by matter. However, the SM predicted
 908 that matter and antimatter should have been created in equal amounts and no mechanism is able to
 909 explain this matter-antimatter asymmetry. Although this asymmetry is seen from the visible uni-
 910 verse, it may be possible that other unknown regions of the Universe are dominated by antimatter.

911 Another possibility to explain the apparent asymmetry would be the existence of a electric dipole
912 in any fundamental particle that would permit matter and antimatter particles to decay at different
913 rates.

914 The discrepancy of velocity dispersion of stars in galaxies with respect to the visible mass they
915 contain is known since the end of the 19th century where Kelvin proposed that this problem could
916 be solved if a "*great majority of [the stars] would be dark bodies*". Throughout the 20th century,
917 physicists like Kapteyn, Zwicky, showed the first hints of a "*dark matter*" by studying star veloc-
918 ities and galactic clusters, followed by robust measurements of galaxy rotation curves by Babcock
919 which suggested that the mass-to-luminosity ratio was different from what would be expected from
920 watching the visible light. Later in the 1970s, Rubin and Ford from direct light observations and
921 Rogstad and Shostak from radio measurements showed that the radial velocity of visible objects in
922 galaxies was increasing with increasing distance to the center of the galaxy. Finally observation of
923 lensing effect by galaxy clusters, temperature distribution of hot gas in galaxies and clusters, and
924 the anisotropies in the Cosmic Microwave Background (CMB) kept on pointing to a "*dark matter*".
925 From all the data accumulated, the visible matter would only account to no more than 5% of the total
926 content on the visible universe. Alternative theories have tried to investigate modified versions of
927 the General Relativity as this theory is only well tested at the scale of the solar system but is not suf-
928 ficiently tested on wider ranges or even theories in which gravitation is not a fundamental force but
929 rather an emergent one, but so far, such theories have difficulties to reproduce all the experimental
930 observations as easily as through dark matter.

931 A possible theory to offer dark matter candidates would be supersymmetry (SUSY) which pro-
932 poses a relationship in between bosons and fermions. In this model, each elementary particle,
933 through a spontaneous spacetime symmetry breaking mechanism would have a *super partner* from
934 the other family of particles. On top of providing heavy dark matter candidates, supersymmetry
935 could also help solving the *Hierarchy problem*, the very large scale difference in between the weak
936 interaction and gravity, although, as mentioned before, in the case gravity is found not to be a funda-
937 mental force, this problem would automatically fade.

938

939 All these different aspects of physics beyond the Standard Model of particle physics and the
940 Standard model itself can be tested through the use of very energetic and intense hadron and ion col-
941 liders. The LHC at CERN is a perfect tool to seek answers to these open questions except maybe for
942 the gravity as gravity is extremely weak at particles level. For example, one of LHCb experiment's
943 goal is to investigate CP-violation and thus baryonic asymmetry. In 2017, the collaboration has an-
944 nounced to have so far a 3.3σ statistical significance over a CP-violation through the study of the
945 decays of Λ_b^0 and $\overline{\Lambda}_b^0$ into a proton (or antiproton) and 3 pions. Many analysis teams are also working
946 hard on supersymmetry both in ATLAS and CMS collaborations, the two multipurpose experiments
947 of LHC, even though no evidence of a supersymmetrical theory was seen, the few hint having the
948 tendency to confirm the standard model. These experiments also have the possibility to investigate
949 ways to explain Majorana neutrino mass through Yukawa interactions of scalar particles.

950 The higher the center-of-mass energy, the smaller details the experiments will be able to see, the
951 heavier the potential particle creation barrier will be, the stronger the cross-section of certain rare
952 decay channels will be. All these advantages eventually lead to new discoveries and deeper under-
953 standing of the models describing our Universe. But the LHC only is a step forward to gather more
954 precise tests of the Standard Model and new knowledge about the physics beyond it. A successful
955 physics campaign will probably serve to justify the building of new accelerators with even greater
956 discovery potential like for example the Future Circular Collider (FCC) that would push even further

957 the study of the unanswered questions of contemporary physics.

958 2.2 The Large Hadron Collider & the Compact Muon Solenoid

959 Throughout its history, CERN has played a leading role in high energy particle physics. Large re-
 960 gional facilities such as CERN were thought after the second world war in an attempt to increase
 961 international scientific collaboration and allows scientists to share the forever increasing costs of
 962 experiment facilities required due to the need for increasing the energy in the center of mass to
 963 deeper probe matter. The construction of the first accelerators at the end of the 50s, the Synchro-
 964 cyclotron (SC) and the Proton Synchrotron (PS), was directly followed by the first observation of
 965 antinuclei in 1965 [1]. Strong from the experience of the Intersecting Storage Rings (ISR), the very
 966 first proton-proton collider that showed hints that protons are not elementary particles, the Super
 967 Proton Synchrotron (SPS) was built in the 70s to investigate the structure of protons, the preference
 968 for matter over antimatter, the state of matter in the early universe or exotic particles, and lead to
 969 the discovery in 1983 of the W and Z bosons [2–5]. These newly discovered particles and the elec-
 970 troweak interaction would then be studied in details by the Large Electron-Positron (LEP) collider
 971 that will help to prove in 1989 that there only are three generations of elementary particles [6]. The
 972 LEP would then be dismantled in 2000 to allow for the LHC to be constructed in the existing tunnel.

973 2.2.1 LHC, the most powerful particle accelerator

974 The LHC has always been considered as an option to the future of CERN. At the moment of the
 975 construction of the LEP beneath the border between France and Switzerland, the tunnel was built in
 976 order to accomodate what would be a Large Hadron Collider with a dipole field of 10 T and a beam
 977 energy in between 8 and 9 TeV [7] directly followed in 1985 with the creation of a 'Working Group
 978 on the Scientific and Technological Future of CERN' to investigate such a collider [8]. The decision
 979 was finally taken almost 10 years later, in 1994, to construct the LHC in the LEP tunnel [9] and the
 980 approval of the 4 main experiments that would take place at the 4 interaction points would come in
 981 1997 [10] and 1998 [11]:

- 982 • ALICE [12] has been designed in the purpose of studying quark-gluon plasma that is believed
 983 to have been a state of matter that existed in the very first moment of the universe.
- 984 • ATLAS [13] and CMS [14] are general purpose experiments that have been designed with
 985 the goal of continuing the exploration of the Standard Model and investigate new physics.
- 986 • LHCb [15] has been designed to investigate the preference of matter over antimatter in the
 987 universe through the CP violation.

988 These large scale experiments, as well as the full CERN accelerator complex, are displayed on
 989 Figure 2.4. The LHC is a 27 km long hadron collider and the most powerful accelerator used for
 990 particle physics since 2008 [16]. The LHC was originally designed to collide protons at a center-
 991 of-mass energy of 14 TeV and luminosity of $10^{34} \text{ cm}^{-2}\text{s}^{-1}$, as well as Pb ions at a center-of-mass
 992 energy of 2.8 TeV/A with a peak luminosity of $10^{27} \text{ cm}^{-2}\text{s}^{-1}$. Run 1 of LHC, when the center-of-
 993 mass energy only was half of the nominal LHC energy, was enough for both CMS and ATLAS to
 994 discover the Higgs boson [17] and for LHCb to discover pentaquarks [18] and confirm the existance
 995 of tetraquarks [19]. Nevertheless, after the Third Long Shutdown (LS3) (2024-2026), the accelerator

will be in the so called High Luminosity LHC (HL-LHC) configuration [20], increasing its instantaneous luminosity to $10^{35} \text{ cm}^{-2}\text{s}^{-1}$ for pp collisions and to $4.5 \times 10^{27} \text{ cm}^{-2}\text{s}^{-1}$, boosting the discovery potential of the LHC. The HL-LHC phase should last at least another 10 years depending on the breakthrough this machine would lead to. Already a new accelerating device, the FCC, as been proposed to prepare the future of high energy physics after the LHC.

CERN's Accelerator Complex

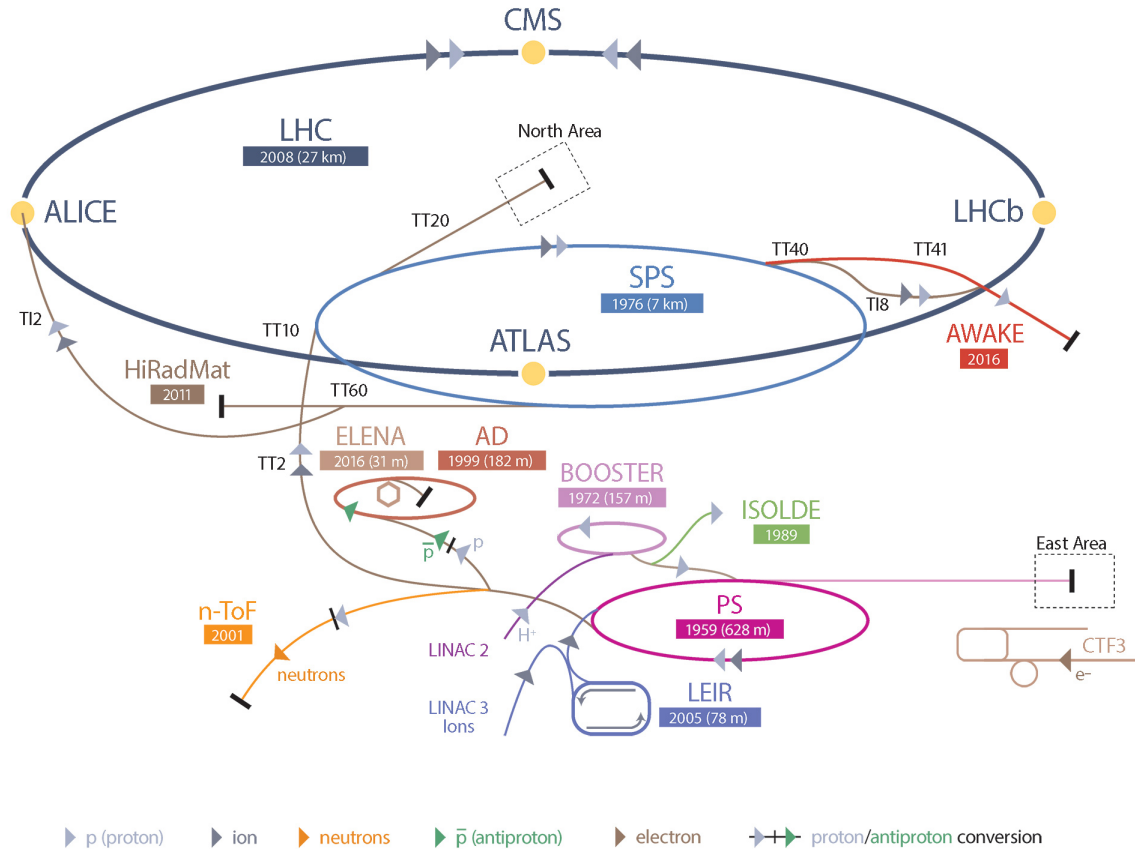


Figure 2.4: CERN accelerator complex.

2.2.1.1 Particle acceleration

The LHC is the last of a long series of accelerating devices. Before being accelerated by the LHC, the particles need to pass through different acceleration stages. All these acceleration stages are visible on Figure 2.4 and pictures of the accelerators are showed in Figure 2.5.

The story of accelerated protons at CERN starts with a bottle of hydrogen gas injected into the source chamber of the linear particle accelerator LINAC 2 2 in which a strong electric field strips the electron off the hydrogen molecules only to keep their nuclei, the protons. The cylindrical conductors, alternatively positively or negatively charged by radiofrequency cavities, accelerate protons by

1010 pushing them from behind and pulling them from the front and ultimately give them an energy of
1011 50 MeV, increasing their mass by 5% in the process.

1012

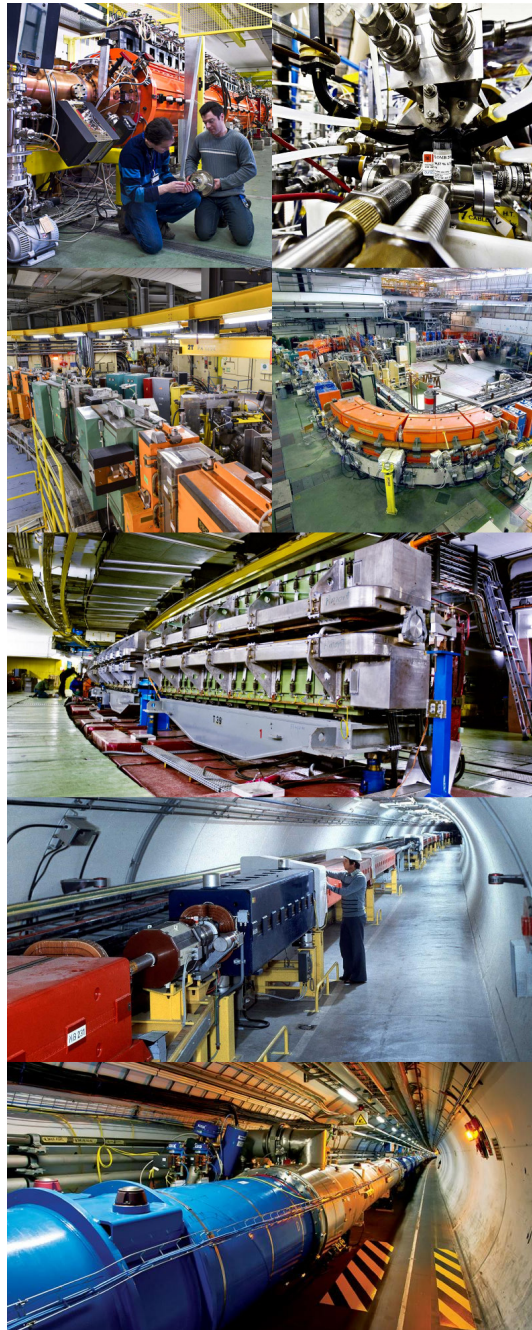


Figure 2.5: Pictures of the different accelerators. From top to bottom: first the LINAC 2 and the Pb source of LINAC 3. Then the Booster and the LEIR. Finally, the PS, the SPS and the LHC.

When exiting the LINAC 2, the protons are divided into 4 bunches and injected into the 4 superimposed synchrotron rings of the *Booster* where they are then accelerated to reach an energy of 1.4 GeV before being injected into the *PS*. Before the Booster was operational in 1972, the protons were directly injected into the *PS* from the LINAC 2 but the low injection energy limited the amount of protons that could be accelerated at once by the *PS*. With the Booster, the *PS* accepts approximately 100 times more particles.

The 4 proton bunches are thus sent as one to the *PS* where their energy eventually reaches 26 GeV. Since the 70s, the main goal of this 628 m circumference synchrotron has been to supply other machines with accelerated particles. Nowadays, not only the *PS* accelerates protons, it also accelerates heavy ions from the *Low Energy Ion Ring (LEIR)*. Indeed, the LHC experiments are not only designed to study *pp*-collisions but also *Pb*-collisions. Lead is first injected into the dedicated linear collider *LINAC 3*, that accelerate the ions using the same principle than LINAC 2. Electrons are stripped off the lead ions all along the acceleration process and eventually, only bare nuclei are injected in the *LEIR* whose goal is to transform the long ion pulses received into short dense bunches for LHC. Ions injected and stored in the *PS* were accelerated by the *LEIR* from 4.2 MeV to 72 MeV.

Directly following the *PS*, is finally the last acceleration stage before the LHC, the 7 km long *SPS*. The *SPS* accelerates the protons to 450 GeV and inject proton in both LHC accelerator rings that will increase their energy up to 7 TeV. When the LHC runs with heavy lead ions for *ALICE* and *LHCb*, ions are injected and accelerated to reach the energy of 2.8 TeV/A.

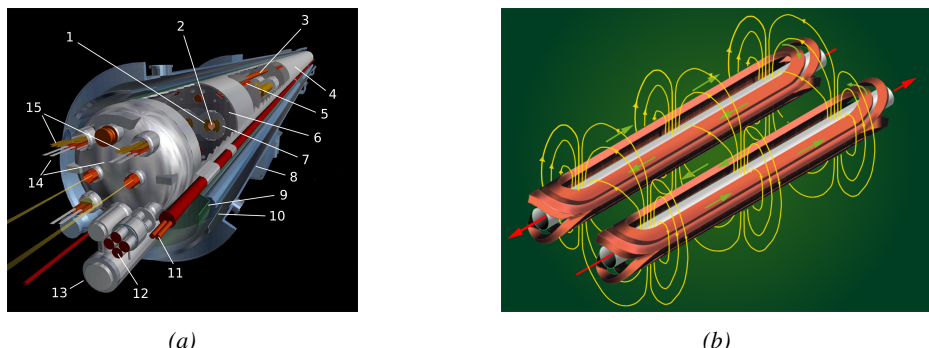


Figure 2.6: Figure 2.6a: schematics of the LHC cryodipoles. 1: Superconducting Coils, 2: Beam pipe, 3: Heat exchanger Pipe, 4: Helium-II Vessel, 5: Superconducting Bus-bar, 6: Iron Yoke, 7: Non-Magnetic Collars, 8: Vacuum Vessel, 9: Radiation Screen, 10: Thermal Shield, 11: Auxiliary Bus-bar Tube, 12: Instrumentation Feed Throughs, 13: Protection Diode, 14: Quadrupole Bus-bars, 15: Spool Piece Bus-bars. Figure 2.6b: magnetic field and resulting motion force applied on the beam particles.

The LHC beams are not continuous and are rather organised in bunch of particles. When in *pp*-collision mode, the beams are composed of 2808 bunches of 1.15×10^{11} protons separated by 25 ns. When in *Pb* collision mode, the 592 *Pb* bunches are on the contrary composed of 2.2×10^8 ions separated by 100 ns. The two parallel proton beams of the LHC are contained in a single twin-bore magnet due to the space restriction in the LEP tunnel. Indeed, building 2 completely separate accelerator rings next to each other was impossible. The dipoles of the 1232 twin-bore magnets are showed in Figure 2.6 alongside the magnetic field generated along the dipole section to accelerate the

1042 particles. The dipoles generate a nominal field of 8.33 T, needed to give protons and lead nucleons
 1043 their nominal energy. Some 392 quadrupoles, presented in Figure 2.7, are also used to focus to the
 1044 beams, as well as other multipoles to correct smaller imperfections.

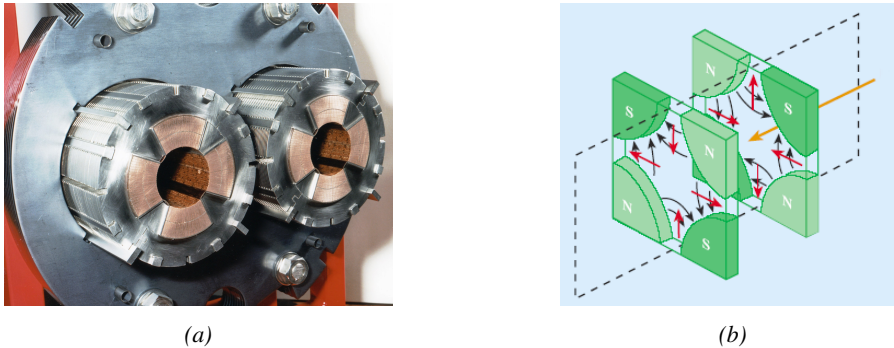


Figure 2.7: Figure 2.7a: picture of the LHC quadrupoles. Figure 2.7b: magnetic fields and resulting focussing force applied on the beam by 2 consecutive quadrupoles.

1045 2.2.1.2 High Luminosity LHC

1046 The very first proton beam successfully circulated in the LHC in September 2008 directly followed
 1047 by an incident leading to mechanical damage that would delay the LHC program for a year until
 1048 November 2009, the very first collisions at a center-of-mass energy of 7 TeV taking place in March
 1049 2010. The energy of the beam would be increased after a First Long Shutdown (LS1) starting early
 1050 2013 after less than 3 years of data taking. Nevertheless, this first data taking period at only 7 TeV
 1051 was sufficient to claim the discovery of a new particle compatible with the Higgs boson in July 2012.
 1052 During the 2 years of shutdown, the upgrade of the accelerator allowed for several maintainances
 1053 along the beam pipes, repair and consolidation of magnet connection and high-current splices. But
 1054 not only the LHC was upgraded. Indeed, the experiments at the 4 collision points also took the
 1055 advantage of this time to upgrade their system in prevision of the next LHC run (Run-II) until
 1056 2018 and the Second Long Shutdown (LS2) as the luminosity and energy of the beam would be
 1057 continuously increasing. By the end of Run-II, the luminosity will have reached twice its nominal
 1058 value when the center-of-mass energy has already got close to its nominal value by reaching an
 1059 historical 13 TeV for the first time in 2017.

1060 The next long shutdown will occur at the end of this year and will again be the occasion for sim-
 1061 ilar maintenance and consolidation in prevision of Run-III and the future upgrade of LS3. Still, the
 1062 main occupation of LS2 on LHC side will be the upgrade of LHC injectors. On the experiments side,
 1063 LHCb and ALICE will, in a very tight schedule, implement major upgrades while ATLAS and CMS
 1064 will wait until LS3 to upgrade their detectors in prevision of high luminosity LHC-Phase-II. ALICE
 1065 main challenge is an upgrade of their apparatus to cope with the 50 kHz $Pb - Pb$ collisions. Simi-
 1066 larly, LHCb will upgrade their frontend readout electronics to cope with the full 40 MHz collisions
 1067 delivered by LHC. ATLAS will perform standard maintenance and CMS will focus on the urgent up-
 1068 grade of the pixel detector and on the installation of new muon detectors in order to take profit of LS2
 1069 time to mitigate the upgrade of detectors foreseen during LS3. Run-III will start in 2021 with the LHC
 1070 at its nominal center-of-mass energy and will bring LHC-Phase-I to an end at the end of 2023. By
 1071 then the luminosity will only increase to reach 2.5 times the nominal luminosity but during these 3
 1072 years of run, the LHC will deliver as much integrated luminosity as what what brought during the al-

1073 most 7 years of both Run-I and II of data taking. Phase-I will end with an overall 300 fb^{-1} delivered.
 1074

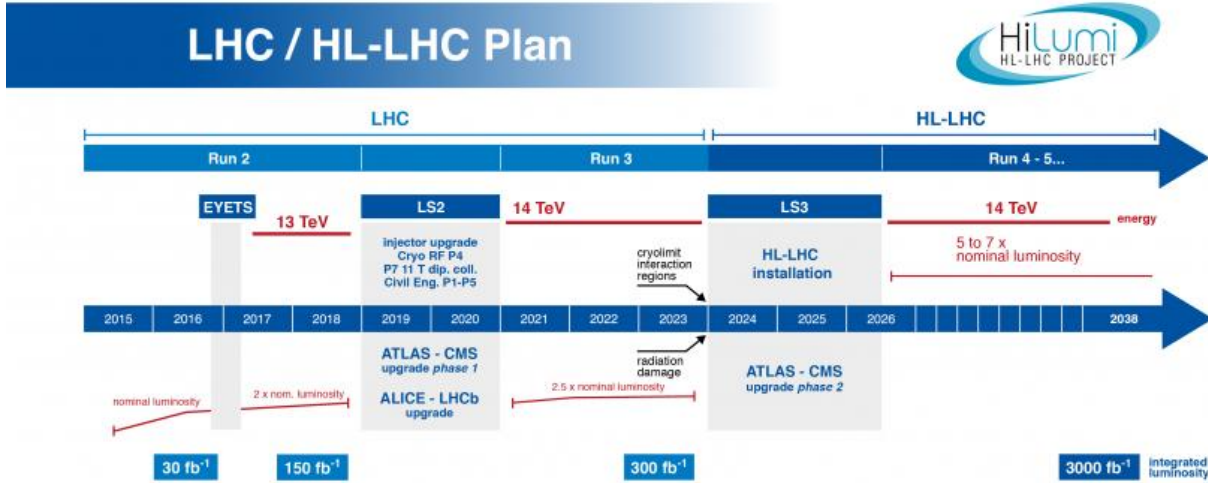


Figure 2.8: Detailed timeline of LHC and HL-LHC operation until 2028 and operation projection until 2038. This timeline only describes the operation plans after LS1.

1075 After approximately 15 years of operation, the LHC will undergo a new series of upgrade during
 1076 the LS3 in order to boost its discovery potential. This moment onward is what is referred to HL-LHC
 1077 or Phase-II as showed in Figure 2.8. The goal is to aim to a luminosity 5 to 7 times stronger than the
 1078 nominal one trying to reach even 10 times this value if possible. Increasing the luminosity means
 1079 that the beam size at the collision points needs to be reduced to boost the number of collisions per
 1080 bunch. For this purpose, new focusing and bending magnets and collimators will be installed at the
 1081 collision points as well as newly developed "*crab cavities*" that will tilt the particle bunches just
 1082 prior to the collisions by giving them transverse momentum and thus increasing their meeting area.
 1083 In addition, the full proton injection line will be upgraded.

1084 So far, the HL-LHC is expected to deliver an outstanding integrated luminosity of 3000 fb^{-1}
 1085 leading, in the case of Higgs studies, to measuring the couplings of the boson to a precision of
 1086 2 to 5% thanks to the estimated 15 millions of Higgs created each year providing a more precise
 1087 measurement of potential deviations from the theoretical predictions. SUSY studies would also see
 1088 their limits pushed away and could lead to a new breakthrough. SUSY is a particularly important
 1089 topic as it could give an answer to why the Higgs boson can stay so light while coupled to heavy
 1090 particles by introducing the contributions of the super partners on top of providing dark matter
 1091 candidates. Finally, the increase of luminosity will give the possibility to investigate "exotic" mode
 1092 like for example the models introducing extra dimensions to explain the hierarchy problem.

1093 On the experiments side, the pile-up (PU) will be increased up to 150 to 200 interactions per
 1094 bunch crossing in ATLAS and CMS, making necessary an strong upgrade of the trigger system and
 1095 of the inner trackers and of the calorimeters. Both ATLAS and CMS will also need to upgrade the
 1096 muon trigger at the level of the endcaps mainly focusing on the coverage near the beam line in order
 1097 to increase the detection acceptance and event selection. Moreover, the increased luminosity will
 1098 also lead to an increased background rate and a faster ageing of the detectors. This PhD work takes

1099 place into this very specific context of muon detector consolidation and certification for the HL-LHC
 1100 period in order to provide the CMS experiment with robust detectors that will live through the next
 1101 20 years of HL-LHC.

1102 2.2.2 CMS, a multipurpose experiment

1103 2.3 Muon Phase-II Upgrade

1104 After the more than two years lasting LS1, the LHC delivered its very first Run-II proton-proton
 1105 collisions early 2015. LS1 gave the opportunity to the LHC and to the its experiments to undergo
 1106 upgrades. The accelerator is now providing collisions at center-of-mass energy of 13 TeV and bunch
 1107 crossing rate of 40 MHz, with a peak luminosity exceeding its design value. During the first and
 1108 upcoming second LHC Long Shutdown, the CMS detector is also undergoing a number of upgrades
 1109 to maintain a high system performance [21].

1110 From the LHC Phase-2 or HL-LHC period onwards, i.e. past LS3, the performance degradation
 1111 due to integrated radiation as well as the average number of inelastic collisions per bunch crossing, or
 1112 pileup, will rise substantially and become a major challenge for the LHC experiments, like CMS that
 1113 are forced to address an upgrade program for Phase-II [22]. Simulations of the expected distribution
 1114 of absorbed dose in the CMS detector under HL-LHC conditions, show in figure 4.16 that detectors
 1115 placed close to the beamline will have to withstand high irradiation, the radiation dose being of the
 1116 order of a few tens of Gy.

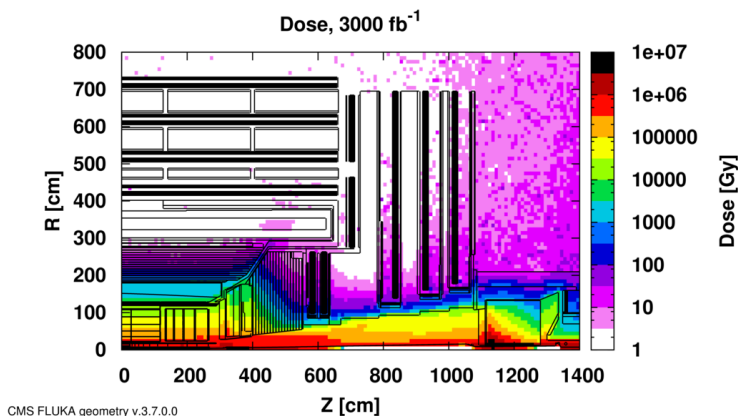


Figure 2.9: Absorbed dose in the CMS cavern after an integrated luminosity of 3000 fb. R is the transverse distance from the beamline and Z is the distance along the beamline from the Interaction Point at $Z=0$.

1117 The measurement of small production cross-section and/or decay branching ratio processes, such
 1118 as the Higgs boson coupling to charge leptons or the $B_s \rightarrow \mu^+ \mu^-$ decay, is of major interest and
 1119 specific upgrades in the forward regions of the detector will be required to maximize the physics
 1120 acceptance on the largest possible solid angle. To ensure proper trigger performance within the
 1121 present coverage, the muon system will be completed with new chambers. In figure 2.10 one can
 1122 see that the existing Cathode Strip Chambers (CSCs) will be completed by Gas Electron Multipliers
 1123 (GEMs) and Resistive Plate Chambers (RPCs) in the pseudo-rapidity region $1.6 < |\eta| < 2.4$ to
 1124 complete its redundancy as originally scheduled in the CMS Technical Proposal [23].

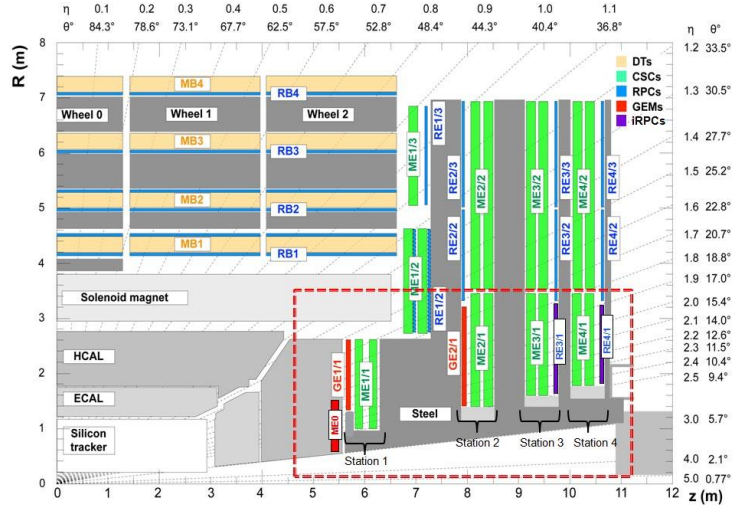


Figure 2.10: A quadrant of the muon system, showing DTs (yellow), RPCs (light blue), and CSCs (green). The locations of new forward muon detectors for Phase-II are contained within the dashed box and indicated in red for GEM stations (ME0, GE1/1, and GE2/1) and dark blue for improved RPC (iRPC) stations (RE3/1 and RE4/1).

1125 RPCs are used by the CMS first level trigger for their good timing performances. Indeed, a very
 1126 good bunch crossing identification can be obtained with the present CMS RPC system, given their
 1127 fast response of the order of 1 ns. In order to contribute to the precision of muon momentum mea-
 1128 surements, muon chambers should have a spatial resolution less or comparable to the contribution
 1129 of multiple scattering [21]. Most of the plausible physics is covered only considering muons with
 1130 $p_T < 100 \text{ GeV}$ thus, in order to match CMS requirements, a spatial resolution of $\mathcal{O}(\text{few mm})$ the
 1131 proposed new RPC stations, as shown by the simulation in figure 2.11. According to preliminary
 1132 designs, RE3/1 and RE4/1 readout pitch will be comprised between 3 and 6 mm and 5 η -partitions
 1133 could be considered.

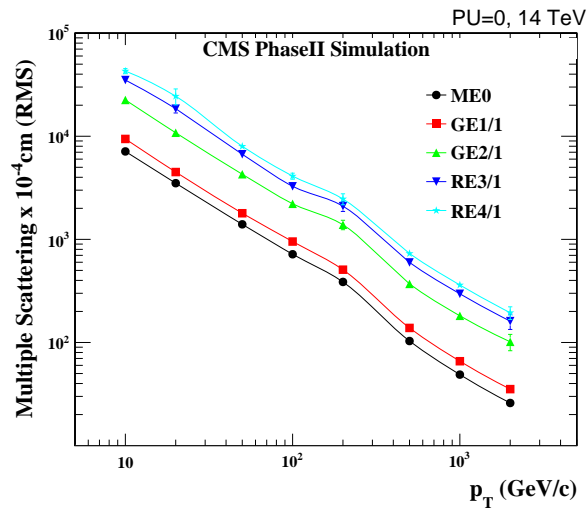


Figure 2.11: RMS of the multiple scattering displacement as a function of muon p_T for the proposed forward muon stations. All of the electromagnetic processes such as bremsstrahlung and magnetic field effect are included in the simulation.

3

1134

1135

Physics of Resistive plate chambers

1136 A Resistive Plate Chamber (RPC) is a gaseous detector using the same physical processes described
1137 in Chapter 3. It has been developed in 1981 by Santonico and Cardarelli [24], under the name of
1138 *Resistive Plate Counter*, as an alternative to the local-discharge spark counters proposed in 1978
1139 by Pestov and Fedotovich [25, 26]. Working with spark chambers implied using high-pressure gas
1140 and high mechanical precision which the RPC simplified by formerly using a gas mixture of argon
1141 and butane flowed at atmospheric pressure and a constant and uniform electric field propagated
1142 in between two parallel electrode plates. Moreover, a significant increase in rate capability was
1143 introduced by the use of electrode plate material with high bulk resistivity, preventing the discharge
1144 from growing throughout the whole gas gap. Indeed, the effect of using resistive electrodes is that
1145 the constant electric field is locally canceled out by the development of the discharge, limiting its
1146 growth.

1147 Through its development history, different operating modes [27–29] and new detector designs [30–
1148 32] have been discovered, leading to further improvement of the rate capability of such a detector.
1149 Moreover, the addition of SF_6 into the gas mix improved the stability of operation of the RPC [33,
1150 34].

1151 The low developing costs and easily achievable large detection areas offered by RPCs, as well as
1152 the wide range of possible designs, made them a natural choice to as muon chambers and/or trigger
1153 detectors in multipurpose experiments such as CMS [21] or ATLAS [35], time-of-flight detectors in
1154 ALICE [36], calorimeter with CALICE [37] or even detectors for volcanic muography with ToMu-
1155 Vol [38].

1156 3.1 Principle

1157 RPCs are ionisation detectors composed of two parallel resistive plate electrodes in between which
1158 a constant electric field is set. The space in between the electrodes, referred as *gap*, is filled with a
1159 dense gas that is used to generate primary ionization into the gas volume. The free charge carriers
1160 (electrons and cations) created by the ionization of the gas molecules are then accelerated towards

¹¹⁶¹ the electrodes by the electric field, as shown in Figure 3.1 [39].

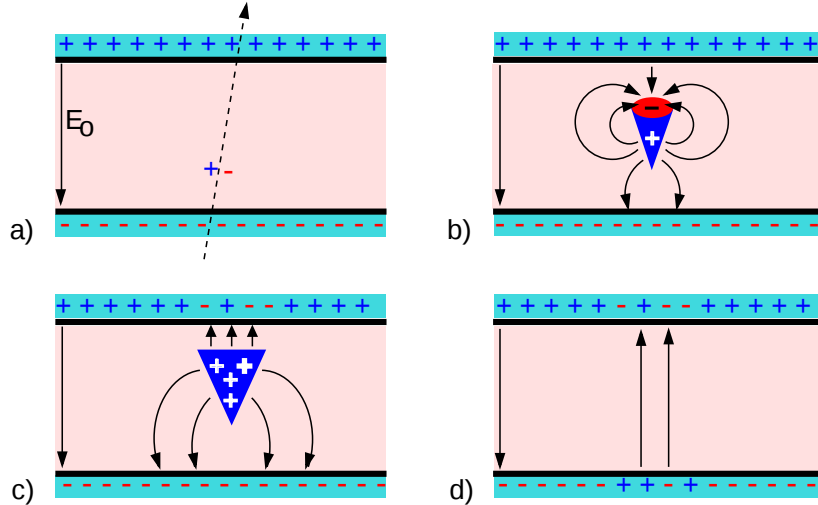


Figure 3.1: Different phases of the avalanche development in the RPC gas volume subjected to a constant electric field E_0 . a) An avalanche is initiated by the primary ionisation caused by the passage of a charged particle through the gas volume. b) Due to its growing size, the avalanche starts to locally influence the electric field. c) The electrons, lighter than the cations reach the anode first. d) The ions reach the cathode. While the charges have not recombined, the electric field in the small region around the avalanche stays affected and locally blind the detector.

¹¹⁶² RPCs being passive detectors, a current on pick-up copper read-out placed outside of the gas
¹¹⁶³ volume is induced by the charge accumulation during the growth of the avalanche. As a result,
¹¹⁶⁴ the time resolution of the detector is substantially increased as the output signal is generated while
¹¹⁶⁵ the electrons are still in movement. The advantage of a constant electric field, over multi-wire
¹¹⁶⁶ proportional chambers, is that the electrons are being fully accelerated from the moment charge
¹¹⁶⁷ carriers are freed and feel the full strength of the electric field that doesn't depend on the distance to
¹¹⁶⁸ the readout and that the output signal doesn't need for the electrons to be physically collected.

¹¹⁶⁹ The typical gas mixture RPCs are operated with is generally composed of 3 gas compounds.

- ¹¹⁷⁰ • Tetrafluoroethane ($C_2F_4H_2$), also referred to as *Freon*, is the principal compound of the RPC
¹¹⁷¹ gas mixtures, with a typical fraction above 90%. It is used for it's high effective Townsend
¹¹⁷² coefficient and the great average fast charge that allows to operate the detector with a high
¹¹⁷³ threshold with respect to argon, for example, that has similar effective Townsend coefficient
¹¹⁷⁴ but suffers from a lower fast charge. To operate with similar conditions, argon would require a
¹¹⁷⁵ higher electric field leading to a higher fraction of streamers, thus limiting the rate capability
¹¹⁷⁶ of the detector [40].
- ¹¹⁷⁷ • Isobutane (i- C_4H_{10}), only present in a few percent in the gas mixtures, is used for its UV
¹¹⁷⁸ quenching properties [41] helping to prevent streamers due to UV photon emission during the
¹¹⁷⁹ avalanche growth.
- ¹¹⁸⁰ • Sulfur hexafluoride, (SF_6), referred to simply as *SF6*, is used in very little quantities for its
¹¹⁸¹ high electronegativity. Excess of electrons are being absorbed by the compound and streamers

are suppressed [34]. Nevertheless, a fraction of SF_6 higher than 1% will not bring any extra benefit in terms of streamer cancelation power but will lead to higher operating voltage [33], as can be understood through Figure 3.2.

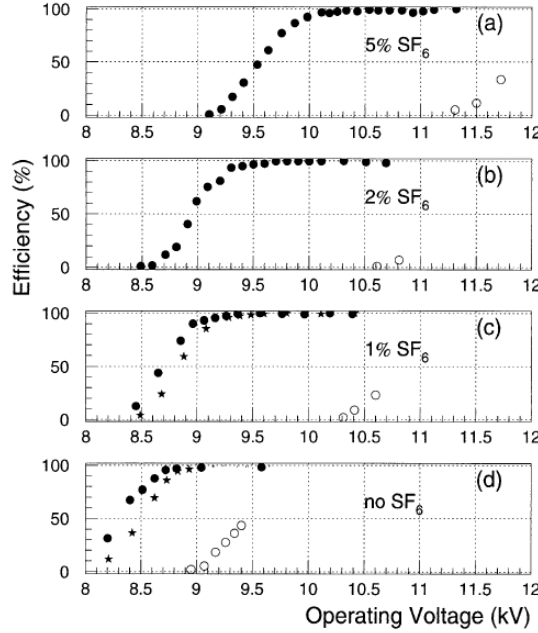


Figure 3.2: Effeciency (circles and stars with 30 mV and 100 mV thresholds respectively) and streamer probability (opened circles) as function of the operating voltatge of a 2 mm single gap HPL RPC flushed with a gas mixture containing (a) 5%, (b) 2%, (c) 1% and (d) no SF_6 [33].

After an avalanche developed in the gas, a time long compared to the development of a discharge is needed to recombine the charge carriers in the electrode material due to their resistivity. This property has the advantage of affecting the local electric field and avoiding sparks in the detector but, on the other hand, the rate capability is intrinsically limited by the time constant τ_{RPC} of the detector. Using a quasi-static approximation of Maxwell's equations for weakly conducting media, it can be shown that the time constant τ_{RPC} necessary to the charge recombination at the interface in between the electrode and the gas volume is given by the Formula 3.1 [42].

$$\tau_{RPC} = \frac{\epsilon_{electrode} + \epsilon_{gas}}{\sigma_{electrode} + \sigma_{gas}} \quad (3.1)$$

A gas can be assimilated to vacuum, leading to $\epsilon_{gas} = \epsilon_0$ and $\sigma_{gas} = 0$, and the electrodes permittivity and conductivity can be written as $\epsilon_{electrode} = \epsilon_r \epsilon_0$ and $\sigma_{electrode} = 1/\rho_{electrode}$, showing the strong dependence of the time constant to the electrodes resistivity in Formula 3.2.

$$\tau_{RPC} = (\epsilon_r + 1)\epsilon_0 \times \rho_{electrode} \quad (3.2)$$

Very few materials with a low enough resistivity exist in nature. The resistivity targeted to build RPCs ranges from 10^9 to $10^{12} \Omega \cdot \text{cm}$. The most common RPC electrode materials are displayed in Table 3.1. When the doped glass and ceramics can offer short time constants of the order of 1 ms,

1198 the developing cost of such materials is quite high due to the very low demand. Thus, High-pressure
 1199 laminate (HPL) is often the choice for high rate experiments using very large RPC detection areas.
 1200 Other experiments working at cosmic muon fluxes can safely operate with ordinary float glass.

Material	$\rho_{electrode}$ ($\Omega \cdot \text{cm}$)	ϵ_r	τ_{RPC} (ms)
Float glass	10^{12}	~ 7	~ 700
High-pressure laminate	10^{10} to 10^{12}	~ 6	~ 6 to 600
Doped glass (LR S)	10^9 to 10^{11}	~ 10	~ 1 to 100
Doped ceramics (SiN/SiC)	10^9	~ 8.5	~ 1
Doped ceramics (Ferrite)	10^8 to 10^{12}	~ 20	~ 0.2 to 2000

Table 3.1: Properties of the most used electrode materials for RPCs.

1201 3.1.1 Electron drift velocity

1202 Talk about the electron drift velocity and mention the time resolution of RPCs.

1203 3.2 Rate capability and time resolution of Resistive Plate Cham- 1204 bers

1205 As already previously discussed, the electrode material plays a key role in the max intrinsic rate
 1206 capability of RPCs. R&D is being done to develop at always cheaper costs material with lower
 1207 resistivity. Nevertheless, the amount of charge released, i.e. the size of the discharge, if reduced
 1208 leads to a smaller blind area in the detector, increasing the rate capability of the detector.

1209 3.2.1 Operation modes

1210 RPCs where developed early 1980s. At that time it was using an operating mode now referred to
 1211 as *streamer mode*. Streamers are large discharges that develop in between the 2 electrodes enough
 1212 to locally discharge the electrodes. If the electric field inside of the gas volume is strong enough,
 1213 with electrons being fast compared to ions, a large and dense cloud of positive ions will develop
 1214 nearby the anode and extend toward the cathode while the electrons are being collected, eventually
 1215 leading to a streamer discharge due to the increase of field seen at the cathode. the field is then strong
 1216 enough so that electrons are pulled out of the cathode. Electrodes, though they are a unique volume
 1217 of resistive material, can be assimilated to capacitors. At the moment an electric field is applied in
 1218 between their outer surfaces, the charge carriers inside of the volume will start moving leading to
 1219 a situation where there is no voltage across the electrodes and a higher density of negative charges,
 1220 i.e. electrons, on the inner surface of the cathode. Finally, when a streamer discharge occurs, these
 1221 electrons are partially released in the gas volume contributing to increase the discharge strength until
 1222 the formation of a conductive plasma, the streamer. This can be understood through Figure 3.3 [27].
 1223 Streamer signals are very convenient in terms of read-out as no amplification is required with output
 1224 pulses amplitudes of the order of a few tens to few hundreds of mV as can be seen on Figure 3.4.

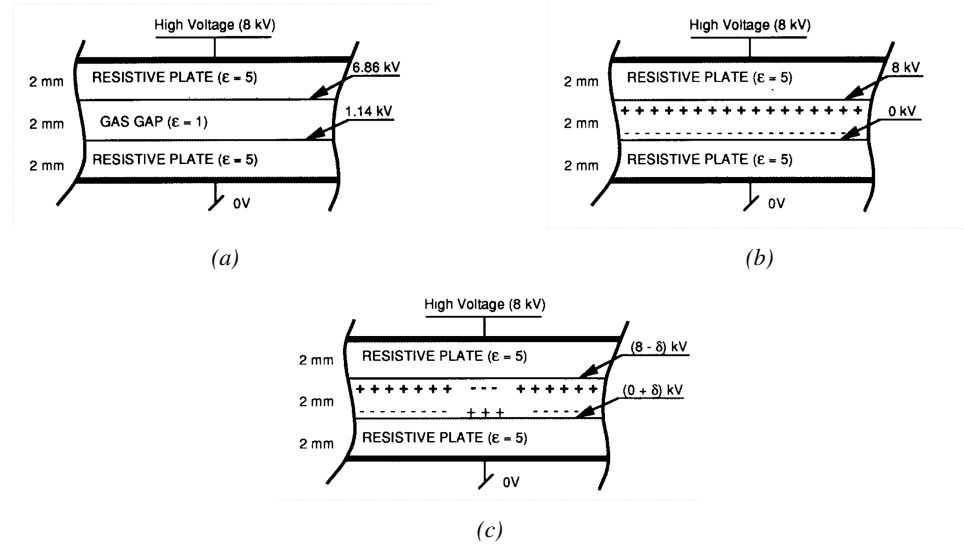


Figure 3.3: Movement of the charge carriers in an RPC. Figure 3.3a: Voltage across an RPC whose electrode have a relative permittivity of 5 at the moment the tension is applied. Figure 3.3b: After the charge carriers moved, the electrodes are charged and there is no voltage drop over the electrodes anymore. The full potential is applied on the gas gap only. Figure 3.3c: The streamer discharge initiated by a charged particle transports electrons and cations towards the anode and cathode respectively.

When the electric field is reduced though, the electronic gain is small until the electrons get close enough to the anode and the positive ion cloud is much smaller. The electric field cannot rise to the point a field emission of electrons on the cathode is possible. The resulting signal is weak, of the order of a few mv as shown on Figure 3.4, and requires amplification. This is the *avalanche mode* of RPC operation.

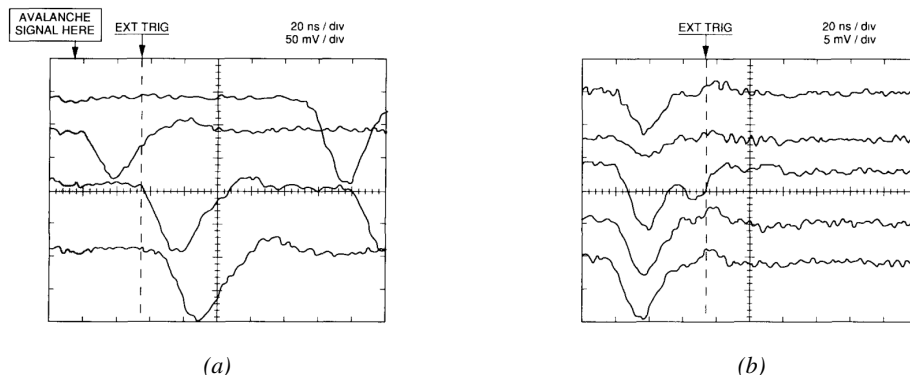


Figure 3.4: Typical oscilloscope pulses in streamer mode (Figure 3.4a) and avalanche mode (Figure 3.4b). In the case of streamer mode, the very small avalanche signal is visible.

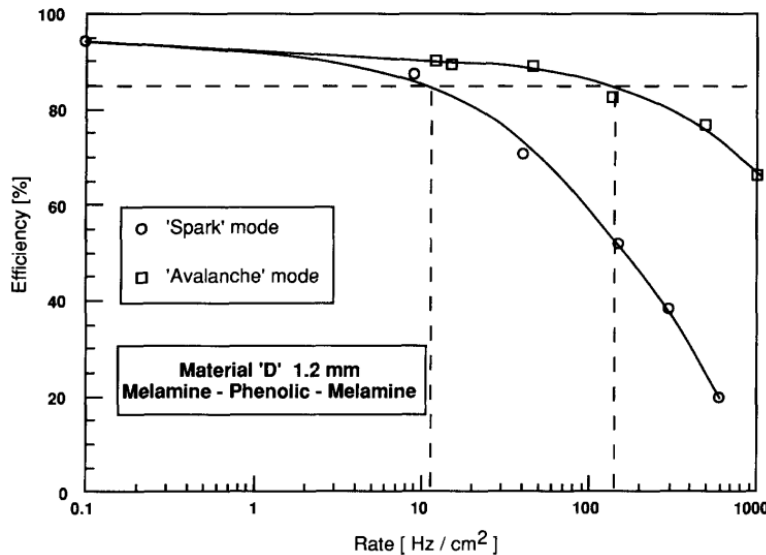


Figure 3.5: Rate capability comparison for the streamer and avalanche mode of operation. An order of magnitude in rate capability for a maximal efficiency drop of 10% is gained by using the avalanche mode over the streamer mode.

This mode offers a higher rate capability by providing smaller discharges that don't affect the electrodes charge and are more locally contained in the gas volume as was demonstrated by Crotty with Figure 3.5 [27]. The detector only stays locally blind the time the charge carriers are recombined and there is no need for electrode recharge which is a long process affecting a large portion of the detector. Another advantage of avalanche signals over streamer is the great time consistency. Figure 3.4 shows very clearly that avalanche signals have a very small time jitter. This is a natural choice for high rate experiments.

3.2.2 Detector designs and performance

Different RPC design have been used and each of them present its own advantages. Historically, the first type of RPC to have been developed is what is referred now to *narrow gap* RPC [24, 43]. After the avalanche mode has been discovered [27], it has been proven that increasing the width of the gas gap lead to higher rate capability, due to lower charge deposition per avalanche, and lower power dissipation [43]. Nevertheless, by increasing the gas gap width, the time resolution of the detector decreases. This is a natural result if the increase of active gas volume in the detector is taken into account. Indeed, for a given threshold, only the small fraction of gas closest to the cathode will provide enough gain to have a detectable signal. In the case of a wider gas volume, the active region is then larger and a larger time jitter is introduced with the variation of starting position of the avalanche, as discussed in [30]. To solve improve both the time resolution and the rate capability, different methods were used trying to get advantages of both narrow and wide gap RPCs.

1249 **3.2.2.1 Double-gap RPC**

1250 Double-gap RPCs are made out of 2 narrow RPC detectors. The 2 RPC gaps are stacked on top of
 1251 each other as shown in Figure 3.6. This detector layout, popularized by the two multipurpose experiments
 1252 CMS [21] and ATLAS [35] at LHC, can be used as an OR system in which each individual
 1253 chamber participates in the output signal. The gain of such a detector is greatly reduced with respect
 1254 to single-gap RPCs with an efficiency plateau reached at lower voltage, as visible on Figure 3.7.

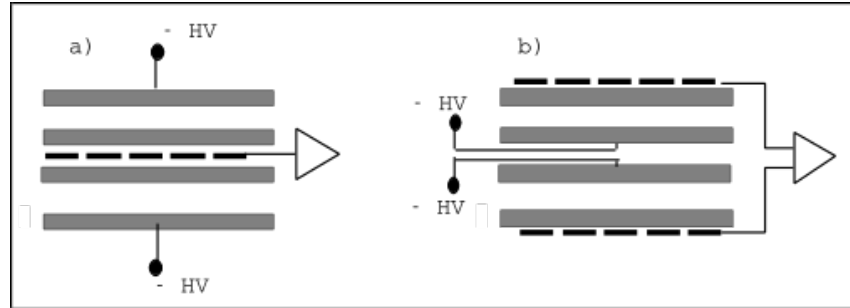


Figure 3.6: Possible double-gap RPC layouts: a) "standard" 1D double-gap RPC, as used in CMS experiment, where the anodes are facing each other and a 1D read-out plane is sandwiched in between them, b) double read-out double-gap RPC as used in ATLAS experiment, where the cathodes are facing each other and 2 read-out planes are used on the outer surfaces. This last layout can offer the possibility to use a 2D reconstruction by using orthogonal read-out planes.

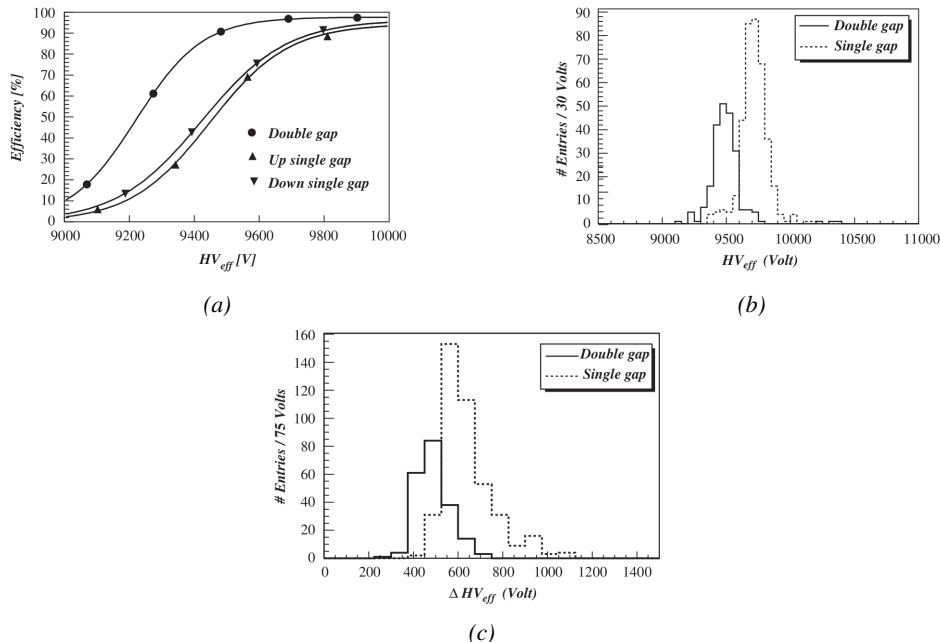


Figure 3.7: Comparison of performance of CMS double and single gap RPCs using cosmic muons [44]. Figure 3.7a: Comparison of efficiency sigmoids. Figure 3.7b: Voltage distribution at 95% of maximum efficiency. Figure 3.7c: $\Delta_{10\%}^{90\%}$ distribution.

1255 **3.2.2.2 Multigap RPC (MRPC)**

1256 MRPCs are layouts in which floating sub electrode plates are placed into a wide gap RPC to divide
 1257 the gas volume and create a sum of narrow gaps [30, 31]. The time resolution of such a detector can
 1258 reach of few tens of ps, with gas gaps of the order of a few hundred μm as shown in Figure 3.8
 1259 representing ALICE Time-of-flight (ToF) MRPCs.

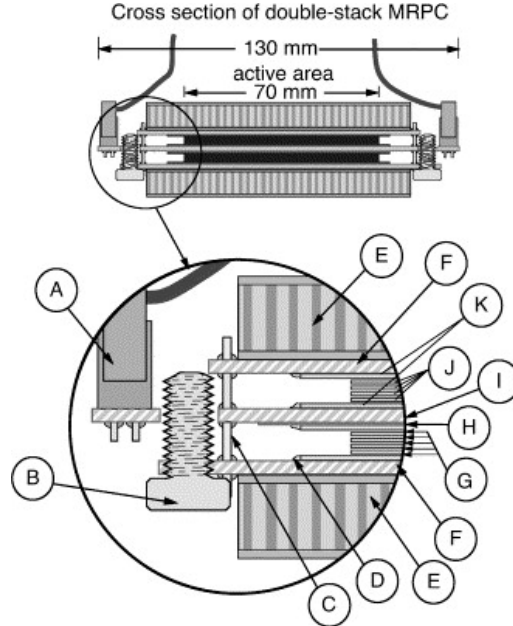


Figure 3.8: Presentation of ALICE MRPC using $250 \mu\text{m}$ gas gaps, $620 \mu\text{m}$ outer glass electrodes and $550 \mu\text{m}$ inner floating electrodes. More details on the labels are given in [45].

1260 Sometimes used as a double multigap RPC, taking advantage of the OR of double gap RPCs,
 1261 the MRPC is mainly used as ToF detector [45–49] due to its excellent timing properties that allow
 1262 to perform particle identification as explained by Williams in [50]. The principle of particle iden-
 1263 tification using ToF is simply the measurement of the velocity of a particle. Indeed, particles are
 1264 defined by their mass (for the parameter of interest here, their electric charge being measured using
 1265 the bending angle of the particles traveling through a magnetic field) and this mass can be calculated
 1266 by measuring the velocity β and momentum of the particle:

$$\beta = \frac{p}{\sqrt{p^2 + m^2}} \quad (3.3)$$

1267 Intuitively, it is trivial to understand that 2 different particles having the same momentum will
 1268 have a different velocity due to the mass difference and thus a different flight time T_1 and T_2 through
 1269 the detector and this is used to separate and identify particles. The better the time resolution of the
 1270 ToF system used, the stronger will the separation be:

$$T = \frac{L}{v} = \frac{L}{c \cdot \beta}, \quad \Delta T = T_1 - T_2 = \frac{L}{c} \left(\sqrt{1 + m_1^2/p^2} - \sqrt{1 + m_2^2/p^2} \right) \cong (m_1^2 - m_2^2) \frac{L}{2cp^2} \quad (3.4)$$

1271 An example of particle identification is given for the case of STAR experiment in Figure 3.9.

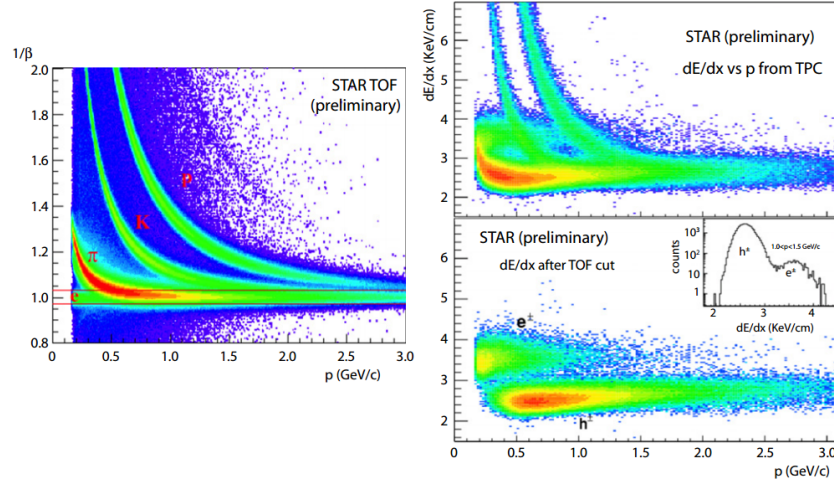


Figure 3.9: Particle identification applied to electrons in the STAR experiment. The identification is performed combining ToF and dE/dx measurements [50].

1272 Another benefice of using such small gas gaps is the strong reduction of the average avalanche
1273 volume and thus of the blind spot on MRPCs leading to an improved rate capability. Multigaps can
1274 sustain backgrounds of several kHz/cm² as demonstrated in Figure 3.10.

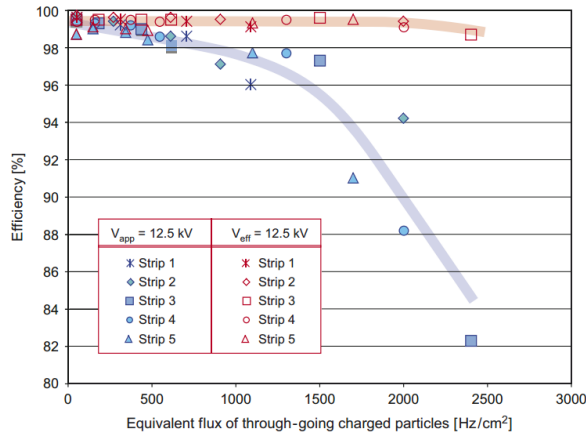


Figure 3.10: Comparison of the detector performance of ALICE ToF MRPC [51] at fixed applied voltage (in blue) and at fixed effective voltage (in red). The effective voltage is kept fixed by increasing the applied voltage accordingly to the current drawn by the detector.

1275 3.2.2.3 Charge distribution and performance limitations

1276 The direct consequence of the different RPC layouts is a variation of intrinsic time resolution of the
1277 RPC as the gap size decreases. An advantage is given to multigaps whose design use sub-millimeter
1278 gas volumes providing very consistent signals.

1279 On the charge spectrum point of view, each layout has its own advantages. When the double-gap
 1280 has the highest induced over drifting charge ratio, as seen in Figure 3.11, the multigap has a charge
 1281 spectrum strongly detached from the origin, as visible in Figure 3.12. A high induced over drifting
 1282 charge ratio means that the double gap can be safely operated at high threshold or that at similar
 1283 threshold it can be operated with a twice smaller drifting charge, meaning a higher rate capability.
 1284 On the other hand, the strong detachment of the charge spectrum from the origin in the MRPC case
 1285 allows to reach a higher efficiency with increasing threshold as most of the induced charge is not low
 1286 due to the convolution of several single gap spectra. The range of stable efficiency increases with
 1287 the number of gap, as presented in Figure 3.13.

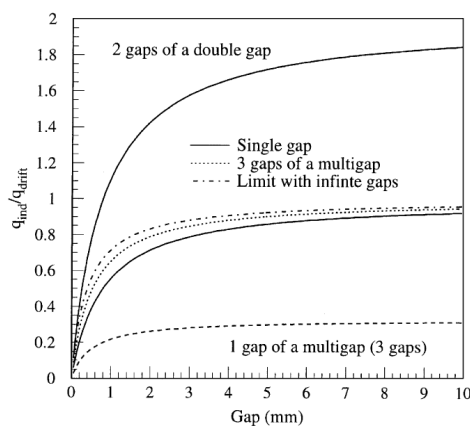


Figure 3.11: Ratio between total induced and drifting charge have been simulated for single gap, double-gap and multigap layouts [52]. The total induced charge for a double-gap RPC is a factor 2 higher than for a multigap.

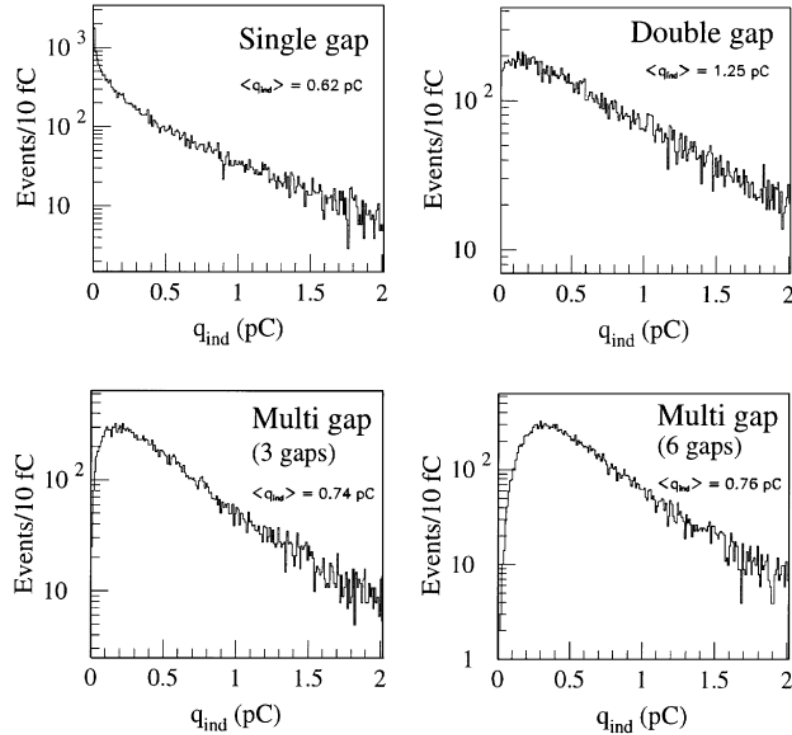


Figure 3.12: Charge spectra have been simulated for single gap, double-gap and multigap layouts [52]. It appears that when single gap shows a decreasing spectrum, double and multigap layouts exhibit a spectrum whose peak is detached from the origin. The detachment gets stronger as the number of gaps increases.

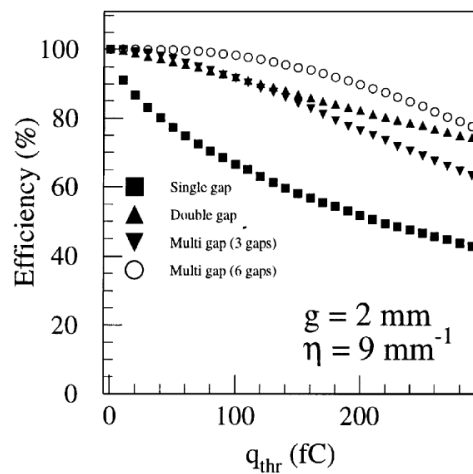


Figure 3.13: The maximal theoretical efficiency is simulated for single gap, double-gap and multigap layouts [52] at a constant gap thickness of 2 mm and using an effective Townsend coefficient of 9 mm^{-1} .

₁₂₈₈ **3.3 Signal formation**

₁₂₈₉ **3.4 Gas transport parameters**

4

1290

1291

1292

Longevity studies and Consolidation of the present CMS RPC subsystem

1293 4.1 Resistive Plate Chambers at CMS

1294 4.1.1 Overview

1295 The Resistive Plate Chambers (RPC) system, located in both barrel and endcap regions, provides a
1296 fast, independent muon trigger with a looser p_T threshold over a large portion of the pseudorapidity
1297 range ($|\eta| < 1.6$) [add reconstruction].

1298

1299 During High-Luminosity LHC (HL-LHC) operations the expected conditions in terms of back-
1300 ground and pile-up will make the identification and correct P_T assignment a challenge for the Muon
1301 system. The goal of RPC upgrade is to provide additional hits to the Muon system with precise tim-
1302 ing. All these informations will be elaborated by the trigger system in a global way enhancing the
1303 performance of the trigger in terms of efficiency and rate control. The RPC Upgrade is based on two
1304 projects: an improved Link Board System and the extension of the RPC coverage up to $|\eta| = 2.4$.
1305 [FIXME 2.4 or 2.5?]

1306 The Link Board system, that will be described in section xxx, is responsible to process, syn-
1307 chronize and zero-suppress the signals coming from the RPC front end boards. The Link Board
1308 components have been produced between 2006 and 2007 and will be subjected to aging and failure
1309 in the long term. The upgraded Link Board system will overcome the aging problems described in
1310 section xxx and will allow for a more precise timing information to the RPC hits from 25 to 1 ns [ref
1311 section xxx].

1312 The extension of the RPC system up to $|\eta| = 2.1$ was already planned in the CMS TDR [ref
1313 cmstdr] and staged because of budget limitations and expected background rates higher than the rate
1314 capability of the present CMS RPCs in that region. An extensive R&D program has been done in
1315 order to develop an improved RPC that fulfills the CMS requirements. Two new RPC layers in the
1316 innermost ring of stations 3 and 4 will be added with benefits to the neutron-induced background

1317 reduction and efficiency improvement for both trigger and offline reconstruction.

1318 4.1.2 The present RPC system

1319 The RPC system is organized in 4 stations called RB1 to RB4 in the barrel region, and RE1 to RE4
 1320 in the endcap region. The innermost barrel stations, RB1 and RB2, are instrumented with 2 layers
 1321 of RPCs facing the innermost (RB1in and RB2in) and outermost (RB1out and RB2out) sides of the
 1322 DT chambers. Every chamber is then divided from the read-out point of view into 2 or 3 η partitions
 1323 called “rolls”. The RPC system consist of 480 barrel chambers and 576 endcap chambers. Details
 1324 on the geometry are discussed in the paper [ref to geo paper].

1325 The CMS RPC chamber is a double-gap, operated in avalanche mode to ensure reliable operation
 1326 at high rates. Each RPC gap consists of two 2-mm-thick resistive High-Pressure Laminate (HPL)
 1327 plates separated by a 2-mm-thick gas gap. The outer surface of the HPL plates is coated with a thin
 1328 conductive graphite layer, and a voltage is applied. The RPCs are operated with a 3-component,
 1329 non-flammable gas mixture consisting of 95.2% freon ($C_2H_2F_4$, known as R134a), 4.5% isobutane
 1330 ($i-C_4H_{10}$), and 0.3% sulphur hexafluoride (SF_6) with a relative humidity of 40% - 50%. Readout
 1331 strips are aligned in η between the 2 gas gaps. [\[Add a sentence on FEBs.\]](#)

1332 The discriminated signals coming from the Front End boards feed via twisted cables (10 to 20 m
 1333 long) the Link Board System located in UXC on the balconies around the detector. The Link System
 1334 consist of the 1376 Link Boards (LBs) and the 216 Control Boards (CBs), placed in 108 Link Boxes.
 1335 The Link Box is a custom crate (6U high) with 20 slots (for two CBs and eighteen LBs). The Link
 1336 Box contains custom backplane to which the cables from the chambers are connected, as well as the
 1337 cables providing the LBs and CBs power supply and the cables for the RPC FEBs control with use
 1338 of the I2C protocol (trough the CB). The backplane itself contains only connectors (and no any other
 1339 electronic devices).

1340 The Link Board has 96 input channels (one channel corresponds to one RPC strip). The input
 1341 signals are the ~ 100 ns binary pulses which are synchronous to the RPC hits, but not to the LHC
 1342 clock (which drives the entire CMS electronics). Thus the first step of the FEB signals processing
 1343 is synchronization, i.e. assignment of the signals to the BXes (25 ns periods). Then the data are
 1344 compressed with a simple zero-suppressing algorithm (the input channels are grouped into 8 bit
 1345 partitions, only the partitions with at least one nonzero bit are selected for each BX). Next, the non-
 1346 empty partitions are time-multiplexed i.e. if there are more than one such partition in a given BX,
 1347 they are sent one-by-one in consecutive BXes. The data from 3 neighbouring LBs are concentrated
 1348 by the middle LB which contains the optical transmitter for sending them to the USC over a fiber at
 1349 1.6 Gbps.

1350 The Control Boards provide the communication of the control software with the LBs via the
 1351 FEC/CCU system. The CBs are connected into token rings, each ring consists of 12 CBs of one
 1352 detector tower and a FEC mezzanine board placed on the CCS board located in the VME crate in
 1353 the USC. In total, there are 18 rings in the entire Link System. The CBs also perform automatic
 1354 reloading of the LB's firmware which is needed in order to avoid accumulation of the radiation
 1355 induced SEUs in the LBs firmware.

1356 Both LBs and CB are based on the Xilinx Spartan III FPGAs, the CB additionally contains
 1357 radiation-tolerant (FLASH based) FPGA Actel ProAsicPlus.

1358 The High Voltage power system is located in USC, not exposed to radiation and easily accessible
 1359 for any reparation. A single HV channel powers 2 RPC chambers both in the barrel and endcap
 1360 regions. The Low Voltage boards are located in UXC on the balconies and provide the voltage to the

¹³⁶¹ front end electronics.

¹³⁶² 4.1.3 Pulse processing of CMS RPCs

¹³⁶³ Signals induced by cosmic particle in the RPC strips are shaped by standard CMS RPC Front-End
¹³⁶⁴ Electronics (FEE) following the scheme of Figure 4.1. On a first stage, analogic signals are amplified
¹³⁶⁵ and then sent to the Constant Fraction Discriminator (CFD) described in Figure 4.2. At the end of
¹³⁶⁶ the chain, 100 ns long pulses are sent in the LVDS output. These output signal are sent on one side to
¹³⁶⁷ a V1190A Time-to-Digital Converter (TDC) module from CAEN and on the other to an OR module
¹³⁶⁸ to count the number of detected signals. Trigger and hit coïncidences are monitored using scalers.
¹³⁶⁹ The TDC is used to store the data into ROOT files. These files are thus analysed to understand the
¹³⁷⁰ detectors performance.

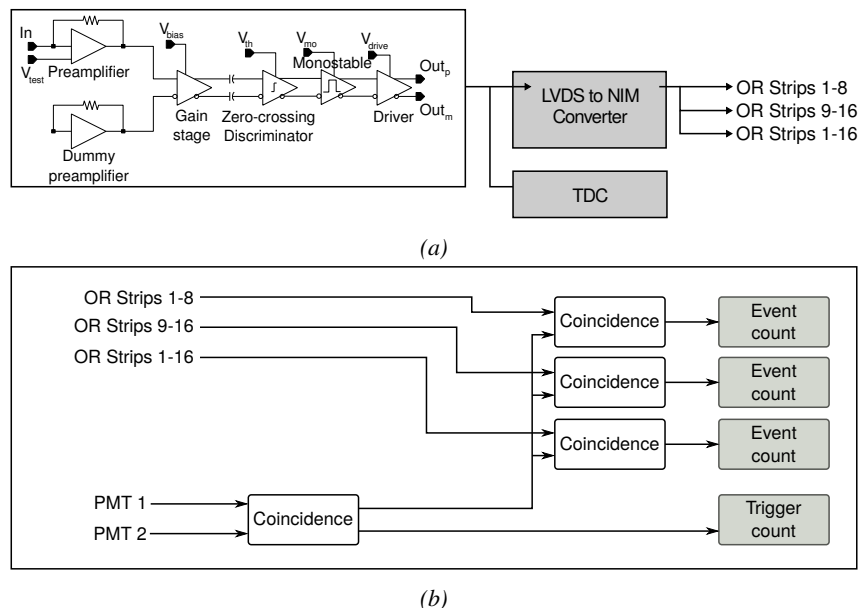


Figure 4.1: Signals from the RPC strips are shaped by the FEE described on Figure 4.1a. Output LVDS signals are then read-out by a TDC module connected to a computer or converted into NIM and sent to scalers. Figure 4.1b describes how these converted signals are put in coincidence with the trigger.

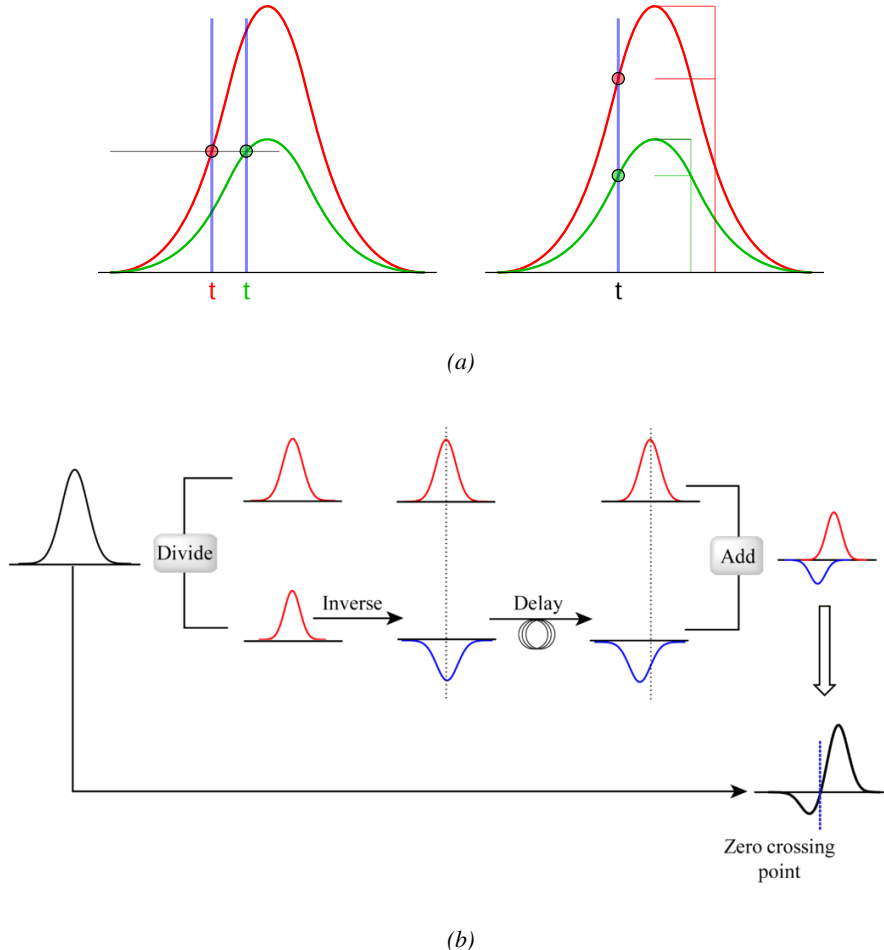


Figure 4.2: Description of the principle of a CFD. A comparison of threshold triggering (left) and constant fraction triggering (right) is shown in Figure 4.2a. Constant fraction triggering is obtained thanks to zero-crossing technique as explained in Figure 4.2b. The signal arriving at the input of the CFD is split into three components. A first one is delayed and connected to the inverting input of a first comparator. A second component is connected to the noninverting input of this first comparator. A third component is connected to the noninverting input of another comparator along with a threshold value connected to the inverting input. Finally, the output of both comparators is fed through an AND gate.

4.2 Testing detectors under extreme conditions

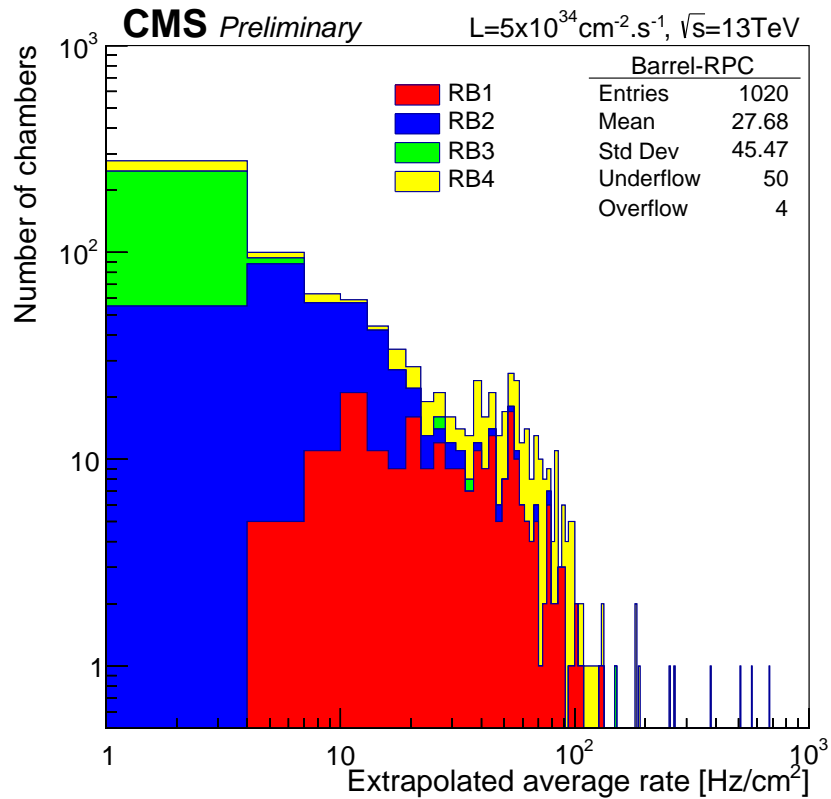
The upgrade from LHC to HL-LHC will increase the peak luminosity from $10^{34} \text{ cm}^{-2} \text{ s}^{-1}$ to reach $5 \times 10^{34} \text{ cm}^{-2} \text{ s}^{-1}$, increasing in the same way the total expected background to which the RPC system will be subjected to. Composed of low energy gammas and neutrons from $p\text{-}p$ collisions, low momentum primary and secondary muons, puch-through hadrons from calorimeters, and particles produced in the interaction of the beams with collimators, the background will mostly affect the regions of CMS that are the closest to the beam line, i.e. the RPC detectors located in the endcaps.

[To update.]

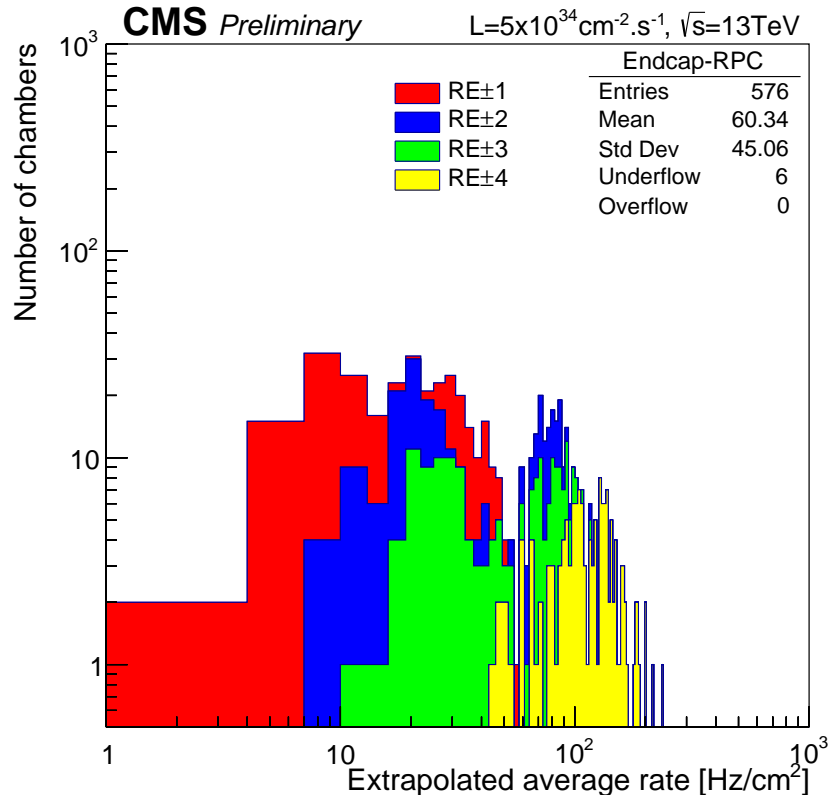
1379

1380 The 2016 data allowed to study the values of the background rate in all RPC system. In Fig-
1381 ure 4.3, the distribution of the chamber background hit rate per unit area is shown at a luminosity
1382 of $5 \times 10^{34} cm^{-2}.s^{-1}$ linearly extrapolating from data collected in 2016 [ref mentioning the linear
1383 dependency of rate vs lumi]. The maximum rate per unit area at HL-LHC conditions is expected to
1384 be of the order of $600 Hz/cm^2$ (including a safety factor 3). Nevertheless, Fluka simulations have
1385 conducted in order to understand the background at HL-LHC conditions. The comparison to the
1386 data has shown, in Figure 4.4, a discrepancy of a factor 2 even though the order of magnitude is
1387 consistent. [Understand mismatch.]

1388



(a)



(b)

Figure 4.3: (4.3a) Extrapolation from 2016 data of single hit rate per unit area in the barrel region. (4.3b) Extrapolation from 2016 data of single hit rate per unit area in the endcap region.

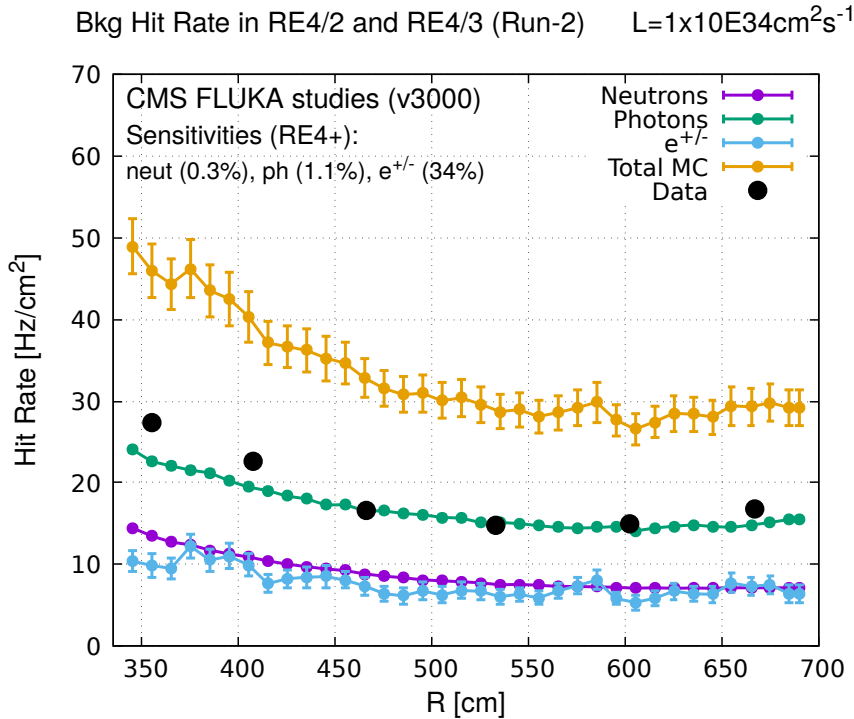


Figure 4.4: Background Fluka simulation compared to 2016 Data at $L = 10^{34} \text{ cm}^{-2} \cdot \text{s}^{-1}$ in the fourth endcap disk region. A mismatch in between simulation and data can be observed. [\[To be understood.\]](#)

1389 In the past, extensive long-term tests were carried out at several gamma and neutron facilities
 1390 certifying the detector performance. Both full size and small prototype RPCs have been irradiated
 1391 with photons up to an integrated charge of $\sim 0.05 \text{ C}/\text{cm}^2$ and $\sim 0.4 \text{ C}/\text{cm}^2$, respectively [53, 54].
 1392 During Run-I, the RPC system provided stable operation and excellent performance and did not
 1393 show any aging effects for integrated charge of the order of $0.01 \text{ C}/\text{cm}^2$. Projections on currents
 1394 from 2016 Data, has allowed to determine that the total integrated charge, by the end of HL-LHC,
 1395 would be of the order of $1 \text{ C}/\text{cm}^2$ (including a safety factor 3). [\[Corresponding figure needed.\]](#)
 1396

1397 4.2.1 The Gamma Irradiation Facilities

1398 4.2.1.1 GIF

1399 Located in the SPS West Area at the downstream end of the X5 test beam, the Gamma Irradiation
 1400 Facility (GIF) was a test area in which particle detectors were exposed to a particle beam in presence
 1401 of an adjustable gamma background [55]. Its goal was to reproduce background conditions these
 1402 detectors would suffer in their operating environment at LHC. GIF layout is shown in Figure 4.5.
 1403 Gamma photons are produced by a strong ^{137}Cs source installed in the upstream part of the zone
 1404 inside a lead container. The source container includes a collimator, designed to irradiate a $6 \times 6 \text{ m}^2$
 1405 area at 5 m maximum to the source. A thin lens-shaped lead filter helps providing with a uniform
 1406 outcoming flux in a vertical plane, orthogonal to the beam direction. The principal collimator hole
 1407 provides a pyramidal aperture of $74^\circ \times 74^\circ$ solid angle and provides a photon flux in a pyramidal vol-

ume along the beam axis. The photon rate is controled by further lead filters allowing the maximum rate to be limited and to vary within a range of four orders of magnitude. Particle detectors under test are then placed within the pyramidal volume in front of the source, perpendicularly to the beam line in order to profit from the homogeneous photon flux. Adjusting the background flux of photons can then be done by using the filters and choosing the position of the detectors with respect to the source.

1413

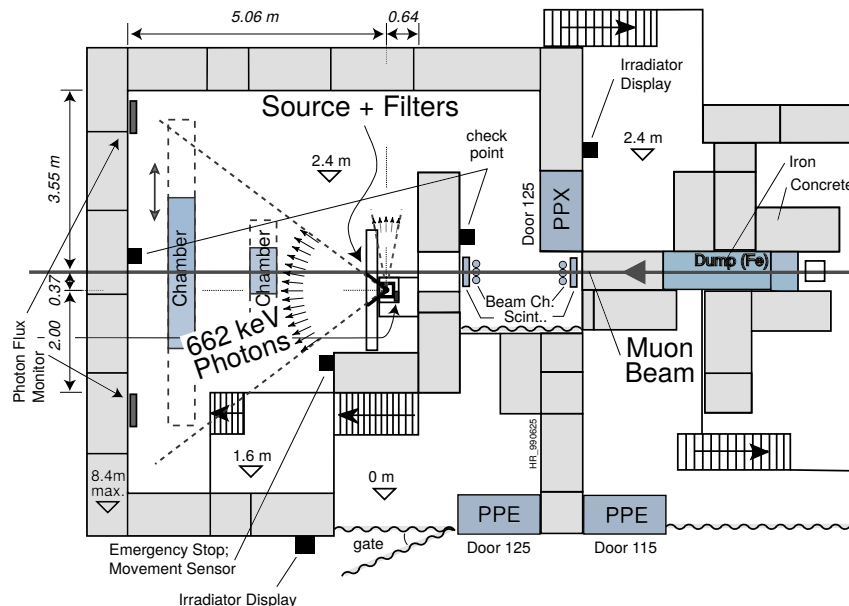


Figure 4.5: Layout of the test beam zone called X5c GIF at CERN. Photons from the radioactive source produce a sustained high rate of random hits over the whole area. The zone is surrounded by 8 m high and 80 cm thick concrete walls. Access is possible through three entry points. Two access doors for personnel and one large gate for material. A crane allows installation of heavy equipment in the area.

As described on Figure 4.6, the ^{137}Cs source emits a 662 keV photon in 85% of the decays. An activity of 740 GBq was measured on the 5th March 1997. To estimate the strength of the flux in 2014, it is necessary to consider the nuclear decay through time assiciated to the Cesium source whose half-life is well known ($t_{1/2} = (30.05 \pm 0.08)\text{y}$). The GIF tests where done in between the 20th and the 31st of August 2014, i.e. at a time $t = (17.47 \pm 0.02)\text{y}$ resulting in an attenuation of the activity from 740 GBq in 1997 to 494 GBq in 2014.

1420

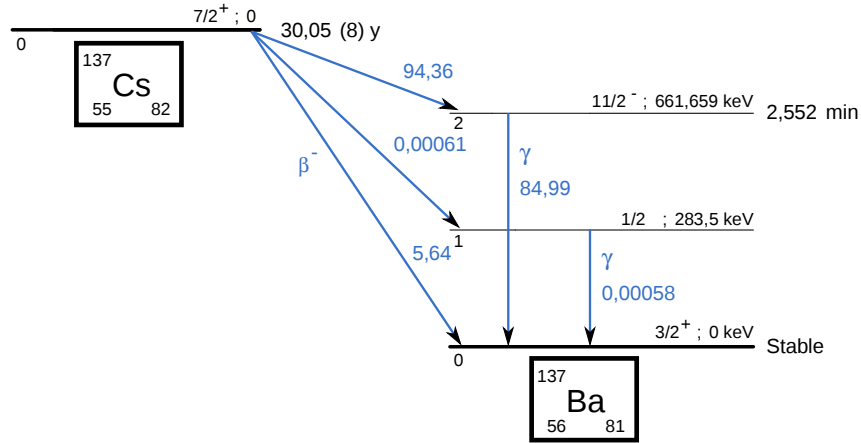


Figure 4.6: ^{137}Cs decays by β^- emission to the ground state of ^{137}Ba ($BR = 5.64\%$) and via the 662 keV isomeric level of ^{137}Ba ($BR = 94.36\%$) whose half-life is 2.55 min.

4.2.1.2 GIF++

The new Gamma Irradiation Facility (GIF++), located in the SPS North Area at the downstream end of the H4 test beam, has replaced its predecessor during LS1 and has been operational since spring 2015 [56]. Like GIF, GIF++ features a ^{137}Cs source of 662 keV gamma photons, their fluence being controlled with a set of filters of various attenuation factors. The source provides two separated large irradiation areas for testing several full-size muon detectors with continuous homogeneous irradiation, as presented in Figure 4.7.

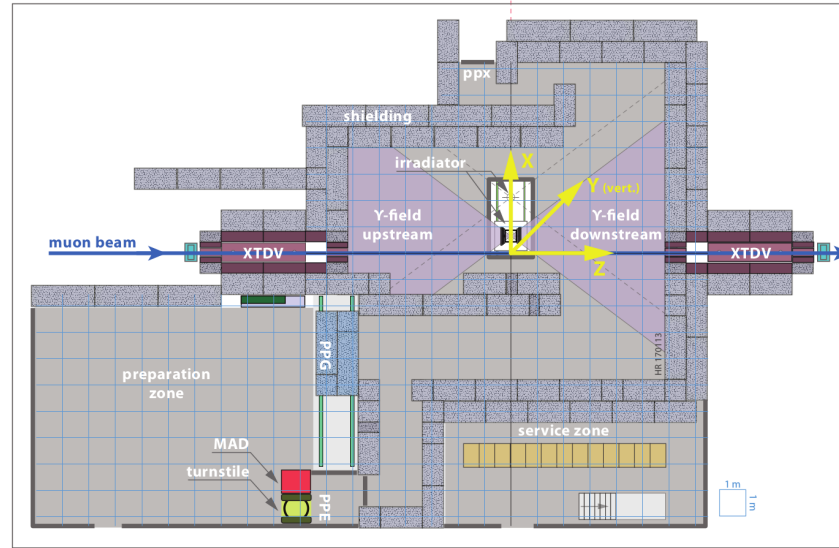


Figure 4.7: Floor plan of the GIF++ facility. When the facility downstream of the GIF++ takes electron beam, a beam pipe is installed along the beam line (z -axis). The irradiator can be displaced laterally (its center moves from $x = 0.65$ m to 2.15 m), to increase the distance to the beam pipe.

1429 The source activity was measured to be about 13.5 TBq in March 2016. The photon flux being
 1430 far greater than HL-LHC expectations, GIF++ provides an excellent facility for accelerated aging
 1431 tests of muon detectors.

1432

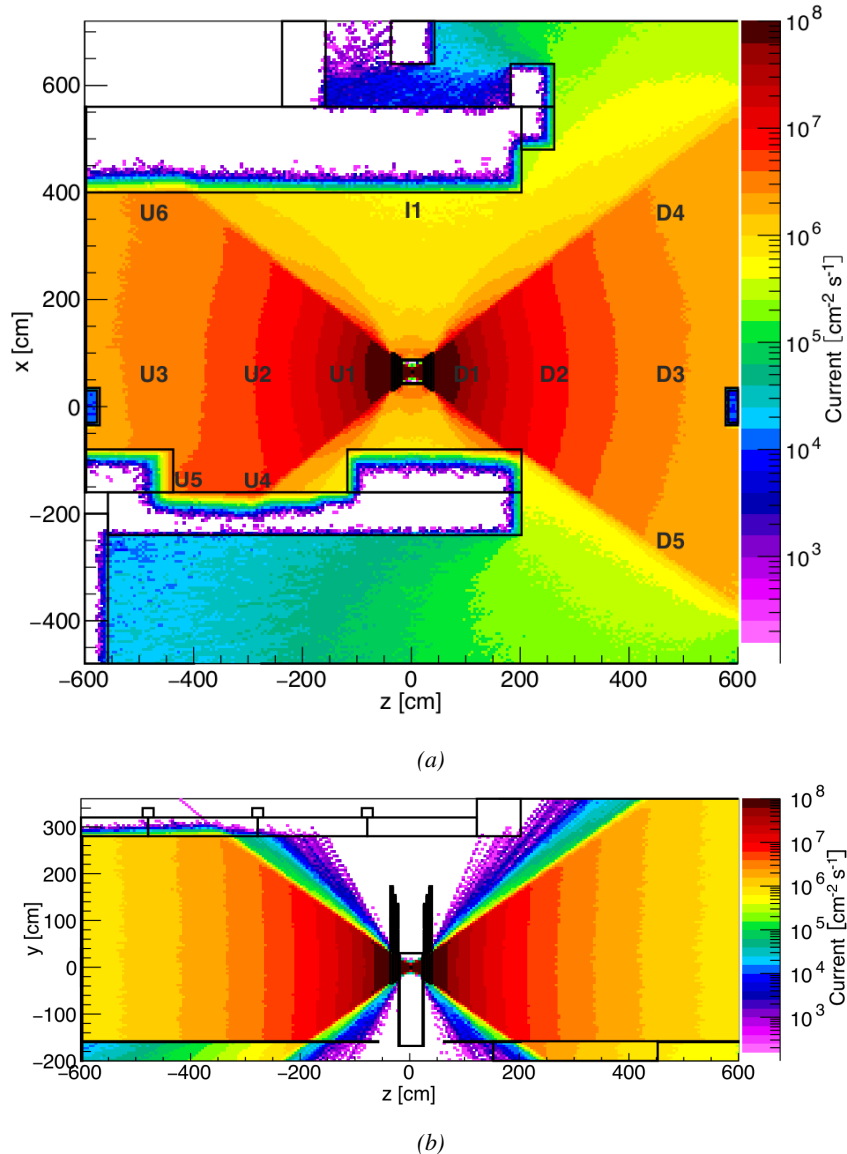


Figure 4.8: Simulated unattenuated current of photons in the xz plane (Figure 4.8a) and yz plane (Figure 4.8b) through the source at $x = 0.65 \text{ m}$ and $y = 0 \text{ m}$. With angular correction filters, the current of 662 keV photons is made uniform in xy planes.

1433 The source is situated in the muon beam line with the muon beam being available a few times a
 1434 year. The H4 beam, composed of muons with a momentum of about 150 GeV/c, passes through the
 1435 GIF++ zone and is used to study the performance of the detectors. Its flux is of 104 particles/ s cm^2

1436 focused in an area similar to $10 \times 10 \text{ cm}^2$. Therefore, with properly adjusted filters, one can imitate
 1437 the HL-LHC background and study the performance of muon detectors with their trigger/readout
 1438 electronics in HL-LHC environment.

1439

1440 4.3 Preliminary tests at GIF

1441 4.3.1 Resistive Plate Chamber test setup

1442 During summer 2014, preliminary tests have been conducted in the GIF area on a newly produced
 1443 RE4/2 chamber labelled RE-4-2-BARC-161. This chamber has been placed into a trolley covered
 1444 with a tent. The position of the RPC inside the tent and of the tent related to the source is described
 1445 in Figure 4.9. To test this CMS RPC, three different absorber settings were used. First of all,
 1446 measurements were done with fully opened source. Then, to complete this preliminary study, the
 1447 gamma flux has been attenuated from a factor 2 and a factor 5. The expected gamma flux at the level
 1448 of our detector will be discussed in subsection ??.

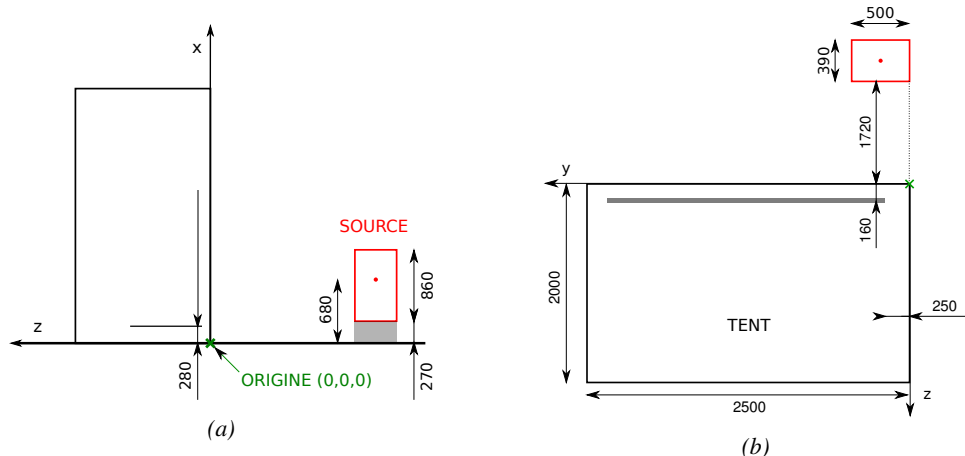


Figure 4.9: Description of the RPC setup. Dimensions are given in mm. A tent containing RPCs is placed at 1720 mm from the source container. The source is situated in the center of the container. RE-4-2-BARC-161 chamber is 160 mm inside the tent. This way, the distance between the source and the chambers plan is 2060 mm. Figure 4.9a provides a side view of the setup in the xz plane while Figure 4.9b shows a top view in the yz plane.



Figure 4.10: RE-4-2-BARC-I61 chamber is inside the tent as described in Figure 4.9. In the top right, the two scintillators used as trigger can be seen. This trigger system has an inclination of 10° relative to horizontal and is placed above half-partition B2 of the RPCs. PMT electronics are shielded thanks to lead blocks placed in order to protect them without stopping photons from going through the scintillators and the chamber.

1449 At the time of the tests, the beam not being operational anymore, a trigger composed of 2 plastic
 1450 scintillators has been placed in front of the setup with an inclination of 10 deg with respect to the
 1451 detector plane in order to look at cosmic muons. Using this particular trigger layout, shown on Fig-
 1452 ure 4.10, leads to a cosmic muon hit distribution into the chamber similar to the one in Figure 4.11.
 1453 Measured without gamma irradiation, two peaks can be seen on the profil of partition B, centered
 1454 on strips 52 and 59. Section ?? will help us understand that these two peaks are due respectively to
 1455 forward and backward coming cosmic particles where forward coming particles are first detected by
 1456 the scintillators and then the RPC while the backward coming muons are first detected in the RPC.

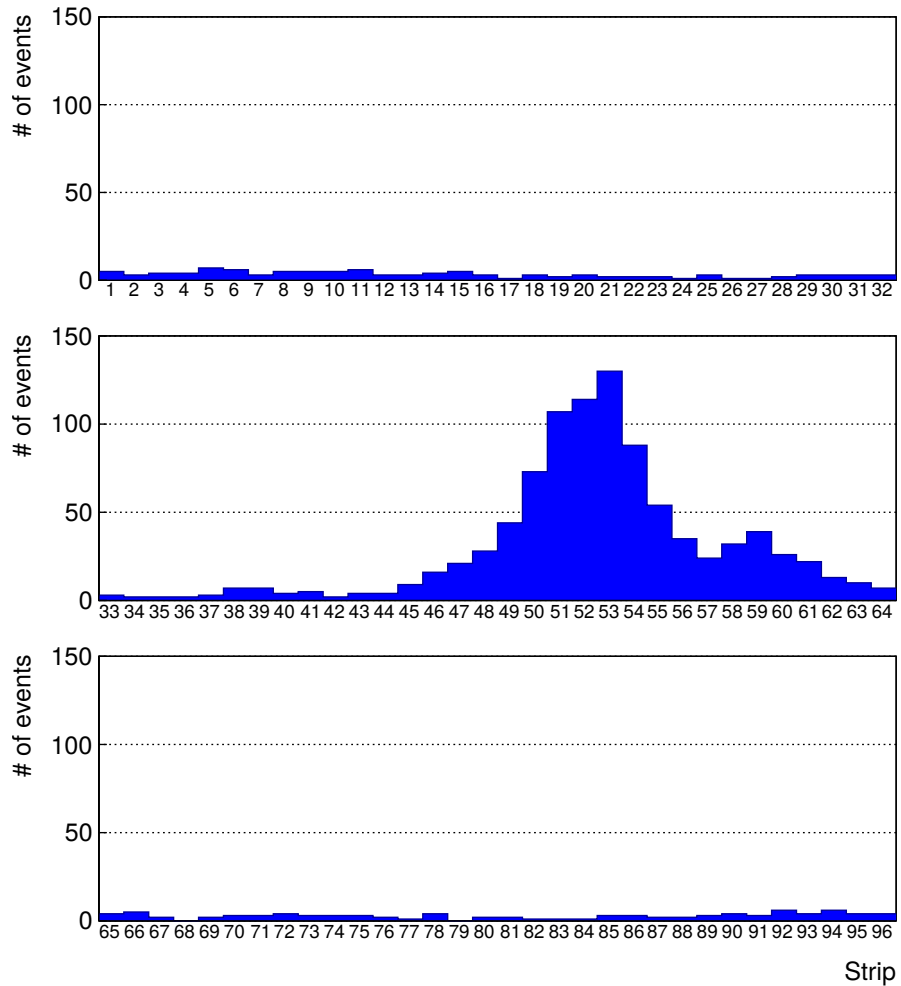


Figure 4.11: Hit distributions over all 3 partitions of RE-4-2-BARC-161 chamber is showed on these plots. Top, middle and bottom figures respectively correspond to partitions A, B, and C. These plots show that some events still occur in other half-partitions than B2, which corresponds to strips 49 to 64, in front of which the trigger is placed, contributing to the inefficiency of detection of cosmic muons. In the case of partitions A and C, the very low amount of data can be interpreted as noise. On the other hand, it is clear that a little portion of muons reach the half-partition B1, corresponding to strips 33 to 48.

4.3.2 Data Acquisition

4.3.3 Geometrical acceptance of the setup layout to cosmic muons

In order to profit from a constant gamma irradiation, the detectors inside of the GIF bunker need to be placed in a plane orthogonal to the beam line. The muon beam that used to be available was meant to test the performance of detectors under test. This beam not being active anymore, another solution to test detector performance had to be used. Thus, it has been decided to use cosmic muons detected through a telescope composed of two scintillators. Lead blocks were used as shielding to

protect the photomultipliers from gammas as can be seen from Figure 4.10.

An inclination has been given to the cosmic telescope to maximize the muon flux. A good compromise had to be found between good enough muon flux and narrow enough hit distribution to be sure to contain all the events into only one half partitions as required from the limited available readout hardware. Nevertheless, a consequence of the misplaced trigger, that can be seen as a loss of events in half-partition B1 in Figure 4.11, is an inefficiency. Nevertheless, the inefficiency of approximately 20 % highlighted in Figure 4.12 by comparing the performance of chamber BARC-161 in 904 and at GIF without irradiation seems too important to be explained only by the geometrical acceptance of the setup itself. Simulations have been conducted to show how the setup brings inefficiency.

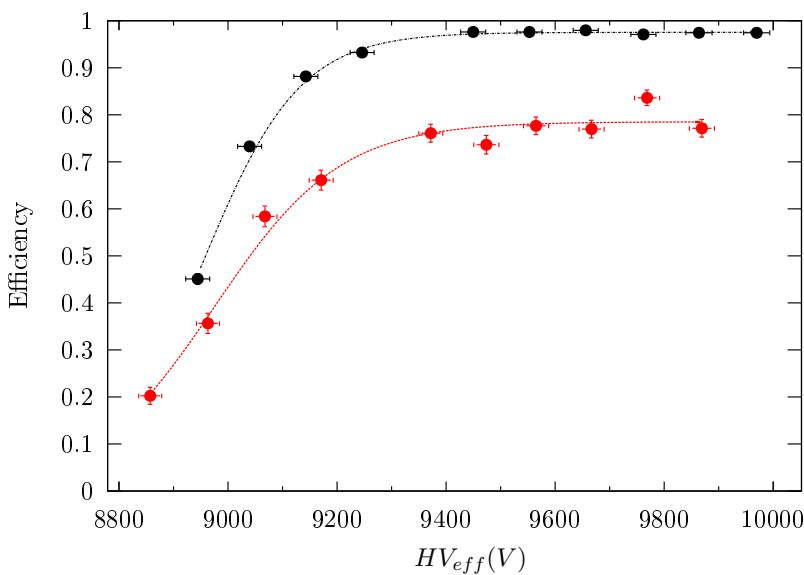


Figure 4.12: Results are derived from data taken on half-partition B2 only. On the 18th of June 2014, data has been taken on chamber RE-2-BARC-161 at building 904 (Prevessin Site) with cosmic muons providing us a reference efficiency plateau of $(97.54 \pm 0.15)\%$ represented by a black curve. A similar measurement has been done at GIF on the 21st of July with the same chamber giving a plateau of $(78.52 \pm 0.94)\%$ represented by a red curve.

4.3.3.1 Description of the simulation layout

The layout of GIF setup has been reproduced and incorporated into a Monte Carlo (MC) simulation to study the influence of the disposition of the telescope on the final distribution measured by the RPC. A 3D view of the simulated layout is given into Figure 4.13. Muons are generated randomly in a horizontal plane located at a height corresponding to the lowest point of the PMTs. This way, the needed size of the plane in order to simulate events happening at very big azimuthal angles (i.e. $\theta \approx \pi$) can be kept relatively small. The muon flux is designed to follow the usual $\cos^2\theta$ distribution for cosmic particle. The goal of the simulation is to look at muons that pass through the muon telescope composed of the two scintillators and define their distribution onto the RPC plane. During the reconstruction, the RPC plane is then divided into its strips and each muon track is assigned to a strip.

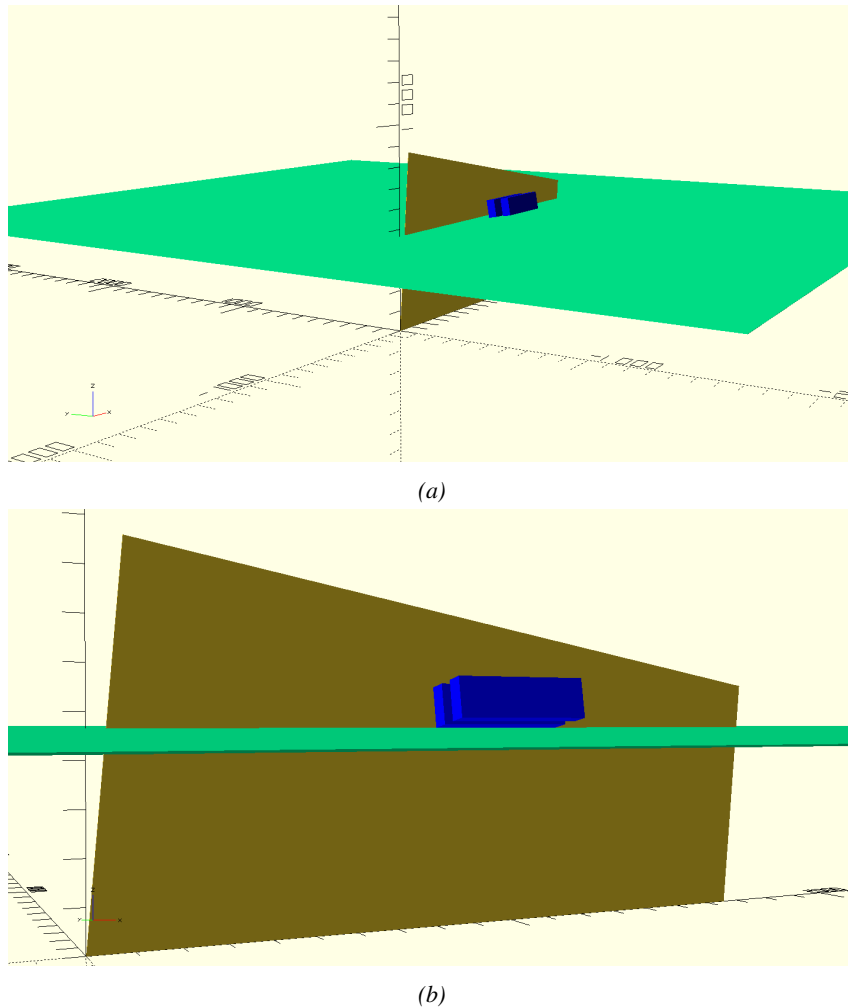


Figure 4.13: Representation of the layout used for the simulations of the test setup. The RPC is represented as a yellow trapezoid while the two scintillators as blue cuboids looking at the sky. A green plane corresponds to the muon generation plane within the simulation. Figure 4.9a shows a global view of the simulated setup. Figure 4.9b shows a zoomed view that allows to see the 2 scintillators as well as the full RPC plane.

1485 In order to further refine the quality of the simulation and understand deeper the results the
 1486 dependance of the distribution has been studied for a range of telescope inclinations. Moreover,
 1487 the threshold applied on the PMT signals has been included into the simulation in the form of a
 1488 cut. In the approximation of uniform scintillators, it has been considered that the threshold can be
 1489 understood as the minimum distance particles need to travel through the scintillating material to give
 1490 a strong enough signal. Particles that travel a distance smaller than the set "threshold" are thus not
 1491 detected by the telescope and cannot trigger the data taking. Finally, the FEE threshold also has
 1492 been considered in a similar way. The mean momentum of horizontal cosmic rays is higher than
 1493 those of vertical ones but the stopping power of matter for momenta ranging from 1 GeV to 1 TeV
 1494 stays comparable. It is then possible to assume that the mean number of primary e^-/ion pairs per
 1495 unit length will stay similar and thus, depending on the applied discriminator threshold, muons with

1496 the shortest path through the gas volume will deposit less charge and induce a smaller signal on the
 1497 pick-up strips that could eventually not be detected. These two thresholds also restrain the overall
 1498 geometrical acceptance of the system.

1499 **4.3.3.2 Simulation procedure**

1500 The simulation software has been designed using C++ and the output data is saved into ROOT
 1501 histograms. Simulations start for a threshold T_{scint} varying in a range from 0 to 45 mm in steps
 1502 of 5 mm, where $T_{scint} = 0$ mm corresponds to the case where there isn't any threshold apply on
 1503 the input signal while $T_{scint} = 45$ mm, which is the scintillator thickness, is the case where muons
 1504 cannot arrive orthogonally onto the scintillator surface. For a given T_{scint} , a set of RPC thresholds
 1505 are considered. The RPC threshold, T_{RPC} varies from 2 mm, the thickness of the gas volume, to
 1506 3 mm in steps of 0.25 mm. For each $(T_{scint}; T_{RPC})$ pair, $N_\mu = 10^8$ muons are randomly generated
 1507 inside the muon plane described in the previous paragraph with an azimuthal angle θ chosen to follow
 1508 a $\cos^2\theta$ distribution.

1509 Planes are associated to each surface of the scintillators. Knowing muon position into the muon
 1510 plane and its direction allows us, by assuming that muons travel in a straight line, to compute the
 1511 intersection of the muon track with these planes. Applying conditions to the limits of the surfaces
 1512 of the scintillator faces then gives us an answer to whether or not the muon passed through the
 1513 scintillators. In the case the muon has indeed passed through the telescope, the path through each
 1514 scintillator is computed and muons whose path was shorter than T_{scint} are rejected and are thus
 1515 considered as having not interacted with the setup.

1516 On the contrary, if the muon is labeled as good, its position within the RPC plane is computed
 1517 and the corresponding strip, determined by geometrical tests in the case the distance through the
 1518 gas volume was enough not to be rejected because of T_{RPC} , gets a hit and several histograms
 1519 are filled in order to keep track of the generation point on the muon plane, the intersection points
 1520 of the reconstructed muons within the telescope, or on the RPC plane, the path traveled through
 1521 each individual scintillator or the gas volume, as well as other histograms. Moreover, muons fill
 1522 different histograms whether they are forward or backward coming muons. They are discriminated
 1523 according to their direction components. When a muon is generated, an (x, y, z) position is assigned
 1524 into the muon plane as well as a $(\theta; \phi)$ pair that gives us the direction it's coming from. This way,
 1525 muons satisfying the condition $0 \leq \phi < \pi$ are designated as backward coming muons while muons
 1526 satisfying $\pi \leq \phi < 2\pi$ as forward coming muons.

1527 This simulation is then repeated for different telescope inclinations ranging in between 4 and 20°
 1528 and varying in steps of 2°. Due to this inclination and to the vertical position of the detector under
 1529 test, the muon distribution reconstructed in the detector plane is asymmetrical. The choice as been
 1530 made to chose a skew distribution formula to fit the data built as the multiplication of gaussian and
 1531 sigmoidal curves together. A typical gaussian formula is given as 4.1 and has three free parameters
 1532 as A_g , its amplitude, \bar{x} , its mean value and σ , its root mean square. Sigmoidal curves as given by
 1533 formula 4.2 are functions converging to 0 and A_s as x diverges. The inflection point is given as x_i
 1534 and λ is proportional to the slope at $x = x_i$. In the limit where $\lambda \rightarrow \infty$, the sigmoid becomes a
 1535 step function.

$$g(x) = A_g e^{-\frac{(x-\bar{x})^2}{2\sigma^2}} \quad (4.1)$$

$$s(x) = \frac{A_s}{1 + e^{-\lambda(x-x_i)}} \quad (4.2)$$

Finally, a possible representation of a skew distribution is given by formula 4.3 and is the product of 4.1 and 4.2. Naturally, here $A_{sk} = A_g \times A_s$ and represents the theoretical maximum in the limit where the skew tends to a gaussian function.

$$sk(x) = g(x) \times s(x) = A_{sk} \frac{e^{\frac{-(x-\bar{x})^2}{2\sigma^2}}}{1 + e^{-\lambda(x-x_i)}} \quad (4.3)$$

4.3.3.3 Results

Influence of T_{scint} on the muon distribution

Influence of T_{RPC} on the muon distribution

Influence of the telescope inclination on the muon distribution

Comparison to data taken at GIF without irradiation

4.3.4 Photon flux at GIF

4.3.4.1 Expectations from simulations

In order to understand and evaluate the γ flux in the GIF area, simulations had been conducted in 1999 and published by S. Agosteo et al [55]. Table 4.1 presented in this article gives us the γ flux for different distances D to the source. This simulation was done using GEANT and a Monte Carlo N-Particle (MCNP) transport code, and the flux F is given in number of γ per unit area and unit time along with the estimated error from these packages expressed in %.

Nominal ABS	Photon flux F [$s^{-1}cm^{-2}$]			
	at $D = 50$ cm	at $D = 155$ cm	at $D = 300$ cm	at $D = 400$ cm
1	$0.12 \cdot 10^8 \pm 0.2\%$	$0.14 \cdot 10^7 \pm 0.5\%$	$0.45 \cdot 10^6 \pm 0.5\%$	$0.28 \cdot 10^6 \pm 0.5\%$
2	$0.68 \cdot 10^7 \pm 0.3\%$	$0.80 \cdot 10^6 \pm 0.8\%$	$0.25 \cdot 10^6 \pm 0.8\%$	$0.16 \cdot 10^6 \pm 0.6\%$
5	$0.31 \cdot 10^7 \pm 0.4\%$	$0.36 \cdot 10^6 \pm 1.2\%$	$0.11 \cdot 10^6 \pm 1.2\%$	$0.70 \cdot 10^5 \pm 0.9\%$

Table 4.1: Total photon flux ($E\gamma \leq 662$ keV) with statistical error predicted considering a ^{137}Cs activity of 740 GBq at different values of the distance D to the source along the x -axis of irradiation field [55].

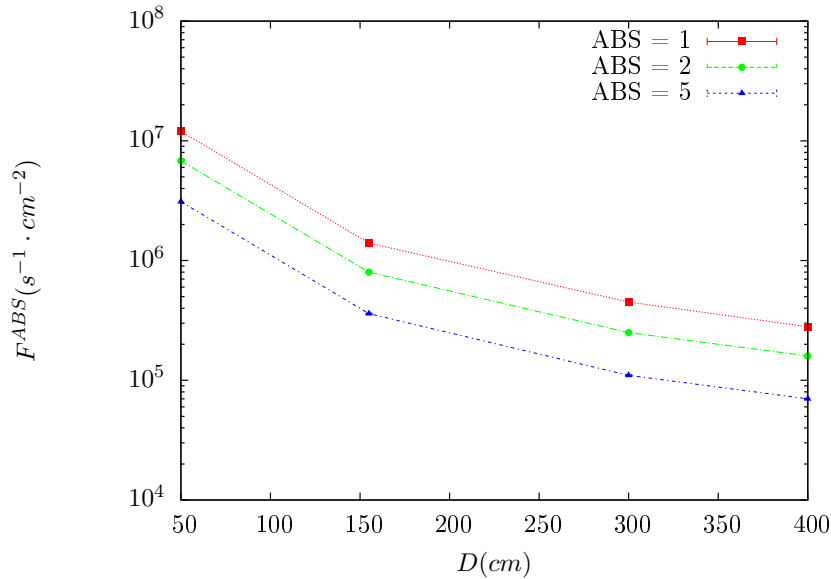


Figure 4.14: γ flux $F(D)$ is plot using values from table 4.1. As expected, the plot shows similar attenuation behaviours with increasing distance for each absorption factors.

The simulation doesn't directly provides us with an estimated flux at the level of our RPC. First of all, it is needed to extract the value of the flux from the available data contained in the original paper and then to estimate the flux in 2014 at the time the experimentation took place. Figure 4.14 that contains the data from Table 4.1. In the case of a pointlike source emitting isotropic and homogeneous gamma radiations, the gamma flux F at a distance D to the source with respect to a reference point situated at D_0 where a known flux F_0 is measured will be expressed like in Equation 4.4, assuming that the flux decreases as $1/D^2$, where c is a fitting factor.

$$F^{ABS} = F_0^{ABS} \times \left(\frac{cD_0}{D} \right)^2 \quad (4.4)$$

By rewriting Equation 4.4, it comes that :

$$c = \frac{D}{D_0} \sqrt{\frac{F^{ABS}}{F_0^{ABS}}} \quad (4.5)$$

$$\Delta c = \frac{c}{2} \left(\frac{\Delta F^{ABS}}{F^{ABS}} + \frac{\Delta F_0^{ABS}}{F_0^{ABS}} \right) \quad (4.6)$$

Finally, using Equation 4.5 and the data in Table 4.1 with $D_0 = 50$ cm as reference point, we can build Table 4.2. It is interesting to note that c for each value of D doesn't depend on the absorption factor.

Nominal ABS	Correction factor c		
	at $D = 155$ cm	at $D = 300$ cm	at $D = 400$ cm
1	$1.059 \pm 0.70\%$	$1.162 \pm 0.70\%$	$1.222 \pm 0.70\%$
2	$1.063 \pm 1.10\%$	$1.150 \pm 1.10\%$	$1.227 \pm 0.90\%$
5	$1.056 \pm 1.60\%$	$1.130 \pm 1.60\%$	$1.202 \pm 1.30\%$

Table 4.2: Correction factor c is computed thanks to formulae 4.5 taking as reference $D_0 = 50$ cm and the associated flux F_0^{ABS} for each absorption factor available in table 4.1.

1562 For the range of D/D_0 values available, it is possible to use a simple linear fit to get the evolution
 1563 of c . The linear fit will then use only 2 free parameters, a and b , as written in Equation 4.7. This gives
 1564 us the results showed in Figure 4.15. Figure 4.15b confirms that using only a linear fit to extract c is
 1565 enough as the evolution of the rate that can be obtained superimposes well on the simulation points.

$$c \left(\frac{D}{D_0} \right) = a \frac{D}{D_0} + b \quad (4.7)$$

$$F^{ABS} = F_0^{ABS} \left(a + \frac{bD_0}{D} \right)^2 \quad (4.8)$$

$$\Delta F^{ABS} = F^{ABS} \left[\frac{\Delta F_0^{ABS}}{F_0^{ABS}} + 2 \frac{\Delta a + \Delta b \frac{D_0}{D}}{a + \frac{bD_0}{D}} \right] \quad (4.9)$$

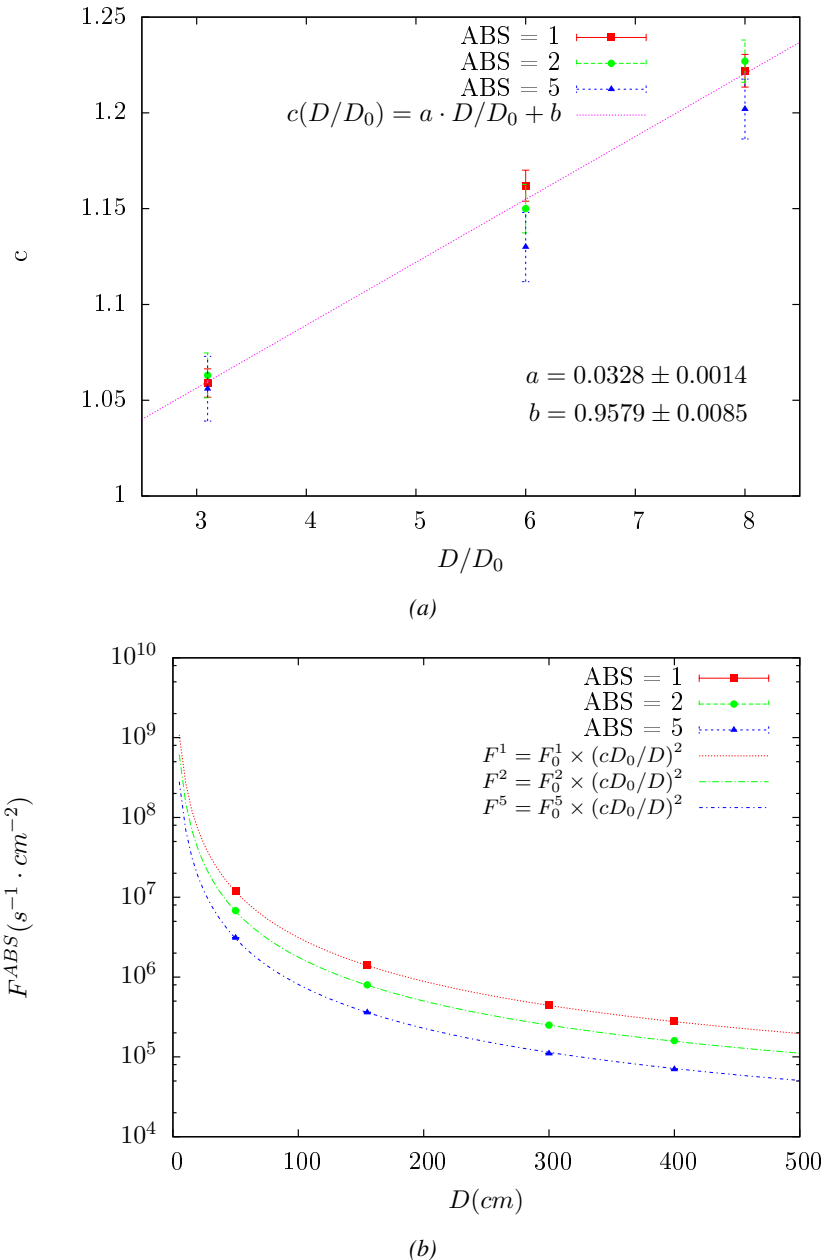


Figure 4.15: Figure 4.15a shows the linear approximation fit done via formulae 4.7 on data from table 4.2. Figure 4.15b shows a comparison of this model with the simulated flux using a and b given in figure 4.15a in formulae 4.4 and the reference value $D_0 = 50\text{cm}$ and the associated flux for each absorption factor F_0^{ABS} from table 4.1

In the case of the 2014 GIF tests, the RPC plane is located at a distance $D = 206\text{ cm}$ to the source. Moreover, to estimate the strength of the flux in 2014, it is necessary to consider the nuclear decay through time associated to the Cesium source whose half-life is well known ($t_{1/2} = (30.05 \pm 0.08)\text{ y}$). The very first source activity measurement has been done on the 5th of March 1997 while the GIF

1570 tests where done in between the 20th and the 31st of August 2014, i.e. at a time $t = (17.47 \pm 0.02)$ y
 1571 resulting in an attenuation of the activity from 740 GBq in 1997 to 494 GBq in 2014. All the needed
 1572 information to extrapolate the flux through our detector in 2014 has now been assembled, leading
 1573 to the Table 4.3. It is interesting to note that for a common RPC sensitivity to γ of $2 \cdot 10^{-3}$, the
 1574 order of magnitude of the estimated hit rate per unit area is of the order of the kHz for the fully
 1575 opened source. Moreover, taking profit of the two working absorbers, it will be possible to scan
 1576 background rates at 0 Hz, ~ 300 Hz as well as ~ 600 Hz. Without source, a good estimate of the
 1577 intrinsic performance will be available. Then at 300 Hz, the goal will be to show that the detectors
 1578 fulfill the performance certification of CMS RPCs. Then a first idea of the performance of the
 1579 detectors at higher background will be provided with absorption factors 2 (~ 600 Hz) and 1 (no
 1580 absorption). *[Here I will also put a reference to the plot showing the estimated background rate at
 1581 the level of RE3/1 in the case of HL-LHC but this one being in another chapter, I will do it later.]*

Nominal ABS	Photon flux F [$s^{-1}cm^{-2}$]			Hit rate/unit area [$Hz cm^{-2}$] at $D^{2014} = 206$ cm
	at $D_0^{1997} = 50$ cm	at $D^{1997} = 206$ cm	at $D^{2014} = 206$ cm	
1	$0.12 \cdot 10^8 \pm 0.2\%$	$0.84 \cdot 10^6 \pm 0.3\%$	$0.56 \cdot 10^6 \pm 0.3\%$	1129 ± 32
2	$0.68 \cdot 10^7 \pm 0.3\%$	$0.48 \cdot 10^6 \pm 0.3\%$	$0.32 \cdot 10^6 \pm 0.3\%$	640 ± 19
5	$0.31 \cdot 10^7 \pm 0.4\%$	$0.22 \cdot 10^6 \pm 0.3\%$	$0.15 \cdot 10^6 \pm 0.3\%$	292 ± 9

Table 4.3: The data at D_0 in 1997 is taken from [55]. In a second step, using Equations 4.8 and 4.9, the flux at D can be estimated in 1997. Then, taking into account the attenuation of the source activity, the flux at D can be estimated at the time of the tests in GIF in 2014. Finally, assuming a sensitivity of the RPC to γ $s = 2 \cdot 10^{-3}$, an estimation of the hit rate per unit area is obtained.

1582 **4.3.4.2 Dose measurements**

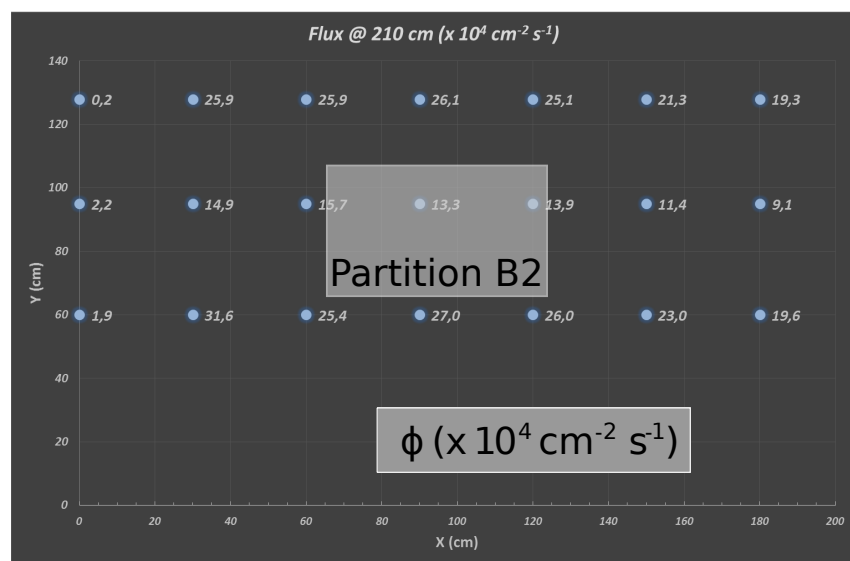


Figure 4.16: Dose measurements has been done in a plane corresponding to the tents front side. This plan is 1900 mm away from the source. As explained in the first chapter, a lens-shaped lead filter provides a uniform photon flux in the vertical plan orthogonal to the beam direction. If the second line of measured fluxes is not taken into account because of lower values due to experimental equipments in the way between the source and the tent, the uniformity of the flux is well showed by the results.

₁₅₈₃ **4.3.5 Results and discussions**

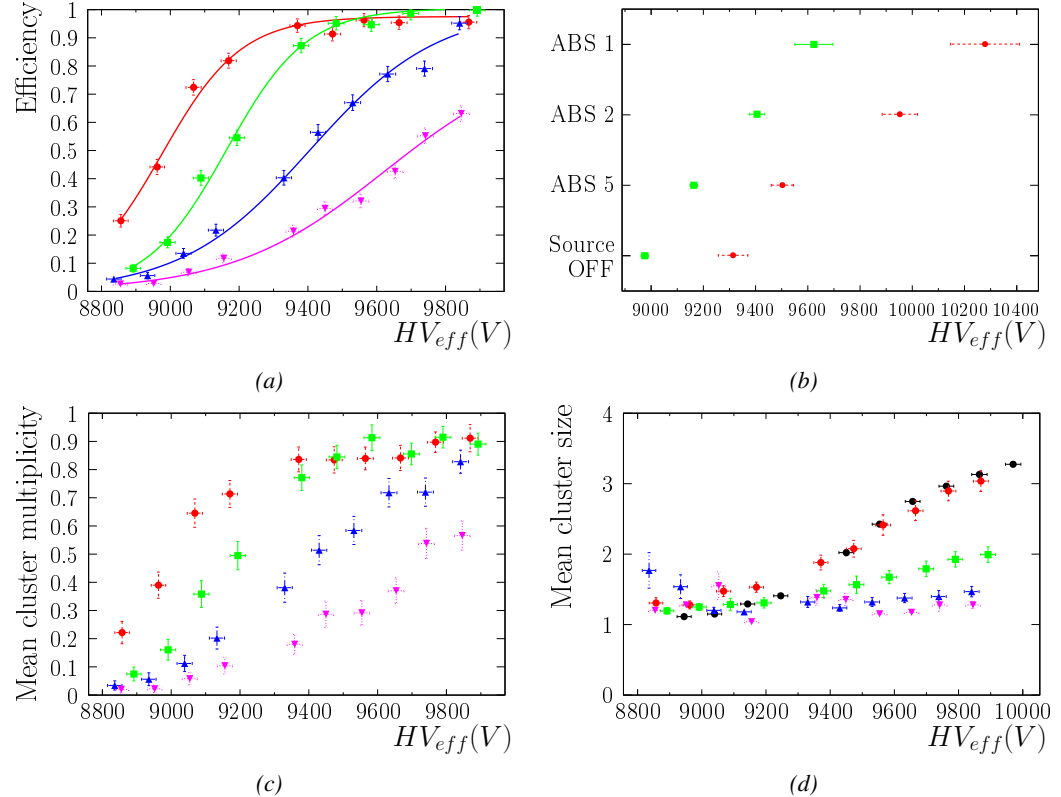


Figure 4.17

1584 4.4 Longevity tests at GIF++

1585 Longevity studies imply a monitoring of the performance of the detectors probed using a high inten-
1586 sity muon beam in a irradiated environment by periodically measuring their rate capability, the dark
1587 current running through them and the bulk resistivity of the Bakelite composing their electrodes.
1588 GIF++, with its very intense ^{137}Cs source, provides the perfect environment to perform such kind
1589 of tests. Assuming a maximum acceleration factor of 3, it is expected to accumulate the equivalent
1590 charge in 1.7 years.

1591 As the maximum background is found in the endcap, the choice naturally was made to focus the
1592 GIF++ longevity studies on endcap chambers. Most of the RPC system was installed in 2007. Nev-
1593 ertheless, the large chambers in the fourth endcap (RE4/2 and RE4/3) have been installed during
1594 LS1 in 2014. The Bakelite of these two different productions having different properties, four spare
1595 chambers of the present system were selected, two RE2,3/2 spares and two RE4/2 spares. Having
1596 two chambers of each type allows to always keep one of them non irradiated as reference, the per-
1597 formance evolution of the irradiated chamber being then compared through time to the performance
1598 of the non irradiated one.

1599 The performance of the detectors under different level of irradiation is measured periodically dur-
1600 ing dedicated test beam periods using the H4 muon beam. In between these test beam periods, the
1601 two RE2,3/2 and RE4/2 chambers selected for this study are irradiated by the ^{137}Cs source in order
1602 to accumulate charge and the gamma background is monitored, as well as the currents. The two
1603 remaining chambers are kept non-irradiated as reference detectors. Due to the limited gas flow in
1604 GIF++, the RE4 chamber remained non-irradiated until end of November 2016 where a new mass
1605 flow controller has been installed allowing for bigger volumes of gas to flow in the system.

1606 Figures 4.18 and 4.19 give us for different test beam periods, and thus for increasing integrated
1607 charge through time, a comparison of the maximum efficiency, obtained using a sigmoid-like func-
1608 tion, and of the working point of both irradiated and non irradiated chambers [**SIGMOID2005**]. No
1609 aging is yet to see from this data, the shifts in γ rate per unit area in between irradiated and non
1610 irradiated detectors and RE2 and RE4 types being easily explained by a difference of sensitivity due
1611 to the various Bakelite resistivities of the HPL electrodes used for the electrode production.

1612 Collecting performance data at each test beam period allows us to extrapolate the maximum effi-
1613 ciency for a background hit rate of $300\text{ Hz}/\text{cm}^2$ corresponding to the expected HL-LHC conditions.
1614 Aging effects could emerge from a loss of efficiency with increasing integrated charge over time,
1615 thus Figure 4.20 helps us understand such degradation of the performance of irradiated detectors in
1616 comparison with non irradiated ones. The final answer for an eventual loss of efficiency is given in
1617 Figure 4.21 by comparing for both irradiated and non irradiated detectors the efficiency sigmoids
1618 before and after the longevity study. Moreover, to complete the performance information, the Bake-
1619 lite resistivity is regularly measured thanks to Ag scans (Figure 4.22) and the noise rate is monitored
1620 weekly during irradiation periods (Figure 4.23). At the end of 2016, no signs of aging were observed
1621 and further investigation is needed to get closer to the final integrated charge requirements proposed
1622 for the longevity study of the present CMS RPC sub-system.

1623

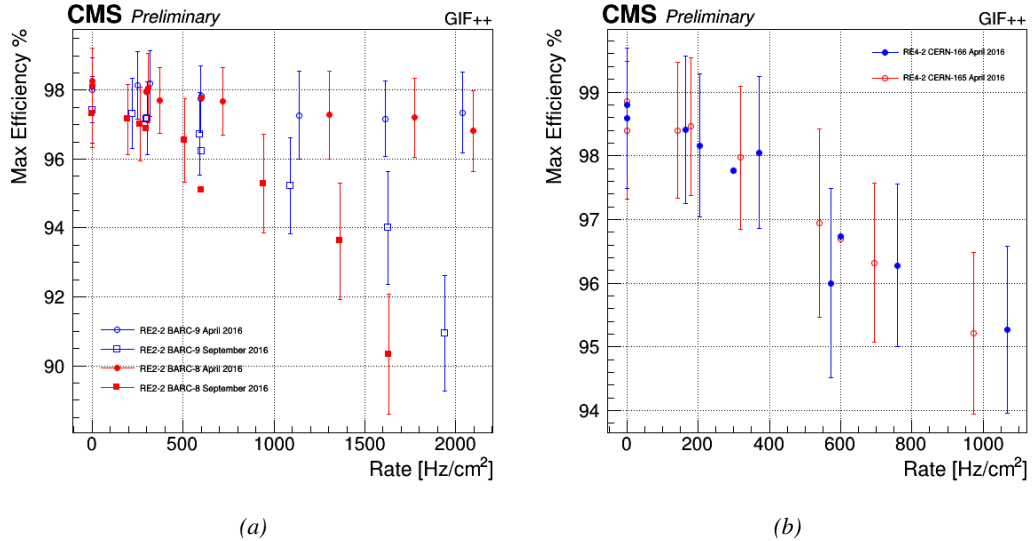


Figure 4.18: Evolution of the maximum efficiency for RE2 (4.18a) and RE4 (4.18b) chambers with increasing extrapolated γ rate per unit area at working point. Both irradiated (blue) and non irradiated (red) chambers are shown.

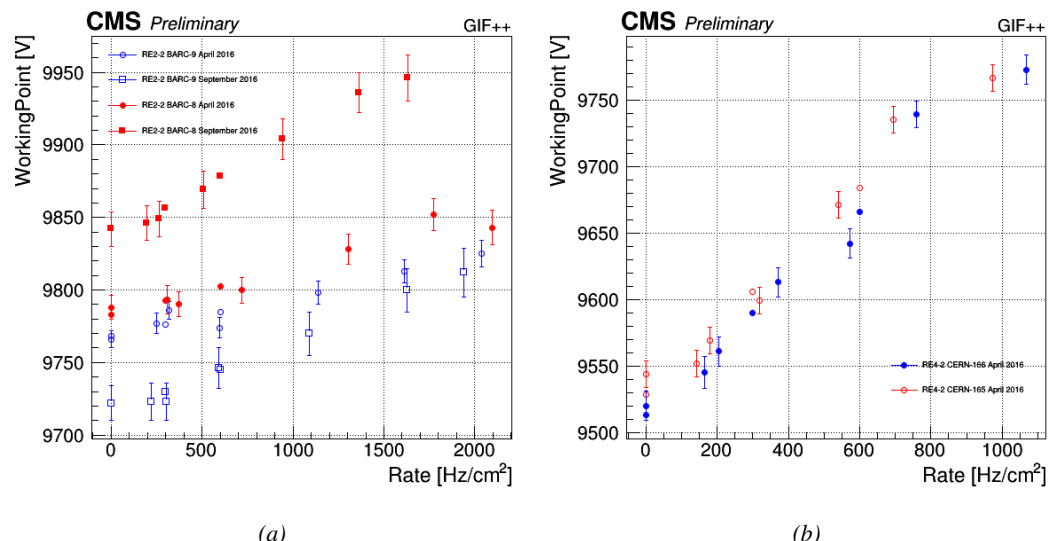


Figure 4.19: Evolution of the working point for RE2 (4.19a) and RE4 (4.19b) with increasing extrapolated γ rate per unit area at working point. Both irradiated (blue) and non irradiated (red) chambers are shown.

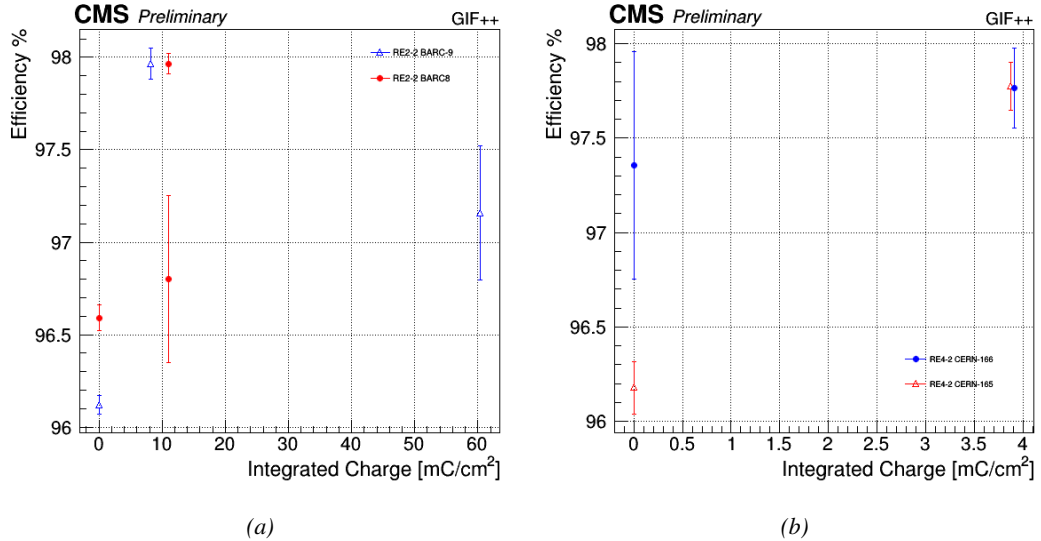


Figure 4.20: Evolution of the maximum efficiency at HL-LHC conditions, i.e. a background hit rate per unit area of 300 Hz/cm², with increasing integrated charge for RE2 (4.20a) and RE4 (4.20b) detectors. Both irradiated (blue) and non irradiated (red) chambers are shown. The integrated charge for non irradiated detectors is recorded during test beam periods and stays small with respect to the charge accumulated in irradiated chambers.

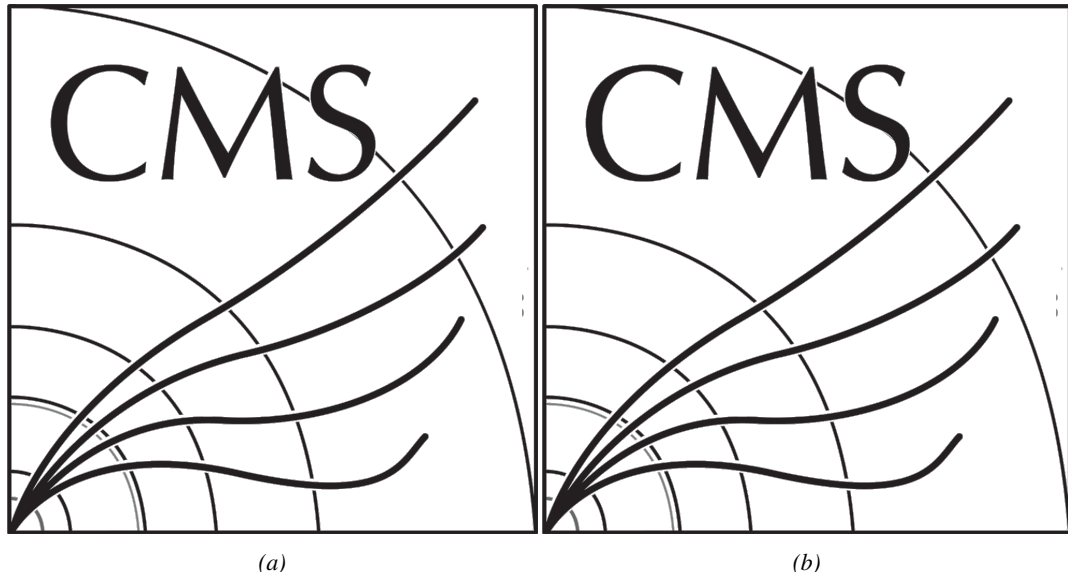


Figure 4.21: Comparison of the efficiency sigmoid before (triangles) and after (circles) irradiation for RE2 (4.21a) and RE4 (4.21b) detectors. Both irradiated (blue) and non irradiated (red) chambers are shown.

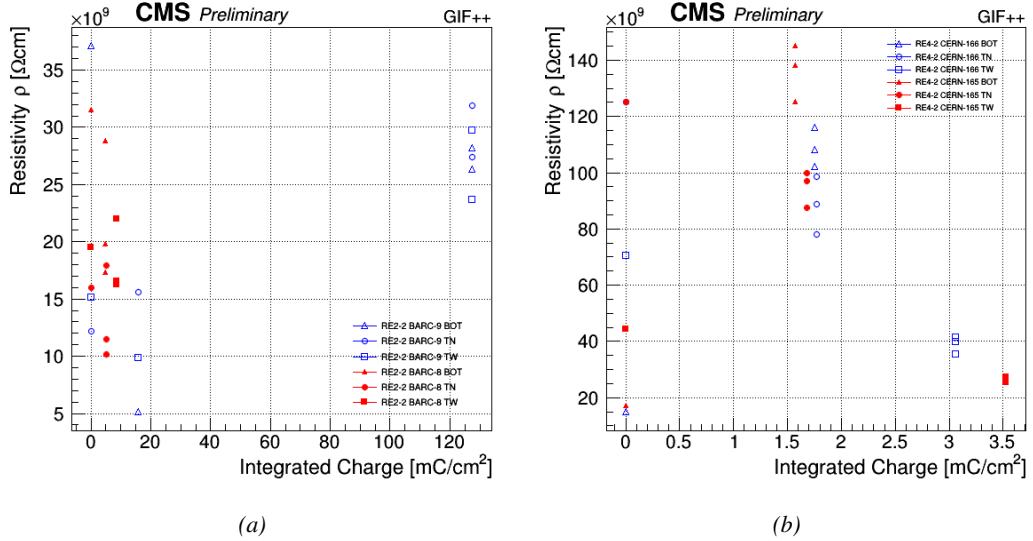


Figure 4.22: Evolution of the Bakelite resistivity for RE2 (4.22a) and RE4 (4.22b) detectors. Both irradiated (blue) and non-irradiated (red) chambers are shown.

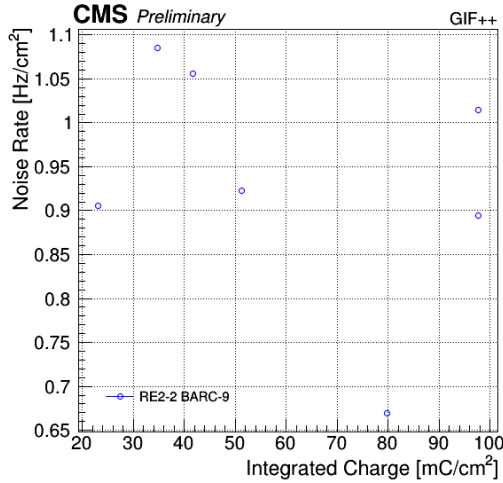


Figure 4.23: Evolution of the noise rate per unit area for the irradiated chamber RE2-2-BARC-9 only.

4.4.1 Description of the Data Acquisition

For the longevity studies, four spare chambers of the present system are used. Two spare RPCs of the RE2,3 stations as well as two spare RPCs from the new RE4 stations have been mounted in a Trolley. Six RE4 gaps are also placed in the trolley. The trolley is placed inside the GIFT++ in the upstream region of the bunker, taking the cesium source as a reference. The trolley is oriented for the detection surface of the chambers to be orthogonal to the beam line. The system can be moved along the orthogonal plane in order to have the beam in all η -partitions. For the aging the trolley is

1631 moved outside the beam line and is placed in a distance of 5.2 m to the source, which irradiates the
 1632 bunker using an attenuation filter of 2.2 which corresponds to a fluence of 10^7 gamma/cm^2 .

1633 During GIF++ operation, the data collected can be divided into different categories as several
 1634 parameters are monitored in addition to the usual RPC performance data. On one hand, to know
 1635 the performance of a chamber, it is need to measure its efficiency and to know the background
 1636 conditions in which it is operated. To do this, the hit signals from the chamber are recorded and
 1637 stored in a ROOT file via a Data Acquisition (DAQ) software. On the other hand, it is also very
 1638 important to monitor parameters such as environmental pressure and temperature, gas temperature
 1639 and humidity, RPC HV, LV, and currents, or even source and beam status. This is done through the
 1640 GIF++ web Detector Control Software (DCS) that stores this information in a database.

1641 Two different types of tests are conducted on RPCs via the DAQ. Indeed, the performance of the
 1642 detectors is measured periodically during dedicated test beam periods using the H4 muon beam. In
 1643 between these test beam periods, when the beam is not available, the chambers are irradiated by the
 1644 ^{137}Cs in order to accumulate deposited charge and the gamma background is measured.

1645 RPCs under test are connected through LVDS cables to V1190A Time-to-Digital Converter
 1646 (TDC) modules manufactured by CAEN. These modules, located in the rack area outside of the
 1647 bunker, get the logic signals sent by the chambers and save them into their buffers. Due to the
 1648 limited size of the buffers, the collected data is regularly erased and replaced. A trigger signal is
 1649 needed for the TDC modules to send the useful data to the DAQ computer via a V1718 CAEN USB
 1650 communication module.

1651 In the case of performance test, the trigger signal used for data acquisition is generated by the
 1652 coincidence of three scintillators. A first one is placed upstream outside of the bunker, a second one
 1653 is placed downstream outside of the bunker, while a third one is placed in front of the trolley, close by
 1654 the chambers. Every time a trigger is sent to the TDCs, i.e. every time a muon is detected, knowing
 1655 the time delay in between the trigger and the RPC signals, signals located in the right time window
 1656 are extracted from the buffers and saved for later analysis. Signals are taken in a time window of
 1657 400 ns centered on the muon peak (here we could show a time spectrum). On the other hand, in the
 1658 case of background rate measurement, the trigger signal needs to be "random" not to measure muons
 1659 but to look at gamma background. A trigger pulse is continuously generated at a rate of 300 Hz using
 1660 a dual timer. To integrate an as great as possible time, all signals contained within a time window of
 1661 10us prior to the random trigger signal are extracted form the buffers and saved for further analysis
 1662 (here another time spectrum to illustrate could be useful, maybe even place both spectrum together
 1663 as a single Figure).

1664 The signals sent to the TDCs correspond to hit collections in the RPCs. When a particle hits
 1665 a RPC, it induce a signal in the pickup strips of the RPC readout. If this signal is higher than the
 1666 detection threshold, a LVDS signal is sent to the TDCs. The data is then organised into 4 branches
 1667 keeping track of the event number, the hit multiplicity for the whole setup, and the time and channel
 1668 profile of the hits in the TDCs.

1669 **4.4.2 RPC current, environmental and operation parameter monitoring**

1670 In order to take into account the variation of pressure and temperature between different data taking
 1671 periods the applied voltage is corrected following the relationship :

$$1672 \quad HV_{eff} = HV_{app} \times \left(0.2 + 0.8 \cdot \frac{P_0}{P} \times \frac{T}{T_0} \right) \quad (4.10)$$

¹⁶⁷² where T_0 (=293 K) and P_0 (=990 mbar) are the reference values.

¹⁶⁷³ **4.4.3 Measurement procedure**

¹⁶⁷⁴ Insert a short description of the online tools (DAQ, DCS, DQM).

¹⁶⁷⁵ Insert a short description of the offline tools : tracking and efficiency algorithm.

¹⁶⁷⁶ Identify long term aging effects we are monitoring the rates per strip.

¹⁶⁷⁷ **4.4.4 Longevity studies results**

5

1678

1679

Investigation on high rate RPCs

1680 **5.1 Rate limitations and ageing of RPCs**

1681 **5.1.1 Low resistivity electrodes**

1682 **5.1.2 Low noise front-end electronics**

1683 **5.2 Construction of prototypes**

1684 **5.3 Results and discussions**

6

1685

1686

Conclusions and outlooks

¹⁶⁸⁷ **6.1 Conclusions**

¹⁶⁸⁸ **6.2 Outlooks**

A

1689

1690

A data acquisition software for CAEN VME TDCs

1691

1692 Certifying detectors in the perspective of HL-LHC required to develop tools for the GIF++ expe-
1693 riment. Among them was the C++ Data Acquisition (DAQ) software that allows to make the com-
1694 munications in between a computer and TDC modules in order to retrieve the RPC data [57]. In this
1695 appendix, details about this software, as of how the software was written, how it functions and how
1696 it can be exported to another similar setup, will be given.

1697 A.1 GIF++ DAQ file tree

1698 GIF++ DAQ source code is fully available on github at [https://github.com/afagot/GIF_](https://github.com/afagot/GIF_DAQ)
1699 DAQ. The software requires 3 non-optional dependencies:

- 1700 • CAEN USB Driver, to mount the VME hardware,
1701 • CAEN VME Library, to communicate with the VME hardware, and
1702 • ROOT, to organize the collected data into a TTree.

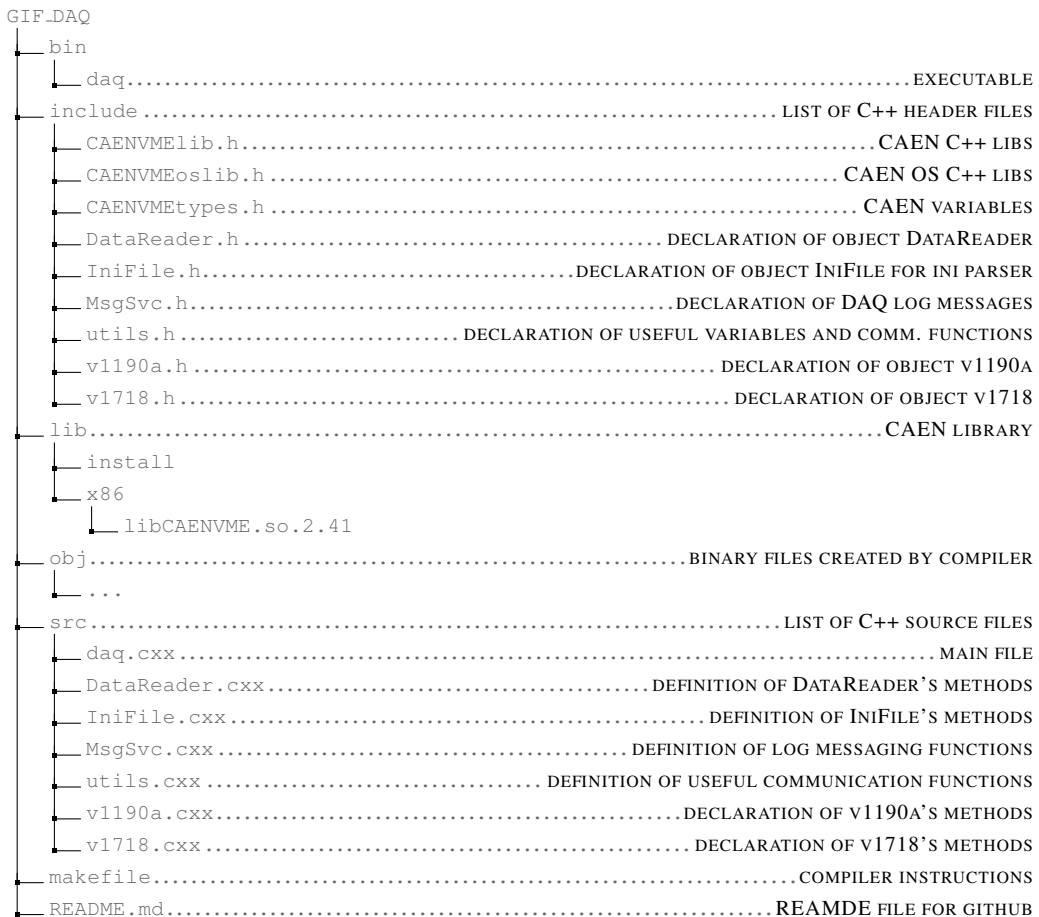
1703 The CAEN VME library will not be packaged by distributions and will need to be installed man-
1704 ually. To compile the GIF++ DAQ project via a terminal, from the DAQ folder use the command:

1705

1706 `make`

1707 The source code tree is provided below along with comments to give an overview of the files' con-
1708 tent. The different objects created for this project (`v1718`, `v1190a`, `IniFile` & `DataReader`) will be
1709 described in details in the following sections.

1710



A.2 Usage of the DAQ

GIF++ DAQ, as used in GIF++, is not a standalone software. Indeed, the system being more complexe, the DAQ only is a sub-layer of the software architecture developped to control and monitor the RPCs that are placed into the bunker for performance study in an irradiated environment. The top layer of GIF++ is a Web Detector Control System (webDCS) application. The DAQ is only called by the webDCS when data needs to be acquired. The webDCS operates the DAQ through command line. To start the DAQ, the webDCS calls:

```
bin/daq /path/to/the/log/file/in/the/output/data/folder
```

where `/path/to/the/log/file/in/the/output/data/folder` is the only argument required. This log file is important for the webDCS as this file contains all the content of the communication of the webDCS and the different systems monitored by the webDCS. Its content is constantly displayed during data taking for the users to be able to follow the operations. The communication messages are normally sent to the webDCS log file via the functions declared in file `MsgSvc.h`, typically `MSG_INFO(string message)`.

1726

A.3 Description of the readout setup

1728 The CMS RPC setup at GIF++ counts 5 V1190A Time-to-Digital Converter (TDC) manufactured
 1729 by CAEN [58]. V1190A are VME units accepting 128 independent Multi-Hit/Multi-Event TDC
 1730 channels whose signals are treated by 4 100 ps high performance TDC chips developed by CERN
 1731 / ECP-MIC Division. The communication between the computer and the TDCs to transfer data is
 1732 done via a V1718 VME master module also manufactured by CAEN and operated from a USB
 1733 port [59]. These VME modules are all hosted into a 6U VME 6021 powered crate manufactured by
 1734 W-Ie-Ne-R than can accommodate up to 21 VME bus cards [60]. These 3 components of the DAQ
 1735 setup are shown in Figure A.1.

1736

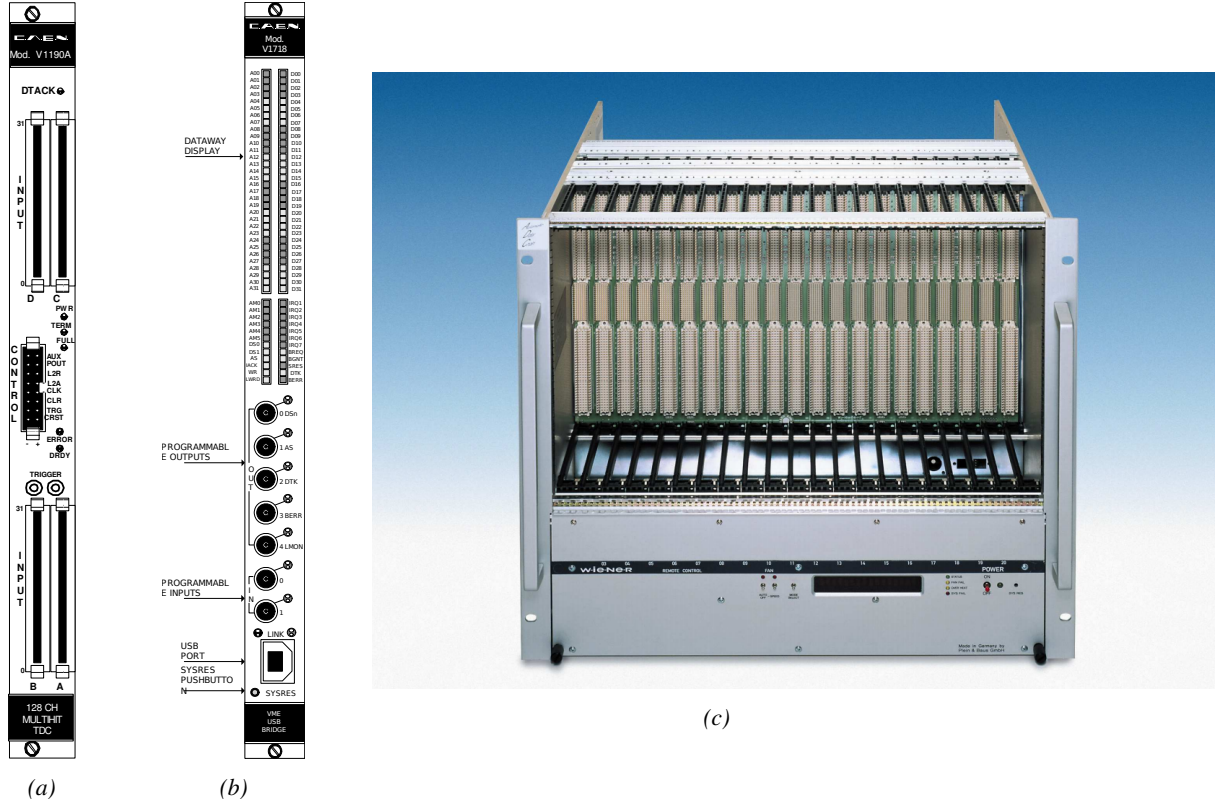


Figure A.1: (A.1a) View of the front panel of a V1190A TDC module [58]. (A.1b) View of the front panel of a V1718 Bridge module [59]. (A.1c) View of the front panel of a 6U 6021 VME crate [60].

1737

A.4 Data read-out

1738 To efficiently perform a data readout algorithm, C++ objects to handle the VME modules (TDCs
 1739 and VME bridge) have been created along with objects to store data and read the configuration file

1740 that comes as an input of the DAQ software.

1741

1742 A.4.1 V1190A TDCs

1743 The DAQ used at GIF takes profit of the *Trigger Matching Mode* offered by V1190A modules.
 1744 This setting is enabled through the method `v1190a::SetTrigMatching (int ntdcs)` where `ntdcs`
 1745 is the total number of TDCs in the setup this setting needs to be enabled for (Source Code A.1). A
 1746 trigger matching is performed in between a trigger time tag, a trigger signal sent into the TRIGGER
 1747 input of the TDC visible on Figure A.1a, and the channel time measurements, signals recorded from
 1748 the detectors under test in our case. Control over this data acquisition mode, explained through
 1749 Figure A.2, is offered via 4 programmable parameters:

- 1750 • **match window:** the matching between a trigger and a hit is done within a programmable time
 1751 window. This is set via the method

1752 `void v1190a::SetTrigWindowWidth(Uint windowHeight, int ntdcs)`

- 1753 • **window offset:** temporal distance between the trigger tag and the start of the trigger matching
 1754 window. This is set via the method

1755 `void v1190a::SetTrigWindowWidth(Uint windowHeight, int ntdcs)`

- 1756 • **extra search margin:** an extended time window is used to ensure that all matching hits are
 1757 found. This is set via the method

1758 `void v1190a::SetTrigSearchMargin(Uint searchMargin, int ntdcs)`

- 1759 • **reject margin:** older hits are automatically rejected to prevent buffer overflows and to speed
 1760 up the search time. This is set via the method

1761 `void v1190a::SetTrigRejectionMargin(Uint rejectMargin, int ntdcs)`

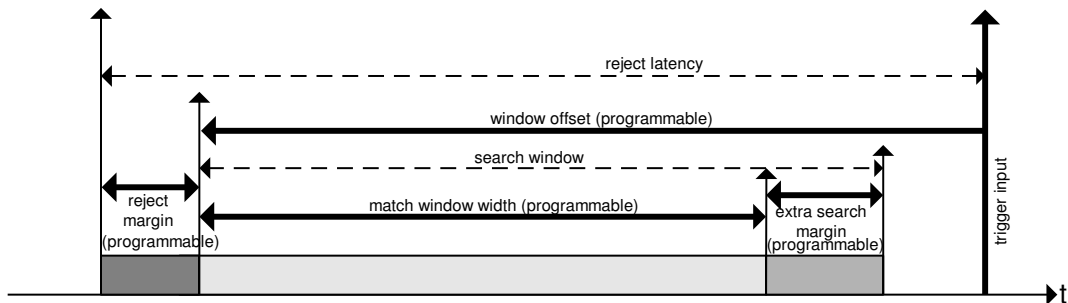


Figure A.2: Module V1190A Trigger Matching Mode timing diagram [58].

1762 Each of these 4 parameters are given in number of clocks, 1 clock being 25 ns long. It is easy to
 1763 understand at this level that there are 3 possible functioning settings:

- 1764 • **1:** the match window is entirely contained after the trigger signal,

- 1765 • **2:** the match window overlaps the trigger signal, or

- 1766 • **3:** the match window is entirely contained before the trigger signal as displayed on Figure A.2.

1767 In both the first and second cases, the sum of the window width and of the offset can be set to
1768 a maximum of 40 clocks, which corresponds to 1 μ s. Evidently, the offset can be negative, allowing
1769 for a longer match window, with the constraint of having the window ending at most 1 μ s after the
1770 trigger signal. In the third case, the maximum negative offset allowed is of 2048 clocks (12 bit) cor-
1771 responding to 51.2 μ s, the match window being strictly smaller than the offset. In the case of GIF++,
1772 the choice has been made to use this last setting by delaying the trigger signal. During the studies
1773 performed in GIF++, both the efficiency of the RPCs, probed using a muon beam, and the noise or
1774 gamma background rate are monitored. The extra search and reject margins are left unused.
1775 To probe the efficiency of RPC detectors, the trigger time tag is provided by the coïncidence of
1776 scintillators when a bunch of muons passes through GIF++ area is used to trigger the data acquisi-
1777 tion. For this measurement, it is useful to reduce the match window width only to contain the muon
1778 information. Indeed, the delay in between a trigger signal and the detection of the corresponding
1779 muon in the RPC being very contant (typically a few tens of ns due to jitter and cable length), the
1780 muon signals are very localised in time. Thus, due to a delay of approximalety 325 ns in between
1781 the muons and the trigger, the settings where chosen to have a window width of 24 clocks (600 ns)
1782 centered on the muon peak thanks to a negative offset of 29 clocks (725 ns).
1783 On the otherhand, monitoring the rates don't require for the DAQ to look at a specific time window.
1784 It is important to integrate enough time to have a robust measurement of the rate as the number of
1785 hits per time unit. The triggerring signal is provided by a pulse generator at a frequency of 300 Hz
1786 to ensure that the data taking occurs in a random way, with respect to beam physics, to probe only
1787 the irradiation spectrum on the detectors. The match window is set to 400 clocks (10 μ s) and the
1788 negative offset to 401 clocks as it needs to exceed the value of the match window.

```

1789
class v1190a
{
    private :
        long             Handle;
        vector<Data32>   Address;
        CVDataWidth      DataWidth;
        CVAddressModifier AddressModifier;

    public:

        v1190a(long handle, IniFile *inifile, int ntdcs);
        ~v1190a();
        Data16 write_op_reg(Data32 address, int code, string error);
        Data16 read_op_reg(Data32 address, string error);
        void Reset(int ntdcs);
        void Clear(int ntdcs);
        void TestWR(Data16 value,int ntdcs);
        void CheckTDCStatus(int ntdcs);
        void CheckCommunication(int ntdcs);
        void SetTDCTestMode(Data16 mode,int ntdcs);
        void SetTrigMatching(int ntdcs);
        void SetTrigTimeSubtraction(Data16 mode,int ntdcs);
        void SetTrigWindowWidth(Uint windowHeight,int ntdcs);
        void SetTrigWindowOffset(Uint windowOffset,int ntdcs);
        void SetTrigSearchMargin(Uint searchMargin,int ntdcs);
        void SetTrigRejectionMargin(Uint rejectMargin,int ntdcs);
        void GetTrigConfiguration(int ntdcs);
        void SetTrigConfiguration(IniFile *inifile,int ntdcs);
        void SetTDCDetectionMode(Data16 mode,int ntdcs);
        void SetTDCResolution(Data16 lsb,int ntdcs);
        void SetTDCDeadTime(Data16 time,int ntdcs);
        void SetTDCHeadTrailer(Data16 mode,int ntdcs);
        void SetTDCEventSize(Data16 size,int ntdcs);
        void SwitchChannels(IniFile *inifile,int ntdcs);
        void SetIRQ(Data32 level, Data32 count,int ntdcs);
        void SetBlockTransferMode(Data16 mode,int ntdcs);
        void Set(IniFile *inifile,int ntdcs);
        void CheckStatus(CVErrorCodes status) const;
        int ReadBlockD32(Uint tdc, const Data16 address,
                         Data32 *data, const Uint words, bool ignore_berr);
        Uint Read(RAWData *DataList,int ntdcs);
};

1790

```

1791 *Source Code A.1: Description of C++ object v1190a.*

1792 The v1190a object, defined in the DAQ software as in Source Code A.1, offers the possibility to
 1793 concatenate all TDCs in the readout setup into a single object containing a list of hardware addresses
 1794 (addresses to access the TDCs' buffer through the VME crate) and each constructor and method acts
 1795 on the list of TDCs.

1796

1797 A.4.2 DataReader

1798 Enabled thanks to v1190a::SetBlockTransferMode(Data16 mode, int ntdcs), the data transfer
 1799 is done via Block Transfer (BLT). Using BLT allows to tranfer a fixed number of events called a
 1800 *block*. This is used together with an Almost Full Level (AFL) of the TDCs' output buffers, defined

1801 through `v1190a::SetIRQ(Data32 level, Data32 count, int ntdcs)`. This AFL gives the maxi-
 1802 mum amount of 32735 words (16 bits, corresponding to the depth of a TDC output buffer) that can
 1803 written in a buffer before an Interrupt Request (IRQ) is generated and seen by the VME Bridge,
 1804 stopping the data acquisition to transfer the content of each TDC buffers before resuming. For each
 1805 trigger, 6 words or more are written into the TDC buffer:

- 1806 • a **global header** providing information of the event number since the beginning of the data
 acquisition,
- 1808 • a **TDC header**,
- 1809 • the **TDC data** (*if any*), 1 for each hit recorded during the event, providing the channel and the
 time stamp associated to the hit,
- 1811 • a **TDC error** providing error flags,
- 1812 • a **TDC trailer**,
- 1813 • a **global trigger time tag** that provides the absolute trigger time relatively to the last reset,
 and
- 1815 • a **global trailer** providing the total word count in the event.

1816 As previously described in Section ??, CMS RPC FEEs provide us with 100 ns long LVDS out-
 1817 put signals that are injected into the TDCs' input. Any avalanche signal that gives a signal above the
 1818 FEEs threshold is thus recorded by the TDCs as a hit within the match window. Each hit is assigned
 1819 to a specific TDC channel with a time stamp, with a precision of 100 ps. The reference time, $t_0 = 0$,
 1820 is provided by the beginning of the match window. Thus for each trigger, coming from a scintillator
 1821 coïncidence or the pulse generator, a list of hits is stored into the TDCs' buffers and will then be
 1822 transferred into a ROOT Tree.

1823 When the BLT is used, it is easy to understand that the maximum number of words that have
 1824 been set as ALF will not be a finite number of events or, at least, the number of events that would
 1825 be recorded into the TDC buffers will not be a multiple of the block size. In the last BLT cycle to
 1826 tranfer data, the number of events to transfer will most propably be lower than the block size. In that
 1827 case, the TDC can add fillers at the end of the block but this option requires to send more data to the
 1828 computer and is thus a little slower. Another solution is to finish the transfer after the last event by
 1829 sending a bus error that states that the BLT reached the last event in the pile. This method has been
 1830 chosen in GIF++.

1832 Due to irradiation, an event in GIF++ can count up to 300 words per TDC. A limit of 4096 words
 1833 (12 bits) has been set to generate IRQ which represent from 14 to almost 700 events depending on
 1834 the average of hits collected per event. Then the block size has been set to 100 events with enabled
 1835 bus errors. When an AFL is reached for one of the TDCs, the VME bridge stops the acquisition by
 1836 sending a BUSY signal.

1838

1839 The data is then transferred one TDC at a time into a structure called `RAWData` (Source Code A.2).

```
1840
1841     struct RAWData{
1842         vector<int>           *EventList;
1843         vector<int>           *NHitsList;
1844         vector<int>           *QFlagList;
1845         vector<vector<int>>   *Channellist;
1846         vector<vector<float>>  *TimeStampList;
1847     };
```

1842 *Source Code A.2: Description of data holding C++ structure `RAWData`.*

1843 In order to organize the data transfer and the data storage, an object called `DataReader` was
1844 created (Source Code A.3). On one hand, it has `v1718` and `v1190a` objects as private members for
1845 communication purposes, such as VME modules settings via the configuration file `*iniFile` or data
1846 read-out through `v1190a::Read()` and on the other hand, it contains the structure `RAWData` that allows
1847 to organise the data in vectors reproducing the tree structure of a ROOT file.

```
1848
1849     class DataReader
1850     {
1851         private:
1852             bool      StopFlag;
1853             IniFile *iniFile;
1854             Data32   MaxTriggers;
1855             v1718    *VME;
1856             int       nTDCs;
1857             v1190a   *TDCs;
1858             RAWData TDCData;
1859
1860         public:
1861             DataReader();
1862             virtual ~DataReader();
1863             void      SetIniFile(string inifilename);
1864             void      SetMaxTriggers();
1865             Data32   GetMaxTriggers();
1866             void      SetVME();
1867             void      SetTDC();
1868             int       GetQFlag(Uint it);
1869             void      Init(string inifilename);
1870             void      FlushBuffer();
1871             void      Update();
1872             string   GetFileName();
1873             void      WriteRunRegistry(string filename);
1874             void      Run();
1875     };
```

1850 *Source Code A.3: Description of C++ object `DataReader`.*

1851 Each event is transferred from `TDCData` and saved into branches of a ROOT `TTree` as 3 integers
1852 that represent the event ID (`EventCount`), the number of hits read from the TDCs (`nHits`), and the
1853 quality flag that provides information for any problem in the data transfer (`qflag`), and 2 lists of
1854 `nHits` elements containing the fired TDC channels (`TDCCh`) and their respective time stamps (`TDCTS`),
1855 as presented in Source Code A.4. The ROOT file file is named using information contained into
1856 the configuration file, presented in section A.5.2. The needed information is extracted using method
1857 `DataReader::GetFileName()` and allow to build the output filename format `ScanXXXXXX_HVX_DAQ.root`

1858 where ScanXXXXXX is a 6 digit number representing the scan number into GIFT++ database and HVX
 1859 the HV step within the scan that can be more than a single digit. An example of ROOT data file is
 1860 provided with Figure A.3.

```
1861
RAWData TDCData;
TFile *outputFile = new TFile(outputFileName.c_str(),"recreate");
TTree *RAWDataTree = new TTree("RAWData","RAWData");

int EventCount = -9;
int nHits = -8;
int qflag = -7;
vector<int> TDCCh;
vector<float> TDCTS;

RAWDataTree->Branch("EventNumber",&EventCount, "EventNumber/I");
RAWDataTree->Branch("number_of_hits",&nHits,"number_of_hits/I");
RAWDataTree->Branch("Quality_flag",&qflag,"Quality_flag/I");
RAWDataTree->Branch("TDC_channel",&TDCCh);
RAWDataTree->Branch("TDC_TimeStamp",&TDCTS);

1862
//...
//Here read the TDC data using v1190a::Read() and place it into
//TDCData for as long as you didn't collect the requested amount
//of data.
//...

for(Uint i=0; i<TDCData.EventList->size(); i++){
    EventCount = TDCData.EventList->at(i);
    nHits = TDCData.NHitsList->at(i);
    qflag = TDCData.QFlagList->at(i);
    TDCCh = TDCData.ChannelList->at(i);
    TDCTS = TDCData.TimeStampList->at(i);
    RAWDataTree->Fill();
}
```

1863 *Source Code A.4: Highlight of the data transfer and organisation within DataReader::Run() after the data has been collected into TDCData.*

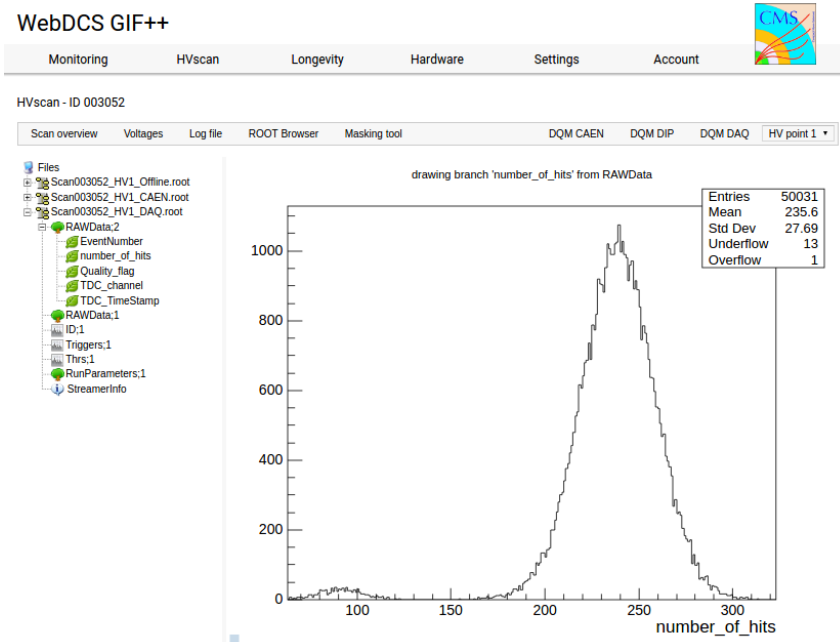


Figure A.3: Structure of the ROOT output file generated by the DAQ. The 5 branches (EventNumber, number_of_hits, Quality_flag, TDC_channel and TDC_TimeStamp) are visible on the left panel of the ROOT browser. On the right panel is visible the histogram corresponding to the variable nHits. In this specific example, there were approximately 50k events recorded to measure the gamma irradiation rate on the detectors. Each event is stored as a single entry in the TTree.

1864 A.4.3 Data quality flag

1865 Among the parameters that are recorded for each event, the quality flag, defined in Source Code A.5,
 1866 is determined on the fly by checking the data recorded by every single TDC. From method `v1190a::Read()`,
 1867 it can be understood that the content of each TDC buffer is readout one TDC at a time. Entries are
 1868 created in the data list for the first TDC and then, when the second buffer is readout, events corre-
 1869 sponding to entries that have already been created to store data for the previous TDC are added to
 1870 the existing list element. On the contrary, when an event entry has not been yet created in the data
 1871 list, a new entry is created.

```
1872
  typedef enum _QualityFlag {
    GOOD      = 1,
    CORRUPTED = 0
} QualityFlag;
```

1874 *Source Code A.5: Definition of the quality flag `enum`.*

1875 It is possible that each TDC buffer contains a different number of events. In cases where the first
 1876 element in the buffer list is an event for corresponds to a new entry, the difference in between the
 1877 entry from the buffer and the last entry in the data list is recorded and checked. If it is greater than 1,
 1878 what should never be the case, the quality flag is set to CORRUPTED for this TDC and an empty entry
 1879 is created in the place of the missing ones. Missing entries are believe to be the result of a bad hold

1880 on the TDC buffers at the moment of the readout. Indeed, the software hold is effective only on 1
 1881 TDC at a time and no solution as been found yet to completely block the writting in the buffers when
 1882 an IRQ is received.

1883 At the end of each BLT cycle, the ID of the last entry stored for each TDC buffer is not recorded.
 1884 When starting the next cycle, if the first entry in the pile corresponds to an event already existing
 1885 in the list, the readout will start from this list element and will not be able to check the difference
 1886 in between this entry's ID and the one of the last entry that was recorded for this TDC buffer in
 1887 the previous cycle. In the case events were missing, the flag stays at its initial value of 0, which is
 1888 similar to CORRUPTED and it is assumed that then this TDC will not contribute to `number_of_hits`,
 1889 `TDC_channel` or `TDC_TimeStamp`.

1890 Finally, since there will be 1 `RAWData` entry per TDC for each event (meaning `nTDCs` entries,
 1891 referring to `DataReader` private attribute), the individual flags of each TDC will be added together.
 1892 The final format is an integer composed `nTDCs` digits where each digit is the flag of a specific TDC.
 1893 This is constructed using powers of 10 like follows:

```
1894     TDC 0: QFlag = 100 × _QualityFlag
1895     TDC 1: QFlag = 101 × _QualityFlag
1896     ...
1897     TDC N: QFlag = 10N × _QualityFlag
```

1898 and the final flag to be with N digits:

```
1899     QFlag = n....3210
```

1900 each digit being 1 or 0. Below is given an example with a 4 TDCs setup.

1901 If all TDCs were good : `QFlag = 1111`,

1902 but if TDC 2 was corrupted : `QFlag = 1011`.

1903 When data taking is over and the data contained in the dynamical `RAWData` structure is transferred
 1904 to the ROOT file, all the 0s are changed into 2s by calling the method `DataReader::GetQFlag()`.
 1905 This will help translating the flag without knowing the number of TDCs beforehand. Indeed, a flag
 1906 111 could be due to a 3 TDC setup with 3 good individual TDC flags or to a more than 3 TDC setup
 1907 with TDCs those ID is greater than 2 being CORRUPTED, thus giving a 0.

1908 The quality flag has been introduced quite late, in October 2017 only, to the list of GIFT++ DAQ
 1909 parameters to be recorded into the output ROOT file. Before this addition, the missing data, corrupting
 1910 the quality for the offline analysis, was contributing to artificially fill data with lower multiplicity.
 1911 Looking at `TBranch number_of_hits` provides an information about the data of the full GIFT++
 1912 setup. When a TDC is not able to transfer data for a specific event, the effect is a reduction of the
 1913 total number of hits recorded in the full setup, this is what can be seen from Figure A.4. After offline
 1914 reconstruction detector by detector, the effect of missing events can be seen in the artificially filled
 1915 bin at multiplicity 0 shown in Figure A.5. Nonetheless, for data with high irradiation levels, as it is
 1916 the case for Figure A.5a, discarding the fake multiplicity 0 data can be done easily during the offline
 1917 analysis. At lower radiation, the missing events contribution becomes more problematic as the multi-
 1918 tiplicity distribution overlaps the multiplicity 0 and that in the same time the proportion of missing

events decreases. Attempts to fit the distribution with a Poisson or skew distribution function were not conclusive and this very problem has been at the origin of the quality flag that allows to give a non ambiguous information about each event quality.

1922

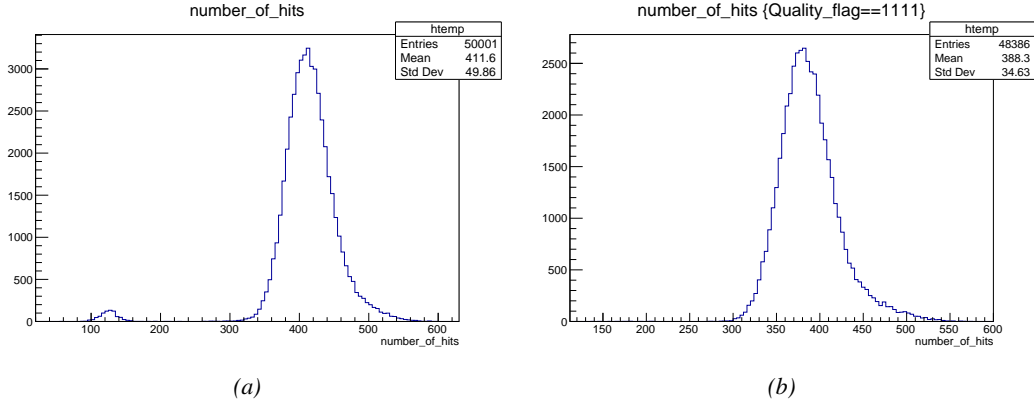


Figure A.4: The effect of the quality flag is explained by presenting the content of TBranch `number_of_hits` of a data file without `Quality_flag` in Figure A.4a and the content of the same TBranch for data corresponding to a `Quality_flag` where all TDCs were labelled as `GOOD` in Figure A.4b taken with similar conditions. It can be noted that the number of entries in Figure A.4b is slightly lower than in Figure A.4a due to the excluded events.

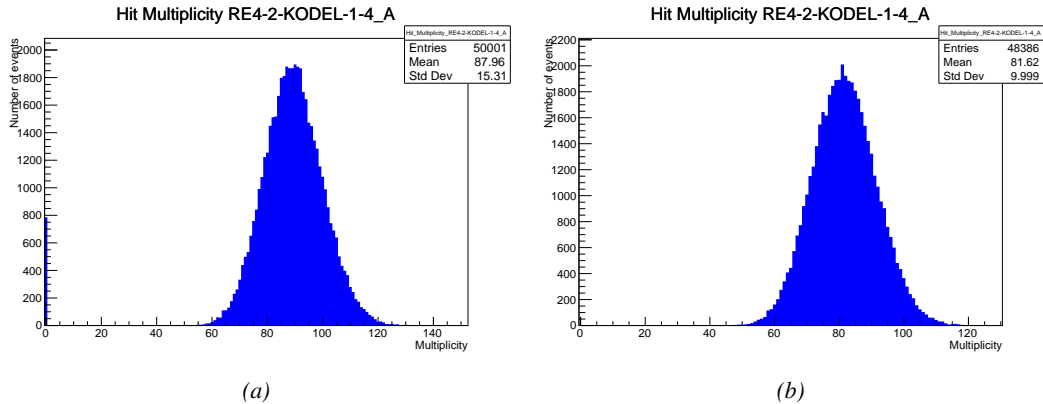


Figure A.5: Using the same data as previously showed in Figure A.4, the effect of the quality flag is explained by presenting the reconstructed hit multiplicity of a data file without `Quality_flag` in Figure A.5a and the reconstructed content of the same RPC partition for data corresponding to a `Quality_flag` where all TDCs were labelled as `GOOD` in Figure A.5b taken with similar conditions. The artificial high content of bin 0 is completely suppressed.

1923

A.5 Communications

1924 To ensure data readout and dialog in between the machine and the TDCs or in between the webDCS
1925 and the DAQ, different communication solutions were used. First of all, it is important to have a

1926 module to allow the communication in between the TDCs and the computer from which the DAQ
 1927 operates. When this communication is effective, shifters using the webDCS to control data taking
 1928 can thus send instructions to the DAQ.

1929

1930 A.5.1 V1718 USB Bridge

1931 In the previous section, the data transfer has been discussed. The importance of the `v1718` object
 1932 (Source Code A.6), used as private member of `DataReader`, was not explicated. VME master
 1933 modules are used for communication purposes as they host the USB port that connects the pow-
 1934 ered crate buffer to the computer where the DAQ is installed. From the source code point of view,
 1935 this object is used to control the communication status, by reading the returned error codes with
 1936 `v1718::CheckStatus()`, or to check for IRQs coming from the TDCs through `v1718::CheckIRQ()`.
 1937 Finally, to ensure that triggers are blocked at the hardware level, a NIM pulse is sent out of one of the
 1938 5 programmable outputs (`v1718::SendBUSY()`) to the VETO of the coincidence module where the
 1939 trigger signals originate from. As long as this signal is ON, no trigger can reach the TDCs anymore.
 1940

```
1941 class v1718{
1942     private:
1943         int Handle;
1944         Data32 Data;           // Data
1945         CVIRQLevels Level;    // Interrupt level
1946         CVAddressModifier AM;   // Addressing Mode
1947         CVDataWidth dataSize; // Data Format
1948         Data32 BaseAddress;   // Base Address
1949
1950     public:
1951         v1718(IniFile *inifile);
1952         ~v1718();
1953         long GetHandle(void) const;
1954         int SetData(Data16 data);
1955         Data16 GetData(void);
1956         int SetLevel(CVIRQLevels level);
1957         CVIRQLevels GetLevel(void);
1958         int SetAM(CVAddressModifier am);
1959         CVAddressModifier GetAM(void);
1960         int SetDatasize(CVDataWidth datasize);
1961         CVDataWidth GetDataSize(void);
1962         int SetBaseAddress(Data16 baseaddress);
1963         Data16 GetBaseAddress(void);
1964         void CheckStatus(CVErrorCodes status) const;
1965         bool CheckIRQ();
1966         void SetPulsers();
1967         void SendBUSY(BusyLevel level);
1968     };
1969 }
```

1942 *Source Code A.6: Description of C++ object v1718.*

1943 A.5.2 Configuration file

1944 The DAQ software takes as input a configuration file written using INI standard [61]. This file is
 1945 partly filled with the information provided by the shifters when starting data acquisition using the
 1946 webDCS, as shown by Figure A.6. This information is written in section [`General`] and will later

1947 be stored in the ROOT file that contains the DAQ data as can be seen from Figure A.3. Indeed,
 1948 another `TTree` called `RunParameters` as well as the 2 histograms `ID`, containing the scan number,
 1949 start and stop time stamps, and `Triggers`, containing the number of triggers requested by the shifter,
 1950 are available in the data files. Moreover, `ScanID` and `HV` are then used to construct the file name
 1951 thanks to the method `DataReader::GetFileName()`.

WebDCS GIF++

Monitoring HVscan Longevity Hardware Settings Account 

DAQ High Voltage Scan

Type scan: Rate Scan Comments:

Source configuration: Source OFF U 333 D 333 HV after scan: Turn off

Beam configuration: Beam OFF

Waiting time: 1 (min)

Trigger mode: External Internal Random

Minimal measure time: 10 (min)

Chamber	RE2-2-NPD-BARC-8	RE4-2-CERN-106	RE2-3-NPD-BARC-9	RE4-2-CERN-165	RE4-2-KODEL-1-4	Max triggers
HV _{eff} 1	8600	8500	8600	8500	6500	
HV _{eff} 2	8700	8600	8700	8600	6600	
HV _{eff} 3	8800	8700	8800	8700	6700	
HV _{eff} 4	8900	8800	8900	8800	6800	
HV _{eff} 5	9000	8900	9000	8900	6900	
HV _{eff} 6	9100	9000	9100	9000	7000	
HV _{eff} 7	9200	9100	9200	9100	7100	
HV _{eff} 8	9300	9200	9300	9200	7200	
HV _{eff} 9	9400	9300	9400	9300	7300	
HV _{eff} 10	9500	9400	9500	9400	7400	

Start HV scan

Figure A.6: WebDCS DAQ scan page. On this page, shifters need to choose the type of scan (Rate, Efficiency or Noise Reference scan), the gamma source configuration at the moment of data taking, the beam configuration, and the trigger mode. These information will be stored in the DAQ ROOT output. Are also given the minimal measurement time and waiting time after ramping up of the detectors is over before starting the data acquisition. Then, the list of HV points to scan and the number of triggers for each run of the scan are given in the table underneath.

1952 The rest of the information is written beforehand in the configuration file template, as explicated
 1953 in Source Code A.7, and contains the hardware addresses to the different VME modules in the
 1954 setup as well as settings for the TDCs. As the TDC settings available in the configuration file are not
 1955 supposed to be modified, an improvement would be to remove them from the configuration file and
 1956 to hardcode them inside of the DAQ code itself or to place them into a different INI file that would
 1957 host only the TDC settings to lower the probability for a bad manipulation of the configuration file
 1958 that can be modified from one of webDCS' menus.

1959

```

[General]
TdcS=4
ScanID=$scanid
HV=$HV
RunType=$runtype
MaxTriggers=$maxtriggers
Beam=$beam
[VMEInterface]
Type=V1718
BaseAddress=0xFF0000
Name=VmeInterface
[TDC0]
Type=V1190A
BaseAddress=0x00000000
Name=Tdc0
StatusA00-15=1
StatusA16-31=1
StatusB00-15=1
StatusB16-31=1
StatusC00-15=1
StatusC16-31=1
StatusD00-15=1
StatusD16-31=1
[TDC1]
Type=V1190A
BaseAddress=0x11110000
Name=Tdc1
StatusA00-15=1
StatusA16-31=1
StatusB00-15=1
StatusB16-31=1
StatusC00-15=1
StatusC16-31=1
StatusD00-15=1
StatusD16-31=1
[TDC2]
Type=V1190A
BaseAddress=0x22220000
Name=Tdc2
StatusA00-15=1
StatusA16-31=1
StatusB00-15=1
StatusB16-31=1
StatusC00-15=1
StatusC16-31=1
StatusD00-15=1
StatusD16-31=1
[TDC3]
Type=V1190A
BaseAddress=0x44440000
Name=Tdc3
StatusA00-15=1
StatusA16-31=1
StatusB00-15=1
StatusB16-31=1
StatusC00-15=1
StatusC16-31=1
StatusD00-15=1
StatusD16-31=1
[TDCSettings]
TriggerExtraSearchMargin=0
TriggerRejectMargin=0
TriggerTimeSubtraction=0b1
TdcDetectionMode=0b01
TdcResolution=0b10
TdcDeadTime=0b00
TdcHeadTrailer=0b1
TdcEventSize=0b1001
TdcTestMode=0b0
BLTMode=1

```

1960

Source Code A.7: INI configuration file template for 4 TDCs. In section [General], the number of TDCs is explicitated and information about the ongoing run is given. Then, there are sections for each and every VME modules. There buffer addresses are given and for the TDCs, the list of channels to enable is given. Finally, in section [TDCSettings], a part of the TDC settings are given.

1961
 1962 In order to retrieve the information of the configuration file, the object `IniFile` has been developed
 1963 to provide an INI parser, presented in Source Code A.8. It contains private methods returning a
 1964 boolean to check the type of line written in the file, whether a comment, a group header or a key line
 1965 (`IniFile::CheckIfComment()`, `IniFile::CheckIfGroup()` and `IniFile::CheckIfToken()`). The
 1966 key may sometimes be referred to as *token* in the source code. Moreover, the private element
 1967 `FileData` is a map of `const string` to `string` that allows to store the data contained inside the
 1968 configuration file via the public method `IniFile::GetFileData()` following the formatting (see
 1969 method `IniFile::Read()`):

```
1970
  1971     string group, token, value;
  // Get the field values for the 3 strings.
  // Then concatenate group and token together as a single string
  // with a dot separation.
  token = group + "." + token;
  FileData[token] = value;
```

1972 More methods have been written to translate the different keys into the right variable format
 1973 when used by the DAQ. For example, to get a `float` value out of the configuration file data, knowing
 1974 the group and the key needed, the method `IniFile::floatType()` can be used. It takes 3 arguments
 1975 being the group name and key name (both `string`), and a default `float` value used as exception in
 1976 the case the expected combination of group and key cannot be found in the configuration file. This
 1977 default value is then used and the DAQ continues on working after sending an alert in the log file for
 1978 further debugging.

```

1979 typedef map< const string, string > IniFileData;
1980
class IniFile{
    private:
        bool          CheckIfComment (string line);
        bool          CheckIfGroup(string line, string& group);
        bool          CheckIfToken(string line, string& key, string& value);
        string         FileName;
        IniFileData   FileData;
        int           Error;

    public:
        IniFile();
        IniFile(string filename);
        virtual      ~IniFile();

        // Basic file operations
        void          SetFileName(string filename);
        int           Read();
        int           Write();
        IniFileData GetFileData();

        // Data readout methods
        Data32         addressType (string groupname, string keyname, Data32
→     defaultvalue);
        long          intType     (string groupname, string keyname, long
→     defaultvalue);
        long long    longType    (string groupname, string keyname, long long
→     defaultvalue );
        string         stringType  (string groupname, string keyname, string
→     defaultvalue );
        float         floatType   (string groupname, string keyname, float
→     defaultvalue );

        // Error methods
        string         GetErrorMsg();
    };

```

1981 *Source Code A.8: Description of C++ object `IniFile` used as a parser for INI file format.*

1982 A.5.3 WebDCS/DAQ intercommunication

1983 When shifters send instructions to the DAQ via the configuration file, it is the webDCS itself that
 1984 gives the start command to the DAQ and then the 2 softwares use inter-process communication
 1985 through file to synchronise themselves. This communication file is represented by the variable **const**
 1986 **string** __runstatuspath.

1987 On one side, the webDCS sends commands or status that are readout by the DAQ:

- 1988 ● INIT, status sent when launching a scan and read via function `CtrlRunStatus(...)`,
- 1989 ● START, command to start data taking and read via function `CheckSTART()`,
- 1990 ● STOP, command to stop data taking at the end of the scan and read via function `CheckSTOP()`,
 1991 and
- 1992 ● KILL, command to kill data taking sent by user and read via function `CheckKILL()`

1993 and on the other, the DAQ sends status that are controled by the webDCS:

- 1994 ● `DAQ_RDY`, sent with `SendDAQReady()` to signify that the DAQ is ready to receive commands
1995 from the webDCS,
- 1996 ● `RUNNING`, sent with `SendDAQRunning()` to signify that the DAQ is taking data,
- 1997 ● `DAQ_ERR`, sent with `SendDAQError()` to signify that the DAQ didn't receive the expected com-
1998 mand from the webDCS or that the launch command didn't have the right number of argu-
1999 ments,
- 2000 ● `RD_ERR`, sent when the DAQ wasn't able to read the communication file, and
- 2001 ● `WR_ERR`, sent when the DAQ wasn't able to write into the communication file.

2002 **A.5.4 Example of inter-process communication cycle**

2003 Under normal conditions, the webDCS and the DAQ processes exchange commands and status via
2004 the file hosted at the address `__runstatuspath`, as explained in subsection A.5.3. An example of
2005 cycle is given in Table A.1. In this example, the steps 3 to 5 are repeated as long as the webDCS tells
2006 the DAQ to take data. A data taking cycle is the equivalent as what is called a *Scan* in GIFT++ jargon,
2007 referring to a set a runs with several HV steps. Each repetition of steps 3 to 5 is then equivalent to a
2008 single *Run*.

2009

2010 At any moment during the data taking, for any reason, the shifter can decide that the data taking
2011 needs to be stopped before it reached the end of the scheduled cycle. Thus at any moment on the
2012 cycle, the content of the inter-process communication file will be changed to `KILL` and the DAQ will
2013 shut down right away. The DAQ checks for `KILL` signals every 5s after the TDCs configuration is
2014 over. So far, the function `CheckKILL()` has been used only inside of the data taking loop of method
2015 `DataReader::Run()` and thus, if the shifter decides to KILL the data taking during the TDC con-
2016 figuration phase or the HV ramping in between 2 HV steps, the DAQ will not be stopped smoothly
2017 and a *force kill* command will be sent to stop the DAQ process that is still awake on the computer.
2018 Improvements can be brought on this part of the software to make sure that the DAQ can safely
2019 shutdown at any moment.

2020

2021 **A.6 Software export**

2022 In section A.2 was discussed the fact that the DAQ as written in its last version is not a standalone
2023 software. It is possible to make it a standalone program that could be adapted to any VME setup
2024 using V1190A and V1718 modules by creating a GUI for the software or by printing the log mes-
2025 sages that are normally printed in the webDCS through the log file, directly into the terminal. This
2026 method was used by the DAQ up to version 3.0 moment where the webDCS was completed. Also, it
2027 is possible to check branches of DAQ v2.X to have example of communication through a terminal.

2028

2029 DAQ v2.X is nonetheless limited in it's possibilities and requires a lot of offline manual interven-
2030 tions from the users. Indeed, there is no communication of the software with the detectors' power
2031 supply system that would allow for a user a predefine a list of voltages to operate the detectors at

step	actions of webDCS	status of DAQ	<code>__runstatuspath</code>
1	launch DAQ ramp voltages ramping over wait for currents stabilization	readout of IniFile configuration of TDCs	INIT
2		configuration done send DAQ ready wait for START signal	DAQ_RDY
3	waiting time over send START		START
4	wait for run to end monitor DAQ run status	data taking ongoing check for KILL signal	RUNNING
5		run over send DAQ_RDY wait for next DCS signal	DAQ_RDY
6	ramp voltages ramping over wait for currents stabilization		DAQ_RDY
3	waiting time over send START		START
4	wait for run to end monitor DAQ run status	update IniFile information data taking ongoing check for KILL signal	RUNNING
5		run over send DAQ_RDY wait for next DCS signal	DAQ_RDY
7	send command STOP	DAQ shuts down	STOP

Table A.1: Inter-process communication cycles in between the webDCS and the DAQ through file string signals.

2032 and loop over to take data without any further manual intervention. In v2.X, the data is taken for a
2033 single detector setting and at the end of each run, the softwares asks the user if he intends on taking
2034 more runs. If so, the software invites the user to set the operating voltages accordingly to what is
2035 necessary and to manual update the configuration file in consequence. This working mode can be a
2036 very first approach before an evolution and has been successfully used by colleagues from different
2037 collaborations.

2038
2039 For a more robust operation, it is recommended to develop a GUI or a web application to inter-
2040 face the DAQ. Moreover, to limit the amount of manual interventions, and thus the probability to
2041 make mistakes, it is also recommended to add an extra feature into the DAQ by installing the HV
2042 Wrapper library provided by CAEN of which an example of use in a similar DAQ software devel-
2043 opped by a master student of UGent, and called TinyDAQ, is provided on UGent's github. Then, this
2044 HV Wrapper will help you communicating with and give instructions to a CAEN HV powered crate
2045 and can be added into the DAQ at the same level where the communication with the user was made
2046 in DAQ v2.X. In case you are using another kind of power system for your detectors, it is stringly
2047 adviced to use HV modules or crates that can be remotely controled via a using C++ libraries.
2048

B

2049

2050

Details on the offline analysis package

2051 The data collected in GIF++ thanks to the DAQ described in Appendix A is difficult to interpret by
2052 a human user that doesn't have a clear idea of the raw data architecture of the ROOT data files. In
2053 order to render the data human readable, a C++ offline analysis tool was designed to provide users
2054 with detector by detector histograms that give a clear overview of the parameters monitored during
2055 the data acquisition [62]. In this appendix, details about this software in the context of GIF++, as of
2056 how the software was written and how it functions will be given.

2057 **B.1 GIF++ Offline Analysis file tree**

2058 GIF++ Offline Analysis source code is fully available on github at https://github.com/aafagot/GIF_OfflineAnalysis. The software requires ROOT as non-optionnal dependency
2059 as it takes ROOT files in input and write an output ROOT file containing histograms. To compile the
2060 GIF++ Offline Analysis project is compiled with cmake. To compile, first a build/ directory must
2061 be created to compile from there:

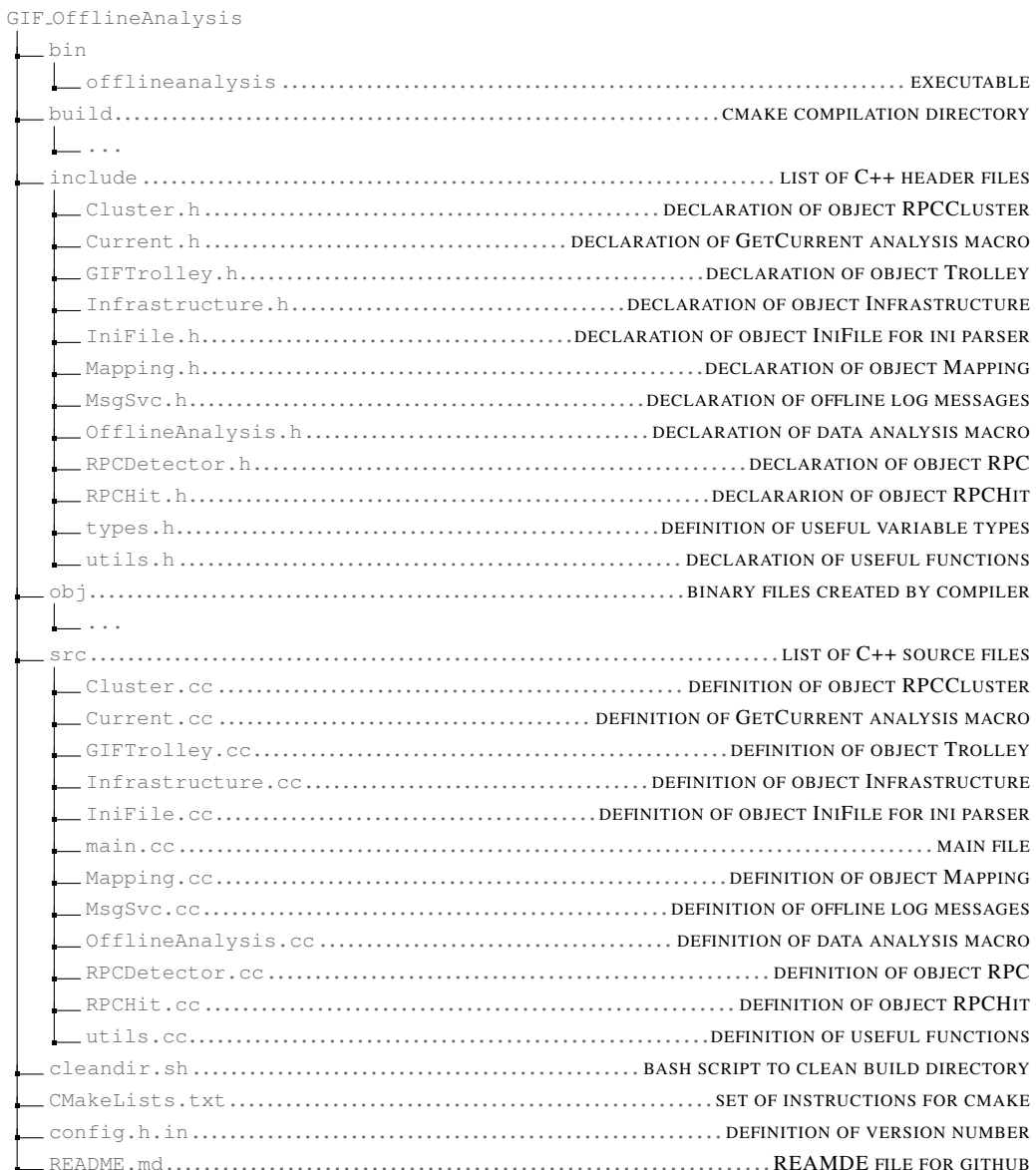
```
2063 mkdir build
2064 cd build
2065 cmake ..
2066 make
2067 make install
```

2068 To clean the directory and create a new build directory, the bash script cleandir.sh can be used:

```
2066
2067 ./cleandir.sh
```

2068 The source code tree is provided below along with comments to give an overview of the files' con-
2069 tent. The different objects created for this project (`Infrastructure`, `Trolley`, `RPC`, `Mapping`, `RPCHit`,
2070 `RPCCluster` and `Inifile`) will be described in details in the following sections.

2071



2072

B.2 Usage of the Offline Analysis

2073

In order to use the Offline Analysis tool, it is necessary to know the Scan number and the HV Step of the run that needs to be analysed. This information needs to be written in the following format:

2075

2076

```
Scan00XXXX_HVY
```

2077

where XXXX is the scan ID and Y is the high voltage step (in case of a high voltage scan, data will be taken for several HV steps). This format corresponds to the base name of data files in the database

2078

2079 of the GIF++ webDCS. Usually, the offline analysis tool is automatically called by the webDCS at
 2080 the end of data taking or by a user from the webDCS panel if an update of the tool was brought.
 2081 Nonetheless, an expert can locally launch the analysis for tests on the GIF++ computer, or a user can
 2082 get the code on its local machine from github and download data from the webDCS for its own anal-
 2083 ysis. To launch the code, the following command can be used from the `GIF_OfflineAnalysis` folder:

2084

```
2085 bin/offlineanalysis /path/to/Scan00XXXX_HVY
```

2086 where, `/path/to/Scan00XXXX_HVY` refers to the local data files. Then, the offline tool will by itself
 2087 take care of finding all available ROOT data files present in the folder, as listed below:

2088

- `Scan00XXXX_HVY_DAQ.root` containing the TDC data as described in Appendix ?? (events, hit
 2089 and timestamp lists), and
- `Scan00XXXX_HVY_CAEN.root` containing the CAEN mainframe data recorded by the monitor-
 2090 ing tool webDCS during data taking (HVs and currents of every HV channels). This file is
 2092 created independently of the DAQ.

2093

B.2.1 Output of the offline tool

2094

B.2.1.1 ROOT file

2095

The analysis gives in output ROOT datafiles that are saved into the data folder and called using the
 2096 naming convention `Scan00XXXX_HVY_Offline.root`. Inside those, a list of `TH1` histograms can be
 2097 found. Its size will vary as a function of the number of detectors in the setup as each set of histograms
 2098 is produced detector by detector. For each partition of each chamber, can be found:

2099

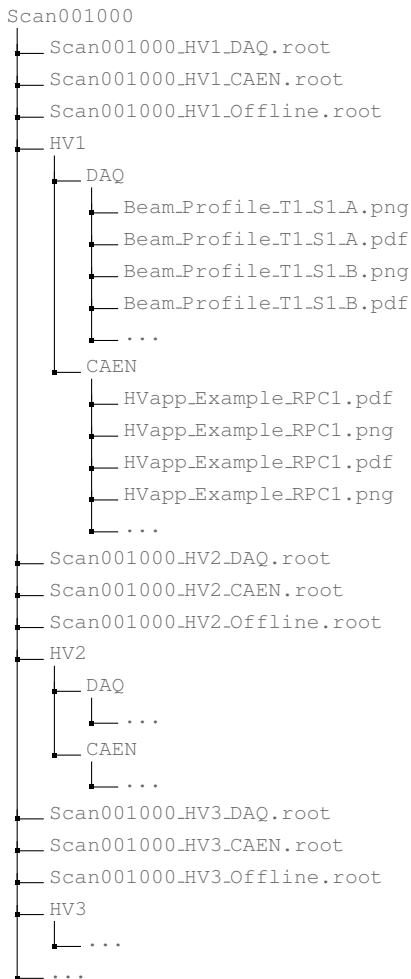
- `Time_Profile_Tt_Sc_p` shows the time profile of all recorded events (number of events per
 2100 time bin),
- `Hit_Profile_Tt_Sc_p` shows the hit profile of all recorded events (number of events per chan-
 2102 nel),
- `Hit_Multiplicity_Tt_Sc_p` shows the hit multiplicity (number of hits per event) of all recorded
 2104 events (number of occurrences per multiplicity bin),
- `Strip_Mean_Noise_Tt_Sc_p` shows noise/gamma rate per unit area for each strip in a se-
 2106 lected time range. After filters are applied on `Time_Profile_Tt_Sc_p`, the filtered version
 2107 of `Hit_Profile_Tt_Sc_p` is normalised to the total integrated time and active detection area
 2108 of a single channel,
- `Strip_Activity_Tt_Sc_p` shows noise/gamma activity for each strip (normalised version of
 2110 previous histogram - strip activity = strip rate / average partition rate),
- `Strip_Homogeneity_Tt_Sc_p` shows the *homogeneity* of a given partition ($\text{homogeneity} = \exp(-\text{strip rates standard deviation(strip rates in partition/average partition rate)})$),
- `mask_Strip_Mean_Noise_Tt_Sc_p` shows noise/gamma rate per unit area for each masked
 2114 strip in a selected time range. Offline, the user can control the noise/gamma rate and decide to
 2115 mask the strips that are judged to be noisy or dead. This is done via the *Masking Tool* provided
 2116 by the webDCS,

- 2117 ● `mask_Strip_Activity_Tt_Sc_p` shows noise/gamma activity per unit area for each masked
2118 strip with respect to the average rate of active strips,
- 2119 ● `NoiseCSize_H_Tt_Sc_p` shows noise/gamma cluster size, a cluster being constructed out of
2120 adjacent strips giving a signal at the *same time* (hits within a time window of 25 ns),
- 2121 ● `NoiseCMult_H_Tt_Sc_p` shows noise/gamma cluster multiplicity (number of reconstructed
2122 clusters per event),
- 2123 ● `Chip_Mean_Noise_Tt_Sc_p` shows the same information than `Strip_Mean_Noise_Tt_Scp` us-
2124 ing a different binning (1 chip corresponds to 8 strips),
- 2125 ● `Chip_Activity_Tt_Sc_p` shows the same information than `Strip_Activity_Tt_Scp` using
2126 chip binning,
- 2127 ● `Chip_Homogeneity_Tt_Sc_p` shows the homogeneity of a given partition using chip binning,
- 2128 ● `Beam_Profile_Tt_Sc_p` shows the estimated beam profile when taking efficiency scan. This
2129 is obtained by filtering `Time_Profile_Tt_Sc_p` to only consider the muon peak where the
2130 noise/gamma background has been subtracted. The resulting hit profile corresponds to the
2131 beam profile on the detector channels,
- 2132 ● `L0_Efficiency_Tt_Sc_p` shows the level 0 efficiency that was estimated **without** muon track-
2133 ing,
- 2134 ● `MuonCSize_H_Tt_Sc_p` shows the level 0 muon cluster size that was estimated **without** muon
2135 tracking, and
- 2136 ● `MuonCMult_H_Tt_Sc_p` shows the level 0 muon cluster multiplicity that was estimated **without**
2137 muon tracking.

2138 In the histogram labels, t stands for the trolley number (1 or 3), c for the chamber slot label in
2139 trolley t and p for the partition label (A, B, C or D depending on the chamber layout) as explained
2140 in Chapter ??.

2141 In the context of GIF++, an extra script called by the webDCS is called to extract the histograms
2142 from the ROOT files. The histograms are then stored in PNG and PDF formats into the correspond-
2143 ing folder (a single folder per HV step, so per ROOT file). the goal is to then display the histograms
2144 on the Data Quality Monitoring (DQM) page of the webDCS in order for the users to control the
2145 quality of the data taking at the end of data taking. An example of histogram organisation is given
2146 below:

2147



2149 *Here can put some screens from the webDCS to show the DQM and the plots available to users.*
 2150

2151 **B.2.1.2 CSV files**

2152 Moreover, up to 3 CSV files can be created depending on which ones of the 3 input files were in the
 2153 data folder:

- 2154 • `Offline-Corrupted.csv` , is used to keep track of the amount of data that was corrupted and
 2155 removed from old data format files that don't contain any data quality flag.
- 2156 • `Offline-Current.csv` , contains the summary of the currents and voltages applied on each
 2157 RPC HV channel.
- 2158 • `Offline-L0-EffC1.csv` , is used to write the efficiencies, cluster size and cluster multiplicity
 2159 of efficiency runs. Note that `L0` refers here to *Level 0* and means that the results of efficiency and
 2160 clusterization are a first approximation calculated without performing any muon tracking in

2161 between the different detectors. This offline tool provides the user with a preliminar calculation
 2162 of the efficiency and of the muon event parameters. Another analysis software especially
 2163 dedicated to muon tracking is called on selected data to retrieve the results of efficiency and
 2164 muon clusterization using a tracking algorithm to discriminate noise or gamma from muons
 2165 as muons are the only particles that pass through the full setup, leaving hits than can be used
 2166 to reconstruct their tracks.

- 2167 • `Offline-Rate.csv`, is used to write the noise or gamma rates measured in the detector readout
 2168 partitions.

2169 Note that these 4 CSV files are created along with their *headers* (`Offline-[...]-Header.csv`
 2170 containing the names of each data columns) and are automatically merged together when the offline
 2171 analysis tool is called from the webDCS, contrary to the case where the tool is runned locally from
 2172 the terminal as the merging bash script is then not called. Thus, the resulting files, used to make
 2173 official plots, are:

- 2174 • `Corrupted.csv`,
 2175 • `Current.csv`,
 2176 • `L0-EffCl.csv`.
 2177 • `Rate.csv`.

2178 B.3 Analysis inputs and information handling

2179 The usage of the Offline Analysis tool as well as its output have been presented in the previous section.
 2180 It is now important to dig further and start looking at the source code and the inputs necessary
 2181 for the tool to work. Indeed, other than the raw ROOT data files that are analysed, more information
 2182 needs to be imported inside of the program to perform the analysis such as the description of the
 2183 setup inside of GIFT++ at the time of data taking (number of trolleys, of RPCs, dimensions of the
 2184 detectors, etc...) or the mapping that links the TDC channels to the coresponding RPC channels in
 2185 order to translate the TDC information into human readable data. 2 files are used to transmit all this
 2186 information:
 2187

- 2188 • `Dimensions.ini`, that provides the necessary setup and RPC information, and
 2189 • `ChannelsMapping.csv`, that gives the link between the TDC and RPC channels as well as the
 2190 *mask* for each channel (masked or not?).

2191 B.3.1 Dimensions file and InFile parser

2192 This input file, present in every data folder, allows the analysis tool to know of the number of active
 2193 trolleys, the number of active RPCs in those trolleys, and the details about each RPCs such as
 2194 the number of RPC gaps, the number of pseudo-rapidity partitions (for CMS-like prototypes), the
 2195 number of strips per partion or the dimensions. To do so, there are 3 types of groups in the INI file
 2196 architecture. A first general group, appearing only once at the head of the document, gives information
 2197 about the number of active trolleys as well as their IDs, as presented in Source Code B.1. For

2198 each active trolley, a group similar to Source Code B.2 can be found containing information about
 2199 the number of active detectors in the trolley and their IDs. Each trolley group as a `Tt` name format,
 2200 where `t` is the trolley ID. Finally, for each detector stored in slots of an active trolley, there is a group
 2201 providing information about their names and dimensions, as shown in Source Code B.3. Each slot
 2202 group as a `TtSs` name format, where `s` is the slot ID of trolley `t` where the active RPC is hosted.

```
2203 [General]
2204 nTrolleys=2
2205 TrolleysID=13
```

2205 *Source Code B.1: Example of `[General]` group as might be found in `Dimensions.ini`. In Gif++, only 2 trolleys are available to hold RPCs and place them inside of the bunker for irradiation. The IDs of the trolleys are written in a single string as "13" and then read character by character by the program.*

```
2206 [T1]
2207 nSlots=4
2208 SlotsID=1234
```

2207 *Source Code B.2: Example of trolley group as might be found in `Dimensions.ini`. In this example, the file tells that there are 4 detectors placed in the holding slots of the trolley `T1` and that their IDs, written as a single string variable, are 1, 2, 3 and 4.*

```
2208 [T1S1]
Name=RE2-2-NPD-BARC-8
Partitions=3
Gaps=3
Gap1=BOT
Gap2=TN
Gap3=TW
AreaGap1=11694.25
AreaGap2=6432
AreaGap3=4582.82
Strips=32
ActiveArea-A=157.8
ActiveArea-B=121.69
ActiveArea-C=93.03
```

2209 *Source Code B.3: Example of slot group as might be found in `Dimensions.ini`. In this example, the file provides information about a detector named `RE2-2-NPD-BARC-8`, having 3 pseudo-rapidity readout partitions and stored in slot `S1` of trolley `T1`. This is a CMS RE2-2 type of detector. This information will then be used for example to compute the rate per unit area calculation.*

2210 This information is readout and stored in a C++ object called `IniFile`, that parses the information
 2211 in the INI input file and stores it into a local buffer for later use. This INI parser is the exact same
 2212 one that was previously developed for the Gif++ DAQ and described in Appendix A.5.2.

2213 B.3.2 TDC to RPC link file and Mapping

2214 The same way the INI dimension file information is stored using `map`, the channel mapping and mask
 2215 information is stored and accessed through `map`. First of all, the mapping CSV file is organised into
 2216 3 columns separated by tabulations (and not by commas, as expected for CSV files as it is easier using
 2217 streams to read tab or space separated data using C++):

2218

2219 RPC_channel TDC_channel mask

2220 using as formatting for each field:

2221
2222 TSCCC TCCC M

2223 TSCCC is a 5-digit integer where T is the trolley ID, s the slot ID in which the RPC is held insite
2224 the trolley T and ccc is the RPC channel number, or *strip* number, that can take values up to
2225 3-digits depending on the detector,

2226 TCCC is a 4 digit integer where T is the TDC ID, ccc is the TDC channel number that can take values
2227 in between 0 and 127, and

2228 M is a 1-digit integer indicating if the channel should be considered ($M = 1$) or discarded ($M = 0$)
2229 during analysis.

2230 This mapping and masking information is readout and stored thanks to the object `Mapping`, pre-
2231 sented in Source Code B.4. Similarly to `IniFile` objects, this class has private methods. The first
2232 one, `Mapping::CheckIfNewLine()` is used to find the newline character '`\n`' or return character
2233 '`\r`' (depending on which kind of operating system interacted with the file). This is used for the
2234 simple reason that the masking information has been introduced only during the year 2017 but the
2235 channel mapping files exist since 2015 and the very beginning of data taking at Gif++. This means
2236 that in the older data folders, before the upgrade, the channel mapping file only had 2 columns, the
2237 RPC channel and the TDC channel. For compatibility reasons, this method helps controling the
2238 character following the readout of the 2 first fields of a line. In case any end of line character is
2239 found, no mask information is present in the file and the default $M = 1$ is used. On the contrary, if
2240 the next character was a tabulation or a space, the mask information is present.

2241 Once the 3 fields have been readout, the second private method `Mapping::CheckIfTDCCh()` is
2242 used to control that the TDC channel is an existing TDC channel. Finally, the information is stored
2243 into 3 different maps (`Link`, `ReverseLink` and `Mask`) thanks to the public method `Mapping::Read()`.
2244 `Link` allows to get the RPC channel by knowing the TDC channel while `ReverseLink` does the op-
2245 posite by returning the TDC channel by knowing the RPC channel. Finally, `Mask` returns the mask
2246 associated to a given RPC channel.

```

2247 typedef map<Uint,Uint> MappingData;

2248 class Mapping {
    private:
        bool          CheckIfNewLine(char next);
        bool          CheckIfTDCCh(Uint channel);
        string         FileName;
        MappingData   Link;
        MappingData   ReverseLink;
        MappingData   Mask;
        int           Error;

    public:
        Mapping();
        Mapping(string baseName);
        ~Mapping();

        void SetFileName(const string filename);
        int Read();
        Uint GetLink(Uint tdcchannel);
        Uint GetReverse(Uint rpcchannel);
        Uint GetMask(Uint rpcchannel);
};


```

2249 *Source Code B.4: Description of C++ object Mapping used as a parser for the channel mapping and mask file.*

2250 **B.4 Description of GIF++ setup within the Offline Analysis tool**

2251 In the previous section, the tool input files have been discussed. The dimension file information is
 2252 stored in a map hosted by the `IniFile` object. But this information is then used to create a series of
 2253 new objects that helps defining the GIF++ infrastructure directly into the Offline Analysis. Indeed,
 2254 from the `RPC`, to the more general `Infrastructure`, every element of the GIF++ infrastrucutre is
 2255 recreated for each data analysis based on the information provided in input. All this information
 2256 about the infrastructure will be used to assign each hit signal to a specific strip channel of a specific
 2257 detector, and having a specific active area. This way, rate per unit area calculation is possible.
 2258

2259 **B.4.1 RPC objects**

2260 `RPC` objects have been developped to represent physical active detectors in GIF++ at the moment
 2261 of data taking. Thus, there are as many `RPC` objects created during the analysis than there were
 2262 active `RPC`s tested during a run. Each `RPC` hosts the information present in the corresponding INI
 2263 slot group, as shown in B.3, and organises it using a similar architecture. This can be seen from
 2264 `Source Code B.5`.

2265 To make the object more compact, the lists of gap labels, of gap active areas and strip active
 2266 areas are stored into `vector` dynamical containers. `RPC` objects are always contructed thanks to the
 2267 dimension file information stored into the `IniFILE` and their ID, using the format `TtSs`. Using the
 2268 `RPC` ID, the constructor calls the methods of `IniFILE` to initialise the `RPC`. The other constructors
 2269 are not used but exist in case of need. Finally, some getters have been written to access the different
 2270 private parameters storing the detector information.

```

2271
class RPC{
    private:
        string      name;           //RPC name as in webDCS database
        Uint        nGaps;          //Number of gaps in the RPC
        Uint        nPartitions;    //Number of partitions in the RPC
        Uint        nStrips;         //Number of strips per partition
        vector<string> gaps;       //List of gap labels (BOT, TOP, etc...)
        vector<float>  gapGeo;        //List of gap active areas
        vector<float>  stripGeo;      //List of strip active areas

    public:
        RPC();
        RPC(string ID, IniFile* geofile);
        RPC(const RPC& other);
        ~RPC();
        RPC& operator=(const RPC& other);

        string GetName();
        Uint GetNGaps();
        Uint GetNPartitions();
        Uint GetNStrips();
        string GetGap(Uint g);
        float GetGapGeo(Uint g);
        float GetStripGeo(Uint p);
};

2272

```

2273 *Source Code B.5: Description of C++ objects RPC that describe each active detectors used during data taking.*

2274 B.4.2 Trolley objects

2275 Trolley objects have been developped to represent physical active trolleys in GIFT++ at the moment
 2276 of data taking. Thus, there are as many trolley objects created during the analysis than there were
 2277 active trolleys hosting tested RPCs during a run. Each Trolley hosts the information present in the
 2278 corresponding INI trolley group, as shown in B.2, and organises it using a similar architecture. In
 2279 addition to the information hosted in the INI file, these object have a dynamical container of RPC
 2280 objects, representing the active detectors the active trolley was hosting at the time of data taking.
 2281 This can been seen from Source Code B.6.

2282 Trolley objects are always contructed thanks to the dimension file information stored into the
 2283 IniFILE and their ID, using the format Tt. Using the Trolley ID, the constructor calls the methods
 2284 of IniFILE to initialise the Trolley. Retrieving the information of the RPC IDs via SlotsID, a new
 2285 RPC is constructed and added to the container RPCs for each character in the ID string. The other
 2286 constructors are not used but exist in case of need. Finally, some getters have been written to access
 2287 the different private parameters storing the trolley and detectors information.

```

2288
class Trolley{
    private:
        Uint          nSlots; //Number of active RPCs in the considered trolley
        string        SlotsID; //Active RPC IDs written into a string
        vector<RPC*> RPCs;   //List of active RPCs

    public:
        //Constructors, destructor and operator =
        Trolley();
        Trolley(string ID, IniFile* geofile);
        Trolley(const Trolley& other);
        ~Trolley();
        Trolley& operator=(const Trolley& other);

        //Get GIFTrolley members
        Uint  GetNSlots();
        string GetSlotsID();
        Uint   GetSlotID(Uint s);

        //Manage RPC list
        RPC*  GetRPC(Uint r);
        void  DeleteRPC(Uint r);

        //Methods to get members of RPC objects stored in RPCs
        string GetName(Uint r);
        Uint   GetNGaps(Uint r);
        Uint   GetNPartitions(Uint r);
        Uint   GetNStrips(Uint r);
        string GetGap(Uint r, Uint g);
        float  GetGapGeo(Uint r, Uint g);
        float  GetStripGeo(Uint r, Uint p);
    };

```

Source Code B.6: Description of C++ objects `Trolley` that describe each active trolley used during data taking.

2291 B.4.3 Infrastructure object

2292 The `Infrastructure` object has been developped to represent the GIFT++ bunker area dedicated to
 2293 CMS RPC experiments. With this very specific object, all the information about the CMS RPC
 2294 setup within GIFT++ at the moment of data taking is stored. It hosts the information present in the
 2295 corresponding INI general group, as shown in B.1, and organises it using a similar architecture. In
 2296 addition to the information hosted in the INI file, this object have a dynamical container of `Trolley`
 2297 objects, representing the active tolleys in GIFT++ area. This can be seen from Source Code B.7.

2298 The `Infrastructure` object is always contructed thanks to the dimension file information stored
 2299 into the `IniFILE`. Retrieving the information of the trolley IDs via `TrolleysID`, a new `Trolley` is
 2300 constructed and added to the container `Trolleys` for each character in the ID `string`. By extension,
 2301 it is easy to understand that the process described in Section B.4.2 for the construction of RPCs
 2302 takes place when a trolley is constructed. The other constructors are not used but exist in case of
 2303 need. Finally, some getters have been written to access the different private parameters storing the
 2304 infrastructure, tolleys and detectors information.

```

2305   class Infrastructure {
2306     private:
2307       Uint           nTrolleys; //Number of active Trolleys in the run
2308       string         TrolleysID; //Active trolley IDs written into a string
2309       vector<Trolley*> Trolleys; //List of active Trolleys (struct)
2310
2311     public:
2312       //Constructors and destructor
2313       Infrastructure();
2314       Infrastructure(IniFile* geofile);
2315       Infrastructure(const Infrastructure& other);
2316       ~Infrastructure();
2317       Infrastructure& operator=(const Infrastructure& other);
2318
2319       //Get Infrastructure members
2320       Uint  GetNTrolleys();
2321       string GetTrolleysID();
2322       Uint   GetTrolleyID(Uint t);
2323
2324       //Manage Trolleys
2325       Trolley* GetTrolley(Uint t);
2326       void    DeleteTrolley(Uint t);
2327
2328       //Methods to get members of GIFTrolley objects stored in Trolleys
2329       Uint  GetNSlots(Uint t);
2330       string GetSlotsID(Uint t);
2331       Uint   GetSlotID(Uint t, Uint s);
2332       RPC*  GetRPC(Uint t, Uint r);
2333
2334       //Methods to get members of RPC objects stored in RPCs
2335       string GetName(Uint t, Uint r);
2336       Uint   GetNGaps(Uint t, Uint r);
2337       Uint   GetNPartitions(Uint t, Uint r);
2338       Uint   GetNStrips(Uint t, Uint r);
2339       string GetGap(Uint t, Uint r, Uint g);
2340       float  GetGapGeo(Uint t, Uint r, Uint g);
2341       float  GetStripGeo(Uint t, Uint r, Uint p);
2342   };

```

Source Code B.7: Description of C++ object Infrastructure that contains the full information about CMS RPC experiment in GIF++.

2308 B.5 Handeling of data

2309 As discussed in Appendix A.4.2, the raw data as a `TTree` architecture where every entry is related to
 2310 a trigger signal provided by a muon or a random pulse, whether the goal of the data taking was to
 2311 measure the performance of the detector or the noise/gamma background respectively. Each of these
 2312 entries, referred also as events, contain a more or less full list of hits in the TDC channels to which
 2313 the detectors are connected. To this list of hits corresponds a list of time stamps, marking the arrival
 2314 of the hits within the TDC channel.

2315 The infrastructure of the CMS RPC experiment within `GIF++` being defined, combining the
 2316 information about the raw data with the information provided by both the mapping/mask file and the
 2317 dimension file allows to build new physical objects that will help in computing efficiency or rates.

2318 **B.5.1 RPC hits**

2319 The raw data stored in the ROOT file as output of the GIFT++ DAQ, is readout by the analysis tool
 2320 using the structure `RAWData` presented in Source Code B.9 that differs from the structure presented
 2321 in Appendix A.4.2 as it is not meant to hold all of the data contained in the ROOT file. In this sense,
 2322 this structure is in the case of the offline analysis tool not a dynamical object and will only be storing
 2323 a single event contained in a single entry of the `TTree`.

```
2324
 2325 class RPCHit {
 2326     private:
 2327         Uint Channel;      //RPC channel according to mapping (5 digits)
 2328         Uint Trolley;      //0, 1 or 3 (1st digit of the RPC channel)
 2329         Uint Station;      //Slot where is held the RPC in Trolley (2nd digit)
 2330         Uint Strip;        //Physical RPC strip where the hit occurred (last 3
 2331             → digits)
 2332         Uint Partition;    //Readout partition along eta segmentation
 2333         float TimeStamp;   //Time stamp of the arrival in TDC
 2334
 2335     public:
 2336         //Constructors, destructor & operator =
 2337         RPCHit();
 2338         RPCHit(Uint channel, float time, Infrastructure* Infra);
 2339         RPCHit(const RPCHit& other);
 2340         ~RPCHit();
 2341         RPCHit& operator=(const RPCHit& other);
 2342
 2343         //Get RPCHit members
 2344         Uint GetChannel();
 2345         Uint GetTrolley();
 2346         Uint GetStation();
 2347         Uint GetStrip();
 2348         Uint GetPartition();
 2349         float GetTime();
 2350     };
 2351
 2352     typedef vector<RPCHit> HitList;
 2353     typedef struct GIFHitList { HitList rpc[NTROLLEYS][NSLOTS][NPARTITIONS]; } → GIFHitList;
 2354
 2355     bool SortHitbyStrip(RPCHit h1, RPCHit h2);
 2356     bool SortHitbyTime(RPCHit h1, RPCHit h2);
 2357 }
```

2326 *Source Code B.8: Description of C++ object RPCHit.*

```
2327 struct RAWData{
 2328     int iEvent;          //Event i
 2329     int TDCNHits;       //Number of hits in event i
 2330     int QFlag;          //Quality flag list (1 flag digit per TDC)
 2331     vector<Uint> *TDCCh; //List of channels giving hits per event
 2332     vector<float> *TDCTS; //List of the corresponding time stamps
 2333 }
```

2328 *Source Code B.9: Description of C++ structure RAWData.*

2329 Each member of the structure is then linked to the corresponding branch of the ROOT data tree,
 2330 as shown in the example of Source Code B.10, and using the method `GetEntry(int i)` of the ROOT
 2331 class `TTree` will update the state of the members of `RAWData`.

```

2332 TTree* dataTree = (TTree*)dataFile.Get("RAWData");
2333 RAWData data;
2334
2335 dataTree->SetBranchAddress("EventNumber", &data.iEvent);
2336 dataTree->SetBranchAddress("number_of_hits", &data.TDCNHits);
2337 dataTree->SetBranchAddress("Quality_flag", &data.QFlag);
2338 dataTree->SetBranchAddress("TDC_channel", &data.TDCCh);
2339 dataTree->SetBranchAddress("TDC_TimeStamp", &data.TDCTS);

```

2334 *Source Code B.10: Example of link in between RAWData and TTree.*

2335 The data is then analysed entry by entry and to each element of the TDC channel list, a `RPCHit` is
 2336 constructed by linking each TDC channel to the corresponding RPC channel thanks to the `Mapping`
 2337 object. The information carried by the RPC channel format allows to easily retrieve the trolley and
 2338 slot from which the hit was recorded (see section B.3.2). Using these 2 values, the readout partition
 2339 can be found by knowing the strip channel and comparing it with the number of partitions and strips
 2340 per partition stored into the `Infrastructure` object.

2341 Thus `RPCHit` objects are then stored into 3D dynamical list called `GIFHitList` (Source Code B.9)
 2342 where the 3 dimensions refer to the 3 layers of the readout in `GIF++` : in the bunker there are *trolleys*
 2343 (τ) holding detectors in *slots* (s) and each detector readout is divided into 1 or more pseudo-rapidity
 2344 *partitions* (p). Using these 3 information allows to assign an address to each readout partition and
 2345 this address will point to a specific hit list.

2346

2347 **B.5.2 Clusters of hits**

2348 All the hits contained in the ROOT file have been sorted into the different hit lists through the
 2349 `GIFHitList`. At this point, it is possible to start looking for clusters. A cluster is a group of adjacent
 2350 strips getting hits within a time window of 25 ns. These strips are then assumed to be part of the same
 2351 physical avalanche signal generated by a muon passing through the chamber or by the interaction of
 2352 a gamma stopping into the electrodes of the RPCs.

2353 To keep the cluster information, `RPCCluster` objects have been defined as shown in Source
 2354 Code B.11. Using the information of each individual `RPCHit` taken out of the hit list, it stores
 2355 the cluster size (number of adjacent strips composing the cluster), the first and last hit, the center for
 2356 spatial reconstruction and finally the start and stop time stamps as well as te time spread in between
 2357 the first and last hit.

```

2358
class RPCCluster{
    private:
        Uint ClusterSize; //Size of cluster #ID
        Uint FirstStrip; //First strip of cluster #ID
        Uint LastStrip; //Last strip of cluster #ID
        float Center; //Center of cluster #ID ((first+last)/2)
        float StartStamp; //Time stamp of the earliest hit of cluster #ID
        float StopStamp; //Time stamp of the latest hit of cluster #ID
        float TimeSpread; //Time difference between earliest and latest hits
                           //of cluster #ID

    public:
        //Constructors, destructor & operator =
        RPCCluster();
        RPCCluster(HitList List, Uint cID, Uint cSize, Uint first, Uint firstID);
        RPCCluster(const RPCCluster& other);
        ~RPCCluster();
        RPCCluster& operator=(const RPCCluster& other);

        //Get Cluster members
        Uint GetID();
        Uint GetSize();
        Uint GetFirstStrip();
        Uint GetLastStrip();
        float GetCenter();
        float GetStart();
        float GetStop();
        float GetSpread();
};

typedef vector<RPCCluster> ClusterList;

//Other functions to build cluster lists out of hit lists
void BuildClusters(HitList &cluster, ClusterList &clusterList);
void Clusterization(HitList &hits, TH1 *hcSize, TH1 *hcMult);

```

Source Code B.11: Description of C++ object cluster.

To investigate the hit list of a given detector partition, the function `Clusterization()` defined in `include/Cluster.h` needs the hits in the list to be time sorted. This is achieved by calling function `sort()` of library `<algorithm>` using the comparator `SortHitbyTime(RPCHit h1, RPCHit h2)` defined in `include/RPCHit.h` that returns `true` if the time stamp of hit `h1` is lower than that of `h2`. A first isolation of strips is made only based on time information. All the hits within the 25 ns window are taken separately from the rest. Then, this sub-list of hits is sorted this time by ascending strip number, using this time the comparator `SortHitbyStrip(RPCHit h1, RPCHit h2)`. Finally, the groups of adjacent strips are used to construct `RPCcluster` objects that are then stored in a temporary list of clusters that is at the end of the process used to know how many clusters were reconstructed and to fill their sizes into an histogram that will allows to know the mean size of muon or gamma clusters.

2373 B.6 DAQ data Analysis

All the ingredients to analyse GIF++ data have been defined. This section will focus on the different part of the analysis performed on the data, from determining the type of data the tool is dealing with

2376 to calculating the rate in each detector or reconstructing muon or gamma clusters.

2377 B.6.1 Determination of the run type

2378 In GIF++, both the performance of the detectors in detecting muons in an irradiated environment and
 2379 the gamma background can be independantly measured. These corresponds to different run types
 2380 and thus, to different TDC settings giving different data to look at.

2381

2382 In the case of performance measurements, the trigger for data taking is provided by the coïncidence
 2383 of several scintillators when muons from the beam passing through the area are detected. Data
 2384 is collected in a 600 ns wide window around the arrival of muons in the RPCs. The expected time
 2385 distribution of hits is shown in Figure B.1a. The muon peak is clearly visible in the center of the
 2386 distribution and is to be extracted from the gamma background that composes the flat part of the
 2387 distribution.

2388 On the other hand, gamma background or noise measurements are focussed on the non muon
 2389 related physics and the trigger needs to be independant from the muons to give a good measurement
 2390 of the gamma/noise distribution as seen by the detectors. The trigger is then provided by a pulse
 2391 generator at a frequency of 300 Hz whose pulse is not likely to be on time with a muon. In order
 2392 to increase the integrated time without increasing the acquisition time too much, the width of the
 2393 acquisition windows are increased to 10 μ s. The time distribution of the hits is expected to be flat, as
 2394 shown by Figure B.1b.

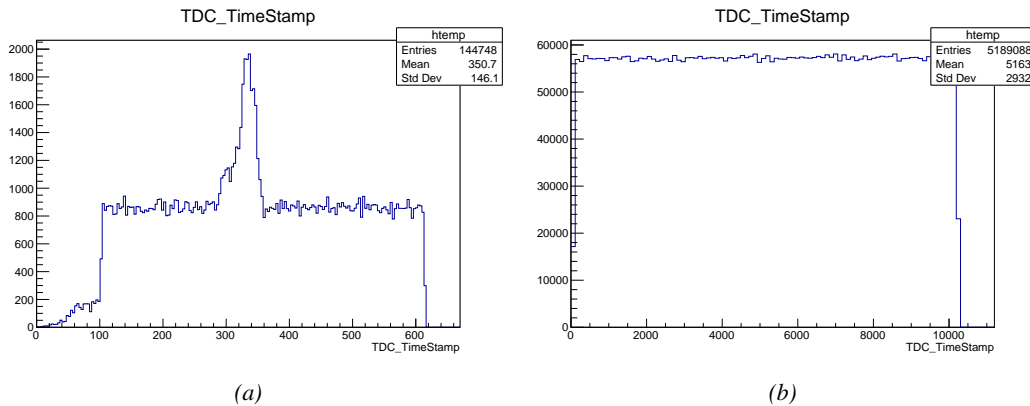


Figure B.1: Example of expected hit time distributions in the cases of efficiency (Figure B.1a) and noise/gamma rate per unit area (Figure B.1b) measurements as extracted from the raw ROOT files. The unit along the x-axis corresponds to ns. The fact that "the" muon peak is not well defined in Figure B.1a is due to the contribution of all the RPCs being tested at the same time that don't necessarily have the same signal arrival time. Each individual peak can have an offset with the ones of other detectors. The inconsistency in the first 100 ns of both time distributions is an artefact of the TDCs and are systematically rejected during the analysis.

2395 The ROOT files include a TTree called RunParameters containing, among other things, the in-
 2396 formation related to the type of run. The run type can then be accessed as described by Source
 2397 Code B.12 and the function IsEfficiencyRun() is then used to determine if the run file is an effi-
 2398 ciency run or, on the contrary, another type of run (noise or gamma measurement).

```

2399     TTree* RunParameters = (TTree*)dataFile.Get("RunParameters");
2400     TString* RunType = new TString();
2401     RunParameters->SetBranchAddress("RunType", &RunType);
2402     RunParameters->GetEntry(0);

```

2401 *Source Code B.12: Access to the run type contained in TTree* RunParameters.*

2402 Finally, the data files will have a slightly different content whether it was collected before or after
 2403 October 2017 and the upgrade of the DAQ software that brought a new information into the ROOT
 2404 output. This is discussed in Appendix A.4.3 and implies that the analysis will differ a little depending
 2405 on the data format. Indeed, as no information on the data quality is stored, in older data files, the cor-
 2406 rections for missing events has to be done at the end of the analysis. The information about the type
 2407 of data format is stored in the variable **bool** `isNewFormat` by checking the list of branches contained
 2408 in the data tree via the methods `TTree::GetListOfBranches()` and `TCollection::Contains()`.

2409 **B.6.2 Beam time window calculation for efficiency runs**

2410 Knowing the run type is important first of all to know the width of the acquisition window to be used
 2411 for the rate calculation and finally to be able to seek for muons. Indeed, the peak that appears in the
 2412 time distribution for each detectors is then fitted to extract the most probable time window in which
 2413 the tool should look for muon hits. The data outside of this time window is then used to evaluate the
 2414 noise or gamma background the detector was subjected to during the data taking. Computing the
 2415 position of the peak is done calling the function `SetBeamWindow()` defined in file `src/RPCHit.cc` that
 2416 loops a first time on the data. The data is first sorted in a 3D array of 1D histograms (`GIFH1Array`, see
 2417 `include/types.h`). Then the location of the highest bin is determined using `TH1::GetMaximumBin()`
 2418 and is used to define a window in which a gaussian fit will be applied to compute the peak width.
 2419 This window is a 80 ns defined by Formula B.1 around the central bin.

$$t_{center}(ns) = bin \times width_{bin}(ns) \quad (\text{B.1a})$$

$$[t_{low}; t_{high}] = [t_{center} - 40; t_{center} + 40] \quad (\text{B.1b})$$

2420 Before the fit is performed, the average number of noise/gamma hits per bin is evaluated using
 2421 the data outside of the fit window. Excluding the first 100 ns, the average number of hits per bin
 2422 due to the noise or gamma is defined by Formula B.2 after extracting the amount of hits in the time
 2423 windows $[100; t_{low}]$ and $[t_{high}; 600]$ thanks to the method `TH1::Integral()`. This average number
 2424 of hits is then subtracted to every bin of the 1D histogram, in order to *clean* it from the noise or
 2425 gamma contribution as much as possible to improve the fit quality. Bins where $\langle n_{hits} \rangle$ is greater
 2426 than the actual bin content are set to 0.

$$\Delta t_{noise}(ns) = 600 \overbrace{-t_{high} + t_{low}}^{-80ns} - 100 = 420ns \quad (\text{B.2a})$$

$$\langle n_{hits} \rangle = width_{bin}(ns) \times \frac{\sum_{t=100}^{t_{low}} + \sum_{t=t_{high}}^{600}}{\Delta t_{noise}(ns)} \quad (\text{B.2b})$$

2427 Finally, the fit parameters are extracted and saved for each detector in 3D arrays of **float**
 2428 (`muonPeak`, see `include/types.h`), a first one for the mean arrival time of the muons, `PeakTime`,

2429 and a second one for the width of the peak, `PeakWidth`. The width is defined as 6σ of the gaussian
 2430 fit. The same settings are applied to every partitions of the same detector. To determine which one
 2431 of the detector's partitions is directly illuminated by the beam, the peak height of each partition is
 2432 compared and the highest one is then used to define the peak settings.

2433 B.6.3 Data loop and histogram filling

2434 3D arrays of histogram are created to store the data and display it on the DQM of G4F++ webDCS
 2435 for the use of shifters. These histograms, presented in section B.2.1.1, are filled while looping on
 2436 the data. Before starting the analysis loop, it is necessary to control the entry quality for the new
 2437 file formats featuring `QFlag`. If the `QFlag` value for this entry shows that 1 TDC or more have a
 2438 `CORRUPTED` flag, then this event is discarded. The loss of statistics is low enough to be neglected.
 2439 `QFlag` is controlled using the function `IsCorruptedEvent()` defined in `src/utils.cc`. As explained
 2440 in Appendix A.4.3, each digit of this integer represents a TDC flag that can be 1 or 2. Each 2 is
 2441 the sign of a `CORRUPTED` state. Then, the data is accessed entry by entry in the ROOT `TTree` using
 2442 `RAWData` and each hit in the hit list is assigned to a detector channel and saved in the corresponding
 2443 histograms. In the first part of the analysis, in which the loop over the ROOT file's content is
 2444 performed, the different steps are:

2445 **1- RPC channel assignment and control:** a check is done on the RPC channel extracted thanks
 2446 to the mapping via the method `Mapping::GetLink()`. If the channel is not initialised and is 0, or if
 2447 the TDC channel was greater than 5127, the hit is discarded. This means there was a problem in the
 2448 mapping. Often a mapping problem leads to the crash of the offline tool.

2449 **2- Creation of a `RPCHit` object:** to easily get the trolley, slot and partition in which the hit has
 2450 been assigned, this object is particularly helpful.

2451 **3- General histograms are filled:** the hit is filled into the time distribution and the general hit
 2452 distribution histograms, and if the arrival time is within the first 100 ns, it is discarded and nothing
 2453 else happens and the loop proceeds with the next hit in the list.

2454 **4- Multiplicity counter:** the hit multiplicity counter of the corresponding detectors incremented.

2455 **5-a- Efficiency runs - Is the hit within the peak window? :** if the peak is contained in the peak
 2456 window previously defined in section B.6.2, the hit is filled into the beam hit profile histogram of
 2457 the corresponding chamber, added into the list of muon hits and increments the counter of *in time*
 2458 hits. The term *in time* here refers to the hits that are likely to be muons by arriving in the expected
 2459 time window. If the hit is outside of the peak window, it is filled into the noise profile histogram
 2460 of the corresponding detector, added into the list of noise/gamma hits and increments the counter of
 2461 noise/gamma hits.

2462 **5-b- Noise/gamma rate runs - Noise histograms are filled:** the hit is filled into the noise profile
 2463 histogram of the corresponding detector, added into the list of noise/gamma hits and increments the
 2464 counter of noise/gamma hits.

2465

2466 After the loop on the hit list of the entry is over, the next step is to clusterize the 3D lists filled
 2467 in the previous steps. A 3D loop is then started over the active trolley, slot and RPC partitions to
 2468 access these objects. Each `NoiseHitList` and `MuonHitList`, in case of efficiency run, are clusterized
 2469 as described in section B.5.2. There corresponding cluster size and multiplicity histograms are filled
 2470 at the end of the clustering process. Then, the efficiency histogram is filled in case of efficiency run.
 2471 The selection is simply made by checking whether the RPC detected signals in the peak window
 2472 during this event. Nevertheless, it is useful to highlight that at this level, it is not possible yet to
 2473 discriminate in between a muon hit and noise or gamma hit. Thus, `MuonCSize_H`, `MuonCMult_H`
 2474 and `Efficiency0_H` are subjected to noise and gamma contamination. This contamination will be
 2475 estimated and corrected at the moment the results will be written into output CSV files. Finally, the
 2476 loop ends on the filling of the general hit multiplicity histogram.

2477 **B.6.4 Results calculation**

2478 As mentioned in section B.2.1, the analysis of DAQ data provides the user with 3 CSV files and
 2479 a ROOT file associated to each and every ROOT data file. The fourth CSV file is provided by the
 2480 extraction of the CEAN main frame data monitored during data taking and will be discussed later.
 2481 After looping on the data in the previous part of the analysis macro, the output files are created and a
 2482 3D loop on each RPC readout partitions is started to extract the histograms parameters and compute
 2483 the final results.

2484

2485 **B.6.4.1 Rate normalisation**

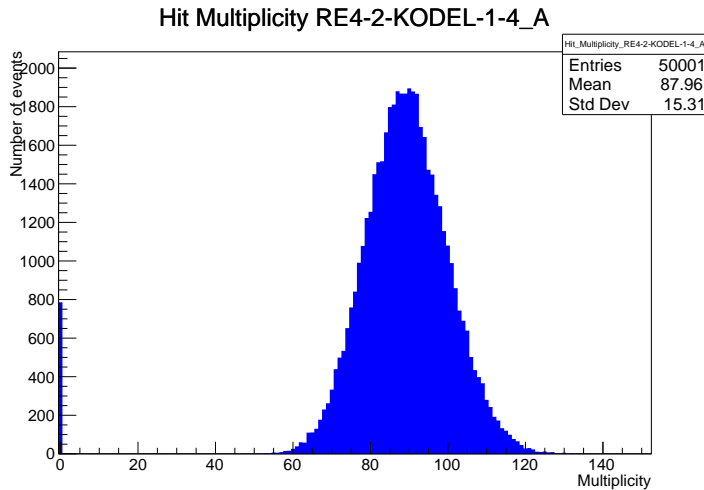


Figure B.2: The effect of the quality flag is explained by presenting the reconstructed hit multiplicity of a data file without `Quality_flag`. The artificial high content of bin 0 is the effect of corrupted data.

2486 To analyse old data format files, not containing any quality flag, it is needed to estimate the amount
 2487 of corrupted data via a fit as the corrupted data will always fill events with a fake "0 multiplicity".
 2488 Indeed, as no hits were stored in the DAQ ROOT files, these events artificially contribute to fill
 2489 the bin corresponding to a null multiplicity, as shown in Figure B.2. In the case the mean of the

hit multiplicity distribution is high, the contribution of the corrupted data can easily be evaluated for later correction by comparing the level of the bin at multiplicity 0 and of a skew fit curve that should indicate a value consistent with 0. A skew fit has been chosen over a Poisson fit as it was giving better results for lower mean multiplicity values. Nevertheless, for low irradiation cases, as explained in Appendix A.4.3, the hit multiplicity distribution mean is, on the contrary, rather small and the probability to record events without hits can't be considered small anymore, leading to a difficult and non-reliable estimation of the corruption. As can be seen in Source Code B.13, conditions have been applied to prevent bad fits and wrong corruption estimation in cases where :

- The difference in between the data for multiplicity 1 and the corresponding fit value should be lower than 1% of the total amount of data : $\frac{|n_{m=1} - sk(1)|}{N_{tot}} < 0.01$ where $n_{m=1}$ is the number of entries with multiplicity 1, $sk(1)$ the value of the skew fit, as defined by Formula 4.3, for multiplicity 1 and N_{tot} the total number of entries.

- The amount of data contained in the multiplicity 0 bin should not exceed 40% : $\frac{n_{m=0}}{N_{tot}} \leq 0.4$ where $n_{m=0}$ is the number of entries with multiplicity 0. This number has been determined to be the maximum to be able to separate the excess of data due to corruption from the hit multiplicity distribution.

Those 2 conditions need to be fulfilled to estimate the corruption of old data format files. If the fit was successful, the level of corruption is written in `Offline-Corrupted.csv` and the number of corrupted entries, refered as the integer `nEmptyEvent`, is subtracted from the total number of entries when the rate normalisation factor is computed as explicit in Source Code B.13. Note that for new data format files, the number of corrupted entries being set to 0, the definition of `rate_norm` stays valid.

```

2512
if(!isNewFormat){
    TF1* GaussFit = new TF1("gaussfit","[0]*exp(-0.5*((x-[1])/[2])**2)",0,Xmax);
    GaussFit->SetParameter(0,100);
    GaussFit->SetParameter(1,10);
    GaussFit->SetParameter(2,1);
    HitMultiplicity_H.rpc[T][S][p]->Fit(GaussFit,"LIQR","",0.5,Xmax);

    TF1* SkewFit = new TF1("skewfit","[0]*exp(-0.5*((x-[1])/[2])**2) / (1 +
→ exp(-[3]*(x-[4])))",0,Xmax);
    SkewFit->SetParameter(0,GaussFit->GetParameter(0));
    SkewFit->SetParameter(1,GaussFit->GetParameter(1));
    SkewFit->SetParameter(2,GaussFit->GetParameter(2));
    SkewFit->SetParameter(3,1);
    SkewFit->SetParameter(4,1);
    HitMultiplicity_H.rpc[T][S][p]->Fit(SkewFit,"LIQR","",0.5,Xmax);

    double fitValue = SkewFit->Eval(1,0,0,0);
    double dataValue = (double)HitMultiplicity_H.rpc[T][S][p]->GetBinContent(2);
    double difference = TMath::Abs(dataValue - fitValue);
    double fitTOdataVSentries_ratio = difference / (double)nEntries;
    bool isFitGOOD = fitTOdataVSentries_ratio < 0.01;

2513
    double nSinglehit = (double)HitMultiplicity_H.rpc[T][S][p]->GetBinContent(1);
    double lowMultRatio = nSinglehit / (double)nEntries;
    bool isMultLOW = lowMultRatio > 0.4;

    if(isFitGOOD && !isMultLOW){
        nEmptyEvent = HitMultiplicity_H.rpc[T][S][p]->GetBinContent(1);
        nPhysics = (int)SkewFit->Eval(0,0,0,0);
        if(nPhysics < nEmptyEvent)
            nEmptyEvent = nEmptyEvent-nPhysics;
    }
}

double corrupt_ratio = 100.*(double)nEmptyEvent / (double)nEntries;
outputCorrCSV << corrupt_ratio << '\t';

float rate_norm = 0.;
float stripArea = GIFIInfra->GetStripGeo(tr,sl,p);

if(IsEfficiencyRun(RunType)){
    float noiseWindow = BMTDCWINDOW - TIMEREJECT - 2*PeakWidth.rpc[T][S][p];
    rate_norm = (nEntries-nEmptyEvent)*noiseWindow*1e-9*stripArea;
} else
    rate_norm = (nEntries-nEmptyEvent)*RDMNOISEWDW*1e-9*stripArea;

```

Source Code B.13: Definition of the rate normalisation variable. It takes into account the number of non corrupted entries and the time window used for noise calculation, to estimate the total integrated time, and the strip active area to express the result as rate per unit area.

2515 B.6.4.2 Rate and activity

2516 At this point, the strip rate histograms, StripNoiseProfile_H.rpc[T][S][p], only contain an in-
2517 formation about the total number of noise or rate hits each channel received during the data taking.
2518 As described in Source Code B.14, a loop on the strip channels will be used to normalise the content
2519 of the rate distribution histogram for each detector partitions. The initial number of hits recorded for
2520 a given bin will be extracted and 2 values will be computed:

- 2521 ● the strip rate, defined as the number of hits recorded in the bin normalised like described in
 2522 the previous section, using the variable `rate_norm`, and

- 2523 ● the strip activity, defined as the number of hits recorded in the bin normalised to the average
 2524 number of hits per bin contained in the partition histogram, using the variable `averageNhit`.
 2525 This value provides an information on the homogeneity of the detector response to the gamma
 2526 background or of the detector noise. An activity of 1 corresponds to an average response.
 2527 Above 1, the channel is more active than the average and bellow 1, the channel is less active.

```

int nNoise = StripNoiseProfile_H.rpc[T][S][p]->GetEntries();
float averageNhit = (nNoise>0) ? (float)(nNoise/nStripsPart) : 1.;

for(Uint st = 1; st <= nStripsPart; st++){
    float stripRate =
        StripNoiseProfile_H.rpc[T][S][p]->GetBinContent(st)/rate_norm;
    float stripAct =
        StripNoiseProfile_H.rpc[T][S][p]->GetBinContent(st)/averageNhit;

    StripNoiseProfile_H.rpc[T][S][p]->SetBinContent(st,stripRate);
    StripActivity_H.rpc[T][S][p]->SetBinContent(st,stripAct);
}

```

2529 *Source Code B.14: Description of the loop that allows to set the content of each strip rate and strip activity
 channel for each detector partition.*

2530 On each detector partitions, which are readout by a single FEE, all the channels are not processed
 2531 by the same chip. Each chip can give a different noise response and thus, histograms using a chip
 2532 binning are used to investigate chip related noise behaviours. The average values of the strip rate
 2533 or activity grouped into a given chip are extracted using the using the function `GetChipBin()` and
 2534 stored in dedicated histograms as described in Source Codes B.15 and B.16 respectively.

```

float GetChipBin(TH1* H, Uint chip){
    Uint start = 1 + chip*NSTRIPSCHIP;
    int nActive = NSTRIPSCHIP;
    float mean = 0.;

    for(Uint b = start; b <= (chip+1)*NSTRIPSCHIP; b++){
        float value = H->GetBinContent(b);
        mean += value;
        if(value == 0.) nActive--;
    }

    if(nActive != 0) mean /= (float)nActive;
    else mean = 0.;

    return mean;
}

```

2537 *Source Code B.15: Function used to compute the content of a bin for an histogram using chip binning.*

```

2538     for(UInt ch = 0; ch < (nStripsPart/NSTRIPSCHIP); ch++) {
2539         ChipMeanNoiseProf_H.rpc[T][S][p]->
2540             SetBinContent(ch+1,GetChipBin(StripNoiseProfile_H.rpc[T][S][p],ch));
2541         ChipActivity_H.rpc[T][S][p]->
2542             SetBinContent(ch+1,GetChipBin(StripActivity_H.rpc[T][S][p],ch));
2543     }

```

Source Code B.16: Description of the loop that allows to set the content of each chip rate and chip activity bins for each detector partition knowing the information contained in the corresponding strip distribution histograms.

The activity variable is used to evaluate the homogeneity of the detector response to background or of the detector noise. The homogeneity h_p of each detector partition can be evaluated using the formula $h_p = \exp(-\sigma_p^R / \langle R \rangle_p)$, where $\langle R \rangle_p$ is the partition mean rate and σ_p^R is the rate standard deviation calculated over the partition channels. The more homogeneously the rates are distributed and the smaller will σ_p^R be, and the closer to 1 will h_p get. On the contrary, if the standard deviation of the channel's rates is large, h_p will rapidly get to 0. This value is saved into histograms as shown in Source Code B.17 and could in the future be used to monitor through time, once extracted, the evolution of every partition homogeneity. This could be of great help to understand the apparition of eventual hot spots due to ageing of the chambers subjected to high radiation levels. The monitored homogeneity information could then be combined with a monitoring of the activity of each individual channel in order to have a finer information. Monitoring tools have been suggested and need to be developed for this purpose.

```

2552     float MeanPartSDev = GetTH1StdDev(StripNoiseProfile_H.rpc[T][S][p]);
2553     float strip_homog = (MeanPartRate==0)
2554         ? 0.
2555         : exp(-MeanPartSDev/MeanPartRate);
2556     StripHomogeneity_H.rpc[T][S][p]->Fill("exp -#left(#frac{\#sigma_{Strip}
2557         \rightarrow Rate}{\#mu_{Strip Rate}}\#right)",strip_homog);
2558     StripHomogeneity_H.rpc[T][S][p]->GetYaxis()->SetRangeUser(0.,1.);
2559
2560     float ChipStDevMean = GetTH1StdDev(ChipMeanNoiseProf_H.rpc[T][S][p]);
2561     float chip_homog = (MeanPartRate==0)
2562         ? 0.
2563         : exp(-ChipStDevMean/MeanPartRate);
2564     ChipHomogeneity_H.rpc[T][S][p]->Fill("exp -#left(#frac{\#sigma_{Chip}
2565         \rightarrow Rate}{\#mu_{Chip Rate}}\#right)",chip_homog);
2566     ChipHomogeneity_H.rpc[T][S][p]->GetYaxis()->SetRangeUser(0.,1.);

```

Source Code B.17: Storage of the homogeneity into dedicated histograms.

B.6.4.3 Strip masking tool

The offline tool is automatically called at the end of each data taking to analyse the data and offer the shifter DQM histograms to control the data quality. After the histograms have been published online in the DQM page, the shifter can decide to mask noisy or dead channels that will contribute to bias the final rate calculation by editing the mask column of `ChannelsMapping.csv` as can be seen in Figure B.3.

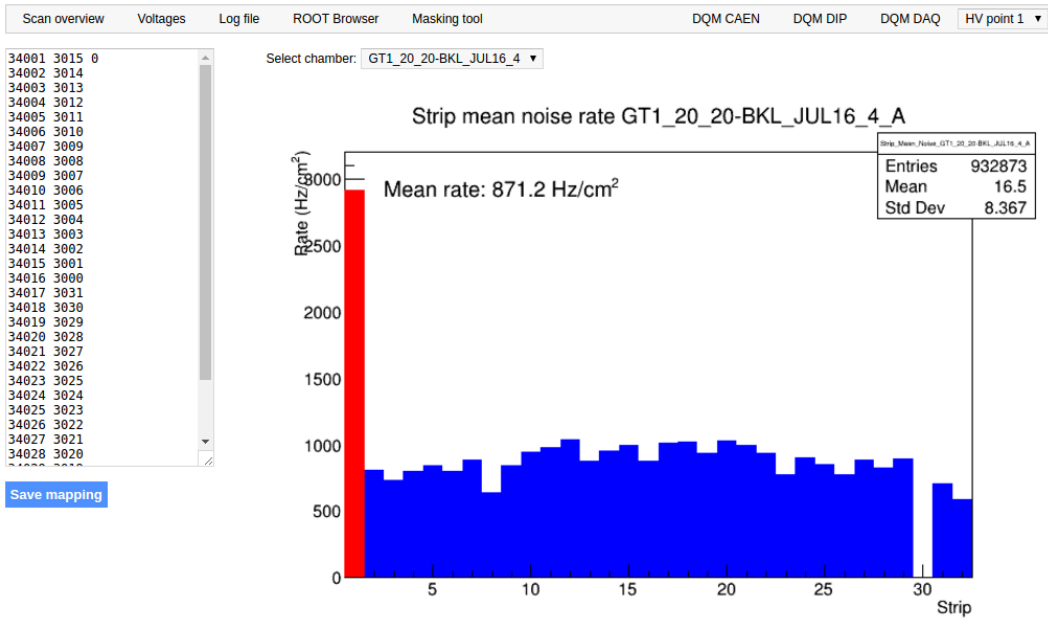


Figure B.3: Display of the masking tool page on the webDCS. The window on the left allows the shifter to edit ChannelsMapping.csv. To mask a channel, it only is needed to set the 3rd field corresponding to the strip to mask to 0. It is not necessary for older mapping file formats to add a 1 for each strip that is not masked as the code is versatile and the default behaviour is to consider missing mask fields as active strips. The effect of the mask is directly visible for noisy channels as the corresponding bin turns red. The global effect of masking strips will be an update of the rate value showed on the histogram that will take into consideration the rejected channels.

From the code point of view, the function `GetTH1Mean()` is used to retrieve the mean rate partition by partition after the rates have been calculated strip by strip and filled into the histograms `StripNoiseProfile_H.rpc[T][S][p]`, as described through Source Code B.18.

Once the mask for each rejected channel has been updated, the shifter can manually run the offline tool again to update the DQM plots, now including the masked strips, as well the rate results written in the output CSV file `Offline-Rate.csv`. If not done during the shifts, the strip masking procedure needs to be carefully done by the person in charge of data analysis on the scans that were selected to produce the final results.

```

2569 float GetTH1Mean(TH1* H) {
2570     int nBins = H->GetNbinsX();
2571     int nActive = nBins;
2572     float mean = 0.;

        for(int b = 1; b <= nBins; b++) {
            float value = H->GetBinContent(b);
            mean += value;
            if(value == 0.) nActive--;
        }

        if(nActive != 0) mean /= (float)nActive;
        else mean = 0.;

        return mean;
}

```

Source Code B.18: The function `GetTH1Mean()` is used to return the mean along the y-axis of `TH1` histograms containing rate information. In order to take into account masked strips whose rate is set to 0, the function looks for masked channels and decrement the number of active channels for each null value found.

2572 B.6.4.4 Output CSV files filling

2573 All the histograms have been filled. Parameters will then be extracted from them to compute the
2574 final results that will later be used to produce plots. Once the results have been computed, the very
2575 last step of the offline macro is to write these values into the corresponding CSV outputs. Aside of
2576 the file `Offline-Corrupted.csv`, 2 CSV files are being written by the macro `offlineAnalysis()`,
2577 `Offline-Rates.csv` and `Offline-L0-EffCl.csv` that respectively contain information about noise
2578 or gamma rates, cluster size and multiplicity, and about level 0 reconstruction of the detector effi-
2579 ciency, muon cluster size and multiplicity. Details on the computation and file writing are respec-
2580 tively given in Sources Codes B.19 and B.20.

2581 **Noise/gamma background variables** are computed and written in the output file for each detector
2582 partitions. A detector average of the hit and cluster rate is also provided, as shown through Sources
2583 Code B.19. The variables that are written for each partition are:

- 2584 • The mean partition hit rate per unit area, `MeanPartRate`, that is extracted from the histogram
2585 `StripNoiseProfile_H` as the mean value along the y-axis, as described in section B.6.4.3. No
2586 error is recorded for the hit rate as this is considered a single measurement. No statistical error
2587 can be associated to it and the systematics are unknown.
- 2588 • The mean cluster size, `cSizePart`, is extracted from the histogram `NoiseCSize_H` and it's
2589 statistical error, `cSizePartErr`, is taken to be 2σ of the total distribution.
- 2590 • The mean cluster multiplicity per trigger, `cMultPart`, is extracted from the histogram `NoiseCMult_H`
2591 and it's statistical error, `cMultPartErr`, is taken to be 2σ of the total distribution. It is impor-
2592 tant to point to the fact that this variable gives an information that is dependent on the buffer
2593 window width used for each trigger for the calculation.
- 2594 • The mean cluster rate per unit area, `ClustPartRate`, is defined as the mean hit rate normalised

2595 to the mean cluster size and it's statistical error, `ClustPartRateErr`, is then obtained using the
 2596 relative statistical error on the mean cluster size.

```

for (UInt tr = 0; tr < GIFInfra->GetNTrolleys(); tr++) {
    UInt T = GIFInfra->GetTrolleyID(tr);

    for (UInt sl = 0; sl < GIFInfra->GetNSlots(tr); sl++) {
        UInt S = GIFInfra->GetSlotID(tr,sl) - 1;

        float MeanNoiseRate = 0.;
        float ClusterRate = 0.;
        float ClusterSDev = 0.;

        for (UInt p = 0; p < GIFInfra->GetNPartitions(tr,sl); p++) {
            float MeanPartRate = GetTH1Mean(StripNoiseProfile_H.rpc[T][S][p]);
            float cSizePart = NoiseCSIZE_H.rpc[T][S][p]->GetMean();
            float cSizePartErr = (NoiseCSIZE_H.rpc[T][S][p]->GetEntries()==0)
                ? 0.
                : 2*NoiseCSIZE_H.rpc[T][S][p]->GetStdDev() /
                    sqrt(NoiseCSIZE_H.rpc[T][S][p]->GetEntries());
            float cMultPart = NoiseCMult_H.rpc[T][S][p]->GetMean();
            float cMultPartErr = (NoiseCMult_H.rpc[T][S][p]->GetEntries()==0)
                ? 0.
                : 2*NoiseCMult_H.rpc[T][S][p]->GetStdDev() /
                    sqrt(NoiseCMult_H.rpc[T][S][p]->GetEntries());
            float ClustPartRate = (cSizePart==0) ? 0.
                : MeanPartRate/cSizePart;
            float ClustPartRateErr = (cSizePart==0) ? 0.
                : ClustPartRate * cSizePartErr/cSizePart;

            outputRateCSV << MeanPartRate << '\t'
                << cSizePart << '\t' << cSizePartErr << '\t'
                << cMultPart << '\t' << cMultPartErr << '\t'
                << ClustPartRate << '\t' << ClustPartRateErr << '\t';

            RPCarea += stripArea * nStripsPart;
            MeanNoiseRate += MeanPartRate * stripArea * nStripsPart;
            ClusterRate += ClustPartRate * stripArea * nStripsPart;
            ClusterSDev += (cSizePart==0)
                ? 0.
                : ClusterRate*cSizePartErr/cSizePart;
        }

        MeanNoiseRate /= RPCarea;
        ClusterRate /= RPCarea;
        ClusterSDev /= RPCarea;

        outputRateCSV << MeanNoiseRate << '\t'
            << ClusterRate << '\t' << ClusterSDev << '\t';
    }
}

```

Source Code B.19: Description of rate result calculation and writing into the CSV output `Offline-Rate.csv`. Are saved into the file for each detector, the mean partition rate, cluster size and cluster mutiplicity, along with their errors, for each partition and as well as a detector average.

2599 **Muon performance variables** are computed and written in the output file for each detector partitions as shown through Sources Code B.20. The variables that are written for each partition are:

- 2601 ● The muon efficiency, `eff`, extracted from the histogram `Efficiency0_H`. It is reminded that
2602 this offline tool doesn't include any tracking algorithm to identify muons from the beam and
2603 only relies on the hits arriving in the time window corresponding to the beam time. The con-
2604 tent of the efficiency histogram is thus biased by the noise/gamma background contribution
2605 into this window and is thus corrected by estimating the muon data content in the peak re-
2606 gion knowing the noise/gamma content in the rate calculation region. Both time windows
2607 being different, the choice was made to normalise the noise/gamma background calculation
2608 window to it's equivalent beam window in order to have comparable values using the variable
2609 `windowRatio`. Finally, to estimate the data ratio in the peak region, the variable `DataRatio`
2610 is defined as the ratio in between the estimated mean cluster multiplicity of the muons in the
2611 peak region, `MuonCM`, and of the total mean cluster multiplicity in the peak region, `PeakCM`.
2612 `MuonCM` is itself defined as the difference in between the total mean cluster multiplicity in the
2613 peak region and the normalised mean noise/gamma cluster multiplicity calculated outside of
2614 the peak region. The statistical error related to the efficiency, `eff_err`, is computed using a
2615 binomial distribution, as the efficiency measure the probability of "success" and "failure" to
2616 detect muons.
- 2617 ● The mean muon cluster size, `MuonCS`, is calculated using the total mean cluster size and multi-
2618 plicity in the peak region, respectively extracted from histograms `MuonCSize_H` and `MuonCMult_H`,
2619 the noise/gamma background mean cluster size and normalised multiplicity, extracted from
2620 `NoiseCSize_H` and `NoiseCMult_H`, and of the estimated muon cluster multiplicity `MuonCM` pre-
2621 viously explicated. The associated statistical error, `MuonCM_err`, is calculated using the propa-
2622 gation of errors of the mentioned variables.
- 2623 ● The mean muon cluster multiplicity in the peak region, `MuonCM`, explicated above whose sta-
2624 tistical error, `MuonCM_err`, is the sum of statistical error associated to the total mean clus-
2625 ter multiplicity in the peak reagion, `PeakCM_err`, and of the mean noise/gamma cluster size,
2626 `NoiseCM_err`.

2627 In addition to these 2 CSV files, the histograms are saved in ROOT file `Scan00XXXX_HVY_Offline.root`
2628 as explained in section B.2.1.1.

2629

```

for (UInt tr = 0; tr < GIFInfra->GetNTrolleys(); tr++) {
    UInt T = GIFInfra->GetTrolleyID(tr);
    for (UInt sl = 0; sl < GIFInfra->GetNSlots(tr); sl++) {
        UInt S = GIFInfra->GetSlotID(tr,sl) - 1;
        for (UInt p = 0; p < GIFInfra->GetNPartitions(tr,sl); p++) {
            float noiseWindow =
                BMTDCWINDOW - TIMEREJECT - 2*PeakWidth.rpc[T][S][p];
            float peakWindow = 2*PeakWidth.rpc[T][S][p];
            float windowRatio = peakWindow/noiseWindow;

            float PeakCM = MuonCMult_H.rpc[T][S][p]->GetMean();
            float PeakCS = MuonCSize_H.rpc[T][S][p]->GetMean();
            float NoiseCM = NoiseCMult_H.rpc[T][S][p]->GetMean() *windowRatio;
            float NoiseCS = NoiseCSize_H.rpc[T][S][p]->GetMean();
            float MuonCM = (PeakCM<NoiseCM) ? 0. : PeakCM-NoiseCM;
            float MuonCS = (MuonCM==0 || PeakCM*PeakCS<NoiseCM*NoiseCS)
                ? 0.
                : (PeakCM*PeakCS-NoiseCM*NoiseCS) / MuonCM;
            float PeakCM_err = (MuonCMult_H.rpc[T][S][p]->GetEntries()==0.)
                ? 0.
                : 2*MuonCMult_H.rpc[T][S][p]->GetStdDev() /
                    sqrt(MuonCMult_H.rpc[T][S][p]->GetEntries());
            float PeakCS_err = (MuonCSize_H.rpc[T][S][p]->GetEntries()==0.)
                ? 0.
                : 2*MuonCSize_H.rpc[T][S][p]->GetStdDev() /
                    sqrt(MuonCSize_H.rpc[T][S][p]->GetEntries());
            float NoiseCM_err = (NoiseCMult_H.rpc[T][S][p]->GetEntries()==0.)
                ? 0.
                : windowRatio*2*NoiseCMult_H.rpc[T][S][p]->GetStdDev() /
                    sqrt(NoiseCMult_H.rpc[T][S][p]->GetEntries());
            float NoiseCS_err = (NoiseCSize_H.rpc[T][S][p]->GetEntries()==0.)
                ? 0.
                : 2*NoiseCSize_H.rpc[T][S][p]->GetStdDev() /
                    sqrt(NoiseCSize_H.rpc[T][S][p]->GetEntries());
            float MuonCM_err = (MuonCM==0) ? 0. : PeakCM_err+NoiseCM_err;
            float MuonCS_err = (MuonCS==0 || MuonCM==0) ? 0.
                : (PeakCS*PeakCM_err + PeakCM*PeakCS_err +
                    NoiseCS*NoiseCM_err + NoiseCM*NoiseCS_err +
                    MuonCS*MuonCM_err) / MuonCM;

            float DataRatio = MuonCM/PeakCM;
            float DataRatio_err = (MuonCM==0) ? 0.
                : DataRatio*(MuonCM_err/MuonCM + PeakCM_err/PeakCM);
            float eff = DataRatio*Efficiency0_H.rpc[T][S][p]->GetMean();
            float eff_err = DataRatio*2*Efficiency0_H.rpc[T][S][p]->GetStdDev() /
                sqrt(Efficiency0_H.rpc[T][S][p]->GetEntries()) +
                Efficiency0_H.rpc[T][S][p]->GetMean()*DataRatio_err;

            outputEffCSV << eff << '\t' << eff_err << '\t'
                << MuonCS << '\t' << MuonCS_err << '\t'
                << MuonCM << '\t' << MuonCM_err << '\t';
        }
    }
}

```

2630

Source Code B.20: Description of efficiency result calculation and writing into the CSV output Offline-L0-EffCl.csv. Are saved into the file for each detector, the efficiency, corrected taking into account the background in the peak window of the time profile, muon cluster size and muon cluster multiplicity, along with their errors, for each partition and as well as a detector average.

2631

B.7 Current data Analysis

Detectors under test at GIF++ are connected both to a CAEN HV power supply and to a CAEN ADC that reads the currents inside of the RPC gaps bypassing the supply cable. During data taking, the webDCS records into a ROOT file called `Scan00XXXX_HVY_CAEN.root` histograms with the monitored parameters of both CAEN devices. Are recorded for each RPC channels (in most cases, a channel corresponds to an RPC gap):

- the effective voltage, HV_{eff} , set by the webDCS using the PT correction on the CAEN power supply,
- the applied voltage, HV_{app} , monitored by the CAEN power supply, and the statistical error related to the variations of this value through time to follow the variation of the environmental parameters defined as the RMS of the histogram divided by the square root of the number of recorded points,
- the monitored current, I_{mon} , monitored by the CAEN power supply, and the statistical error related to the variations of this value through time to follow the variation of the environmental parameters defined as the RMS of the histogram divided by the square root of the number of recorded points,
- the corresponding current density, J_{mon} , defined as the monitored current per unit area, $J_{mon} = I_{mon}/A$, where A is the active area of the corresponding gap,
- the ADC current, I_{ADC} , recorded through the CAEN ADC module that monitors the dark current in the gap itself. First of all, the resolution of such a module is better than that of CAEN power supplies and moreover, the current is not read-out through the HV supply line but directly at the chamber level giving the real current inside of the detector. The statistical error is defined as the RMS of the histogram distribution divided by the square root of the number of recorded points.

Once extracted through a loop over the element of GIF++ infrastructure via the C++ macro `GetCurrent()`, these parameters, organised in 9 columns per detector HV supply line, are written in the output CSV file `Offline-Current.csv`. The macro can be found in the file `Current.cc`.

References

- [1] T. Massam et al. “Experimental observation of antideuteron production”. In: *Il Nuovo Cimento A* 63 (1965), pp. 10–14.
- [2] UA1 Collaboration. “Experimental observation of isolated large transverse energy electrons with associated missing energy at $s = 540 \text{ GeV}$ ”. In: *Physics Letters B* 122 (1983), pp. 103–116.
- [3] UA2 Collaboration. “Observation of single isolated electrons of high transverse momentum in events with missing transverse energy at the CERN pp collider”. In: *Physics Letters B* 122 (1983), pp. 476–485.
- [4] UA1 Collaboration. “Experimental observation of lepton pairs of invariant mass around $95 \text{ GeV}/c^2$ at the CERN SPS collider”. In: *Physics Letters B* 126 (1983), pp. 398–410.
- [5] UA2 Collaboration. “Evidence for $Z_0 \rightarrow e^+e^-$ at the CERN pp collider”. In: *Physics Letters B* 129 (1983), pp. 130–140.
- [6] ALEPH Collaboration. “Determination of the number of light neutrino species”. In: *Physics Letters B* 231 (1989), pp. 519–529.
- [7] CERN, ed. (1985).
- [8] CERN, ed. (1986).
- [9] CERN, ed. (1994).
- [10] CERN, ed. (1998).
- [11] CERN, ed. (1999).
- [12] CERN. Geneva. LHC Experiments Committee. *Letter of Intent for A Large Ion Collider Experiment [ALICE]*, note = CERN-LHCC-93-016. Tech. rep. ALICE Collaboration, 1993.
- [13] CERN. Geneva. LHC Experiments Committee. *ATLAS : technical proposal for a general-purpose pp experiment at the Large Hadron Collider at CERN*, note = CERN-LHCC-94-43. Tech. rep. ATLAS Collaboration, 1994.
- [14] CERN. Geneva. LHC Experiments Committee. *CMS : letter of intent by the CMS Collaboration for a general purpose detector at LHC*, note = CERN-LHCC-92-003. Tech. rep. CMS Collaboration, 1992.
- [15] CERN. Geneva. LHC Experiments Committee. *LHCb : letter of intent*. Tech. rep. CERN-LHCC-95-5. LHCb Collaboration, 1995.
- [16] L. Evans and P. Bryant. “LHC Machine”. In: *JINST* 3 (2008). S08001.
- [17] CMS Collaboration ATLAS Collaboration. “Combined Measurement of the Higgs Boson Mass in pp Collisions at $\sqrt{s} = 7$ and 8 TeV with the ATLAS and CMS Experiments”. In: *Physical Review Letters* 114 (2015). 191803.
- [18] LHCb Collaboration. “Observation of $J/\psi p$ Resonances Consistent with Pentaquark States in $\Lambda_b^0 \rightarrow J/\psi K^- p$ Decays”. In: *Physical Review Letters* 115 (2015). 072001.

- 2695 [19] LHCb Collaboration. “Observation of $J/\psi\phi$ Structures Consistent with Exotic States from
2696 Amplitude Analysis of $B^+ \rightarrow J/\psi\phi K^+$ Decays”. In: *Physical Review Letters* 118 (2017).
2697 022003.
- 2698 [20] CERN. Geneva. *High-Luminosity Large Hadron Collider (HL-LHC) Technical Design Re-*
2699 *port V. 0.1*. Tech. rep. CERN-2017-007-M. 2017.
- 2700 [21] CERN. Geneva. LHC Experiments Committee. *The CMS muon project : Technical Design*
2701 *Report*. Tech. rep. CERN-LHCC-97-032. CMS Collaboration, 1997.
- 2702 [22] CERN. Geneva. LHC Experiments Committee. *Technical Proposal for the Phase-II Upgrade*
2703 *of the CMS Detector*. Tech. rep. CERN-LHCC-2015-010. CMS Collaboration, 2015.
- 2704 [23] CERN. Geneva. LHC Experiments Committee. *CMS, the Compact Muon Solenoid : technical*
2705 *proposal*. Tech. rep. CERN-LHCC-94-38. CMS Collaboration, 1994.
- 2706 [24] R. Santonico and R. Cardarelli. “Development of resistive plate counters”. In: *Nucl. Instr.*
2707 *Meth. Phys. Res.* 187 (1981), pp. 377–380.
- 2708 [25] Yu.N. Pestov and G.V. Fedotovich. *A picosecond time-of-flight spectrometer for the VEPP-2M*
2709 *based on local-discharge spark counter*. Tech. rep. SLAC-TRANS-0184. SLAC, 1978.
- 2710 [26] W.W. Ash, ed. *Spark Counter With A Localized Discharge*. Vol. SLAC-R-250. 1982, pp. 127–
2711 131.
- 2712 [27] I. Crotty et al. “The non-spark mode and high rate operation of resistive parallel plate cham-
2713 bers”. In: *NIMA* 337 (1993), pp. 370–381.
- 2714 [28] I. Crotty et al. “Further studies of avalanche mode operation of resistive parallel plate cham-
2715 bers”. In: *NIMA* 346 (1994), pp. 107–113.
- 2716 [29] R. Cardarelli et al. “Avalanche and streamer mode operation of resistive plate chambers”. In:
2717 *NIMA* 382 (1996), pp. 470–474.
- 2718 [30] E. Cerron Zeballos et al. “A new type of resistive plate chamber: The multigap RPC”. In:
2719 *NIMA* 374 (1996), pp. 132–135.
- 2720 [31] M.C.S. Williams. “The development of the multigap resistive plate chamber”. In: *Nucl. Phys.*
2721 *B* 61 (1998), pp. 250–257.
- 2722 [32] H. Czyrkowski et al. “New developments on resistive plate chambers for high rate operation”.
2723 In: *NIMA* 419 (1998), pp. 490–496.
- 2724 [33] P. Camarri et al. “Streamer suppression with SF6 in RPCs operated in avalanche mode”. In:
2725 *NIMA* 414 (1998), pp. 317–324.
- 2726 [34] E. Cerron Zeballos et al. “Effect of adding SF6 to the gas mixture in a multigap resistive plate
2727 chamber”. In: *NIMA* 419 (1998), pp. 475–478.
- 2728 [35] CERN. Geneva. LHC Experiments Committee. *ATLAS muon spectrometer: Technical design*
2729 *report*. Tech. rep. CERN-LHCC-97-22. ATLAS Collaboration, 1997.
- 2730 [36] CERN. Geneva. LHC Experiments Committee. *ALICE Time-Of-Flight system (TOF) : Tech-*
2731 *nical Design Report*. Tech. rep. CERN-LHCC-2000-012. ALICE Collaboration, 2000.
- 2732 [37] The CALICE collaboration. “First results of the CALICE SDHCAL technological proto-
2733 type”. In: *JINST* 11 (2016).
- 2734 [38] PoS, ed. *Density Imaging of Volcanoes with Atmospheric Muons using GRPCs*. International
2735 Europhysics Conference on High Energy Physics - HEP 2011. 2011.
- 2736 [39] C. Lippmann. “Detector Physics of Resistive Plate Chambers”. PhD thesis. Johann Wolfgang
2737 Goethe-Universität, 2003.

BIBLIOGRAPHY

- 2738 [40] M. Abbrescia et al. “Properties of C₂H₂F₄-based gas mixture for avalanche mode operation
2739 of resistive plate chambers”. In: *NIMA* 398 (1997), pp. 173–179.
- 2740 [41] G.Battistoni et al. “Sensitivity of streamer mode to single ionization electrons”. In: *NIMA*
2741 235 (1985), pp. 91–97.
- 2742 [42] W. Riegler. “Induced signals in resistive plate chambers”. In: *NIMA* 491 (2002), pp. 258–271.
- 2743 [43] E. Cerron Zeballos et al. “A comparison of the wide gap and narrow gap resistive plate
2744 chamber”. In: *NIMA* 373 (1996), pp. 35–42.
- 2745 [44] M. Abbrescia et al. “Cosmic ray tests of double-gap resistive plate chambers for the CMS
2746 experiment”. In: *NIMA* 550 (2005), pp. 116–126.
- 2747 [45] ALICE Collaboration. “A study of the multigap RPC at the gamma irradiation facility at
2748 CERN”. In: *NIMA* 490 (2002), pp. 58–70.
- 2749 [46] B. Bonner et al. “A multigap resistive plate chamber prototype for time-of-flight for the STAR
2750 experiment at RHIC”. In: *NIMA* 478 (2002), pp. 176–179.
- 2751 [47] S. Yang et al. “Test of high time resolution MRPC with different readout modes for the
2752 BESIII upgrade”. In: *NIMA* 763 (2014), pp. 190–196.
- 2753 [48] A. Akindinov et al. “RPC with low-resistive phosphate glass electrodes as a candidate for
2754 the CBM TOF”. In: *NIMA* 572 (2007), pp. 676–681.
- 2755 [49] JINST, ed. *Development of the MRPC for the TOF system of the MultiPurpose Detector.*
2756 RPC2016: XII Workshop on Resistive Plate Chambers and Related Detectors. 2016.
- 2757 [50] M.C.S. Williams. “Particle identification using time of flight”. In: *Journal of Physics G* 39
2758 (2012).
- 2759 [51] A. Alici et al. “Aging and rate effects of the Multigap RPC studied at the Gamma Irradiation
2760 Facility at CERN”. In: *NIMA* 579 (2007), pp. 979–988.
- 2761 [52] M. Abbrescia et al. “The simulation of resistive plate chambers in avalanche mode: charge
2762 spectra and efficiency”. In: *NIMA* 431 (1999), pp. 413–427.
- 2763 [53] M. Abbrescia et al. “Study of long-term performance of CMS RPC under irradiation at the
2764 CERN GIF”. In: *NIMA* 533 (2004), pp. 102–106.
- 2765 [54] H.C. Kim et al. “Quantitative aging study with intense irradiation tests for the CMS forward
2766 RPCs”. In: *NIMA* 602 (2009), pp. 771–774.
- 2767 [55] S. Agosteo et al. “A facility for the test of large-area muon chambers at high rates”. In: *NIMA*
2768 452 (2000), pp. 94–104.
- 2769 [56] PoS, ed. *CERN GIF ++ : A new irradiation facility to test large-area particle detectors for*
2770 *the high-luminosity LHC program*. Vol. TIPP2014. 2014, pp. 102–109.
- 2771 [57] A. Fagot. *GIF++ DAQ v4.0*. 2017. URL: https://github.com/afagot/GIF_DAQ.
- 2772 [58] CAEN. *Mod. V1190-VX1190 A/B, 128/64 Ch Multihit TDC*. 14th ed. 2016.
- 2773 [59] CAEN. *Mod. V1718 VME USB Bridge*. 9th ed. 2009.
- 2774 [60] W-Ie-Ne-R. *VME 6021-23 VXI*. 5th ed. 2016.
- 2775 [61] Wikipedia. *INI file*. 2017. URL: https://en.wikipedia.org/wiki/INI_file.
- 2776 [62] S. Carrillo A. Fagot. *GIF++ Offline Analysis v6*. 2017. URL: https://github.com/afagot/GIF_OfflineAnalysis.